NASA TECHNICAL NOTE

NASA TN D-5514

c. 1

NASA TN D-5514

WIND-TUNNEL INVESTIGATION OF THE AERODYNAMIC PRESSURES ON THE APOLLO COMMAND MODULE CONFIGURATION

by William C. Moseley, Jr., and B. J. Wells

Manned Spacecraft Center
Houston, Texas

NATIONAL AERONAUTICS AND SPACE ADMINISTRATION • WASHINGTON, D. C. • OCTOBER 1969

1. REPORT NO. NASA TN D-5514	2. GOVERNMENT ACCESSION NO.	3. RECIPIENT'S
4. TITLE AND SUBTITLE WIND-TUNNEL INVESTIGATION OF THE AERODYNAMIC PRESSURES ON THE APOLLO COMMAND MODULE CONFIGURATION		5. REPORT DATE October 1969
		6. PERFORMING ORGANIZATION CODE
7. AUTHOR(S) William C. Moseley, Jr., MSC, and B. J. Wells, ITT, Federal Electric Corp.		8. PERFORMING ORGANIZATION REPORT NO. S-219
9. PERFORMING ORGANIZATION NAME AND ADDRESS Manned Spacecraft Center Houston, Texas 77058		10. WORK UNIT NO. 914-50-10-03-72
		11. CONTRACT OR GRANT NO.
12. SPONSORING AGENCY NAME AND ADDRESS National Aeronautics and Space Administration Washington, D.C. 20546		13. REPORT TYPE AND PERIOD COVERED Technical Memorandum
		14. SPONSORING AGENCY CODE
15. SUPPLEMENTARY NOTES		

16. ABSTRACT

A program of wind-tunnel tests was conducted at Mach numbers from 0.4 to 19.0 to determine the pressure distribution of the Apollo command module. Data are presented for the angle-of-attack range from 0° to 180°. Results of these tests are presented as pressure coefficients plotted against the physical positions of the orifices.

17. KEY WORDS (SUPPLIED BY AUTHOR) · Aerodynamic Characteristics · Apollo · Wind Tunnel · Scale Model · Command Module · Pressure Coefficient · Manned Spacecraft	18. DISTRIBUTION STATEMENT

19. SECURITY CLASSIFICATION (THIS REPORT)	20. SECURITY CLASSIFICATION (THIS PAGE)	21. NO. OF PAGES	22. PRICE *
Unclassified	Unclassified	77	$3.00

*For sale by the Clearinghouse for Federal Scientific and Technical Information
Springfield, Virginia 22151

CONTENTS

TABLES

FIGURES

Figure		Page

Figure		Page

WIND-TUNNEL INVESTIGATION OF THE AERODYNAMIC PRESSURES ON THE APOLLO COMMAND MODULE CONFIGURATION

By William C. Moseley, Jr., and B. J. Wells*
Manned Spacecraft Center

SUMMARY

Wind-tunnel tests were conducted at several facilities to determine the pressure distribution over the Apollo command module at Mach numbers from low subsonic speed to hypersonic speed. The Mach-number range is 0.4 to 19.0, and the angle of attack varies from 0° to 180°.

The data obtained from these tests are presented in this paper as pressure coefficients plotted against the physical positions of the orifices. Only limited data are presented in the angle-of-attack range from 0° to 140°; the area of concentration is the angle-of-attack range from 150° to 180° because this is the trim-angle-of-attack range for atmospheric entry.

INTRODUCTION

In late 1959, personnel from several NASA Centers recommended a circumlunar flight and an earth-orbiting laboratory program to be called the Apollo Program. This program was initiated and was assigned to the NASA space task group. On May 25, 1961, the Apollo Program was reoriented toward achieving a manned lunar landing as part of the continuing program of space exploration following Project Mercury and the Gemini Program.

To satisfy the design criteria and guidelines for an Apollo spacecraft, many possible configurations were considered. The basic configuration chosen for development was the one determined to be most practical with respect to the current development of the state of the art.

Once the configuration was determined, it was necessary to evaluate the basic design of the Apollo spacecraft thoroughly. One means of evaluating the basic design was the Apollo wind-tunnel testing program (AWTTP). This program is discussed in detail in reference 1. Early wind-tunnel studies that were used to support and verify the basic design as the most practical are discussed in references 2 to 5.

*ITT/Federal Electric Corporation.

Investigations were made as a part of the AWTTP to determine the aerodynamic loads on the Apollo command-module (CM) configuration. Pressure distributions were determined at Mach numbers from 0.4 to 19.0 over an angle-of-attack range of 0° to 180°. Data are presented in this paper as pressure coefficients plotted against the physical positions of the orifices.

SYMBOLS

The positive directions of the body-axis system, as referred to in the following list, are shown in figure 1.

C_p	pressure coefficient, $(P_X - P_\infty)/q_\infty$
D	maximum diameter of CM (154 inches full scale)
M	Mach number
P_X	orifice pressure
P_∞	free-stream static pressure
q_∞	free-stream dynamic pressure, $1/2\rho V^2$
R	radius
R_e	Reynolds number (based on maximum model diameter)
r	radius of CM at maximum diameter
s	distance to orifice from the center of the apex or of the heat shield of the model, measured along the surface, positive in the positive Z-direction for apex-forward mounting and positive in the negative Z-direction for heat-shield-forward mounting
V	velocity
X, Y, Z	body reference axes
α	angle of attack in the XZ-plane
λ	angle of instrumentation plane relative to pitch plane
ρ	air density

MODELS AND TEST TECHNIQUES

The CM body-axis system is shown in figure 1, and sketches of test models with controlling dimensions are shown in figure 2. Typical photographs of test models mounted in test facilities are shown in figure 3.

The models tested vary in scale from 0.02 to 0.05; the configurations are shown in figure 2.

Data were determined for attitudes with both apex (small end) and heat shield (blunt face) forward. The apex-forward attitude was designated as $\alpha = 0°$; and, through the use of a series of modules, data were determined at designated angles of attack from 0° to 180°. All the modules were sting-supported, and the sting attachment was usually in the wake of the model. The ratio of sting diameter to model diameter varied from facility to facility, and no attempt has been made to correct the data for sting-interference effects.

Static pressure orifices are located on the surface of the Apollo CM. The physical position of an individual orifice is indicated by the ratio of s/r, as presented in figure 4, for the models tested.

Each orifice was connected to a calibrated pressure transducer, and the resulting pressure readings were reduced to the standard pressure-coefficient form by using the following equation:

$$C_p = \frac{P_X - P_\infty}{q_\infty}$$

FACILITIES

The broad range of expected flight conditions (M, R_e, and α) and the limitations of a wind tunnel to simulate all these conditions dictated the use of certain test facilities. The facilities used to acquire pressure distribution on the CM configuration are listed in table I, along with wind-tunnel sizes and capabilities. These facilities included the Arnold Engineering Development Center Tunnel C (AEDC-C), the Ames 2- by 2-foot transonic wind tunnel (Ames 2×2 TWT), the Jet Propulsion Laboratory 20-inch supersonic wind tunnel (JPL-20SWT) and 21-inch hypersonic wind tunnel (JPL-21HWT), the Arnold Engineering Development Center Hot-Shot II impulse tunnel (AEDC-HS II), and the Cornell Aeronautical Laboratory 48-inch hypersonic shock tunnel (CAL-48HST).

TEST CONDITIONS AND ACCURACY

Test Conditions

Test conditions are listed in table II according to the facility used.

Accuracy

Table III is a list of estimated errors encountered in the test facilities utilized in this study.

SUMMARY OF RESULTS

Static and dynamic characteristics of the Apollo CM (with and without surface protuberances) were investigated and are presented in reference 6; the effects of varying certain geometric dimensions of the basic CM configuration are presented in reference 7. The pressure-coefficient data for these configurations are presented herein with a minimum of analysis.

The data presented in figures 5 to 39 are plotted as pressure coefficient versus physical position of the orifices, with the pressure coefficient having three data planes: $\lambda = 0°$, $\lambda = 45°$, and $\lambda = 90°$. (Values of λ and s/r for various model orifice numbers are presented in figure 4.) The results of this report are summarized in the following figures.

1. Figures 5 to 18 present the variation of the pressure coefficient with increasing angle of attack from 0° to 140° at Mach numbers from 0.4 to 10.1 in the apex-forward attitude.

2. Figures 19 to 39 present the variation of the pressure coefficient with increasing angle of attack from 140° to 180° at Mach numbers from 0.4 to 19.0 in the heat-shield-forward attitude.

Additional information and data are available in references 8 and 9.

Manned Spacecraft Center
National Aeronautics and Space Administration
Houston, Texas, August 4, 1969
914-50-10-03-72

REFERENCES

1. Moseley, William C., Jr.; and Martino, Joseph C.: Apollo Wind Tunnel Testing Program — Historical Development of General Configurations. NASA TN D-3748, 1966.

2. Morgan, James R.; and Fournier, Roger H.: Static Longitudinal Characteristics of a 0.07-Scale Model of a Proposed Apollo Spacecraft at Mach Numbers of 1.57 to 4.65 (C). NASA TM X-603, 1961.

3. Pearson, Albin O.: Wind-Tunnel Investigation of the Static Longitudinal Aerodynamic Characteristics of Models of Reentry and Atmospheric-Abort Configurations of a Proposed Apollo Spacecraft at Mach Numbers from 0.30 to 1.20 (C). NASA TM X-604, 1961.

4. Pearson, Albin O.: Wind-Tunnel Investigation of the Static Longitudinal Aerodynamic Characteristics of a Modified Model of a Proposed Apollo Atmospheric-Abort Configuration at Mach Numbers from 0.30 to 1.20. NASA TM X-686, 1962.

5. Fournier, Roger H.; and Corlett, William A.: Aerodynamic Characteristics in Pitch of Several Models of the Apollo Abort System from Mach 1.57 to 2.16. NASA TM X-910, 1964.

6. Mosely, William C., Jr.; Moore, Robert H., Jr.; and Hughes, Jack E.: Stability Characteristics of the Apollo Command Module. NASA TN D-3890, 1967.

7. Moseley, William C., Jr.; Graham, Ralph E.; and Hughes, Jack E.: Aerodynamic Stability Characteristics of the Apollo Command Module. NASA TN D-4688, 1968.

8. Deitering, J. S.; and Brillhart, R. E., Jr.: Pressure Tests on Apollo Configurations at Mach Numbers 1.5, 2, 3, and 10 (C). AEDC-TDR-63-164, 1963.

9. Knox, E. C.: Pressure Distributions and Force Coefficients Measured on the Apollo Command Module Reentry Configuration at Mach 19 (C). AEDC-TDR-62-193, 1962.

TABLE I. - TEST FACILITIES

Facility	Size of test section	Mach-number range	Reynolds-number range $\times 10^{-6}$/ft
Continuous tunnels			
AEDC-C	50 in. diameter	10	0.29 to 2.5
Ames 2×2 TWT	2 by 2 ft	0 to 1.4	2 to 8.4
JPL-20SWT	18 by 20 in.	1.3 to 5	.4 to 6
JPL-21HWT	21 by 15 to 28 in.	5 to 9.5	.25 to 3.6
Impulse tunnels			
AEDC-HS II	50 in. diameter	16 to 21	0.062 to 0.3
CAL-48HST	48 in. diameter	5 to 18	.03 to 10

TABLE II. - TEST CONDITIONS

Facility	Mach number	Angle-of-attack range, deg	Reynolds number × 10^{-6}
AEDC-C	10.1	0 to 180	1.1
AEDC-HS II	19.0	140 to 180	.085
Ames 2×2 TWT	.4	0 to 180	.077
	.7	0 to 180	.077
	.9	0 to 180	.080
	1.1	0 to 180	.077
	1.2	0 to 180	.077
	1.34	0 to 180	.074
JPL-20SWT	1.48	0 to 180	1.68
	2.01	0 to 180	1.71
	3.01	0 to 180	.98
	3.99	0 to 180	.75
	5.01	0 to 180	.76
JPL-21HWT	6.07	140 to 180	.807
	7.35	0 to 180	.75
	9.08	0 to 180	.46
CAL-48HST	12.0	150 to 180	.061
	12.7	150 to 180	.298
	13.1	150 to 180	1.052
	16.2	150 to 180	.048
	17.3	150 to 180	.196

TABLE III. - ESTIMATED ERRORS

Item	Facility					
	AEDC-C	AEDC-HS II	Ames 2×2 TWT	JPL-20SWT	JPL-21HWT	CAL-48HST
Transducer, psi	0.002	--	0.02	0.0025	0.0025	0.01
C_p	0.001	0.05	0.1	--	--	0.07
α, deg . . .	0.1	--	0.003	--	--	0.1
M	--	--	--	--	--	0.083

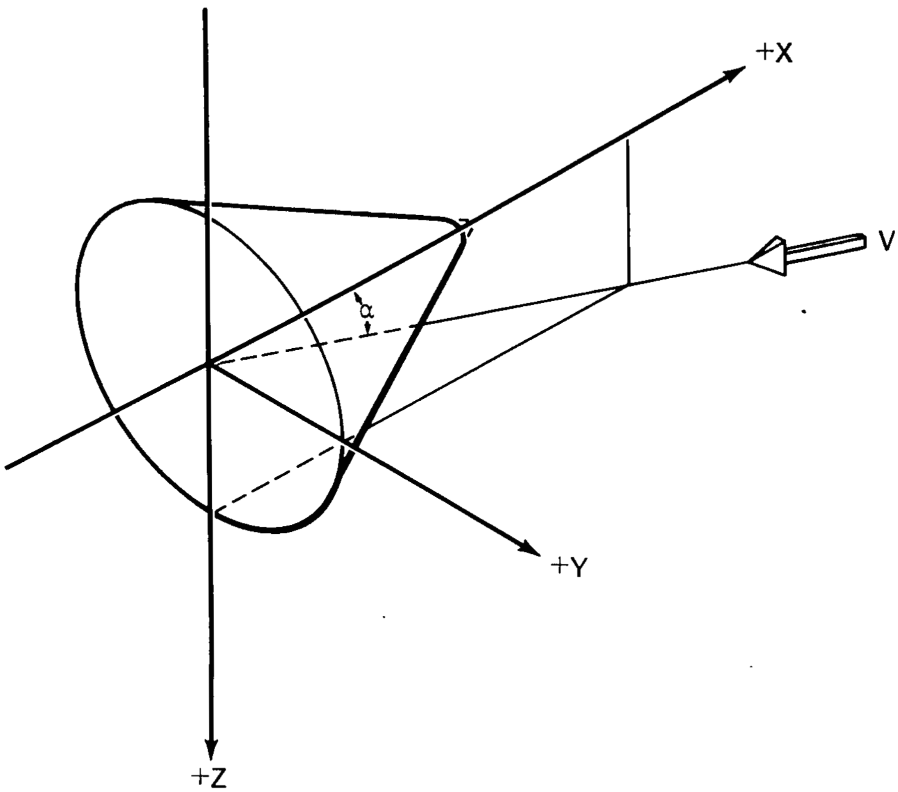

Figure 1. - Body-axis system.

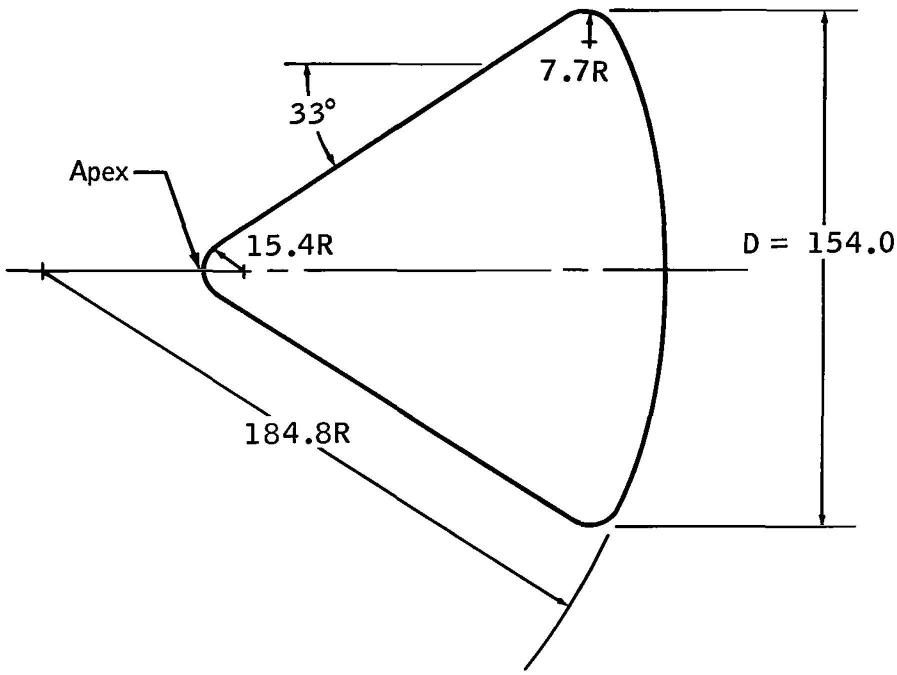

(a) Command module configuration C_1.

Figure 2. - Sketch of Apollo command module. Dimensions are given in full-scale inches; however, drawings are not to scale.

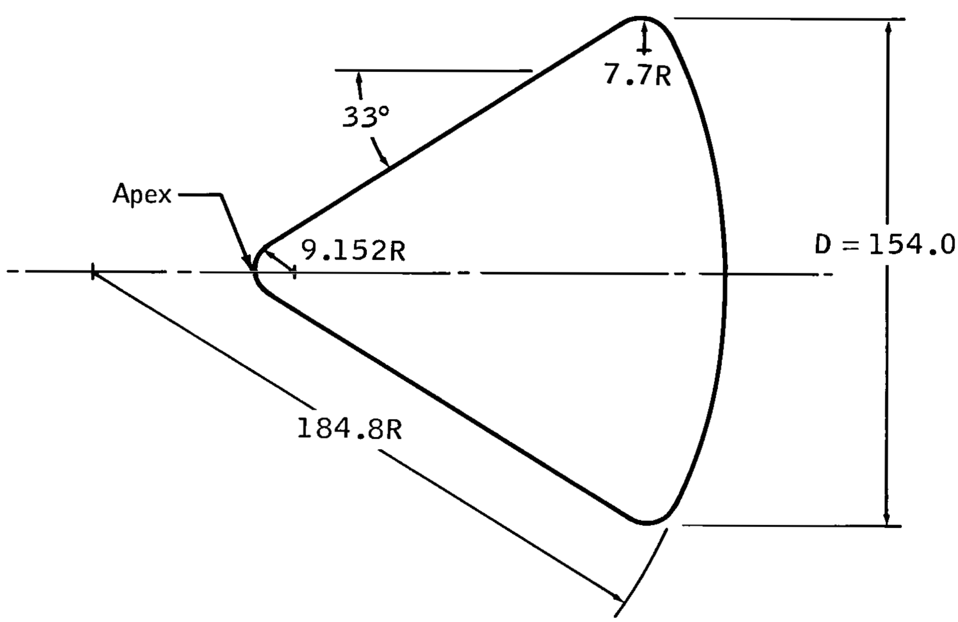

(b) Command module configuration C_2.

Figure 2. - Continued.

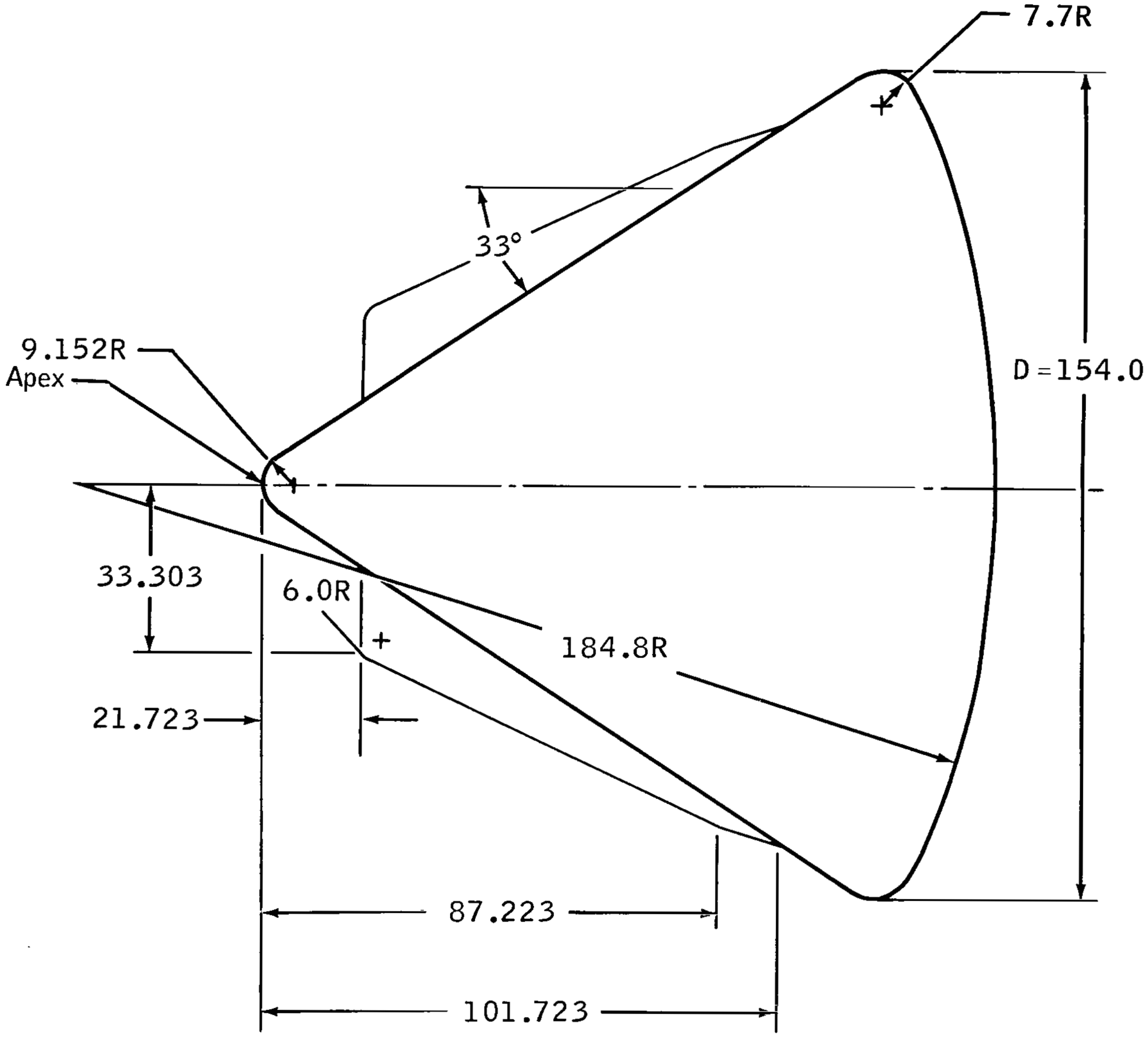

(c) Command module configuration with strakes (configuration $C_{38}L_{28}$).

Figure 2. - Concluded.

(a) AEDC-C, heat shield forward, configuration C_2.

Figure 3. - Photographs of test models.

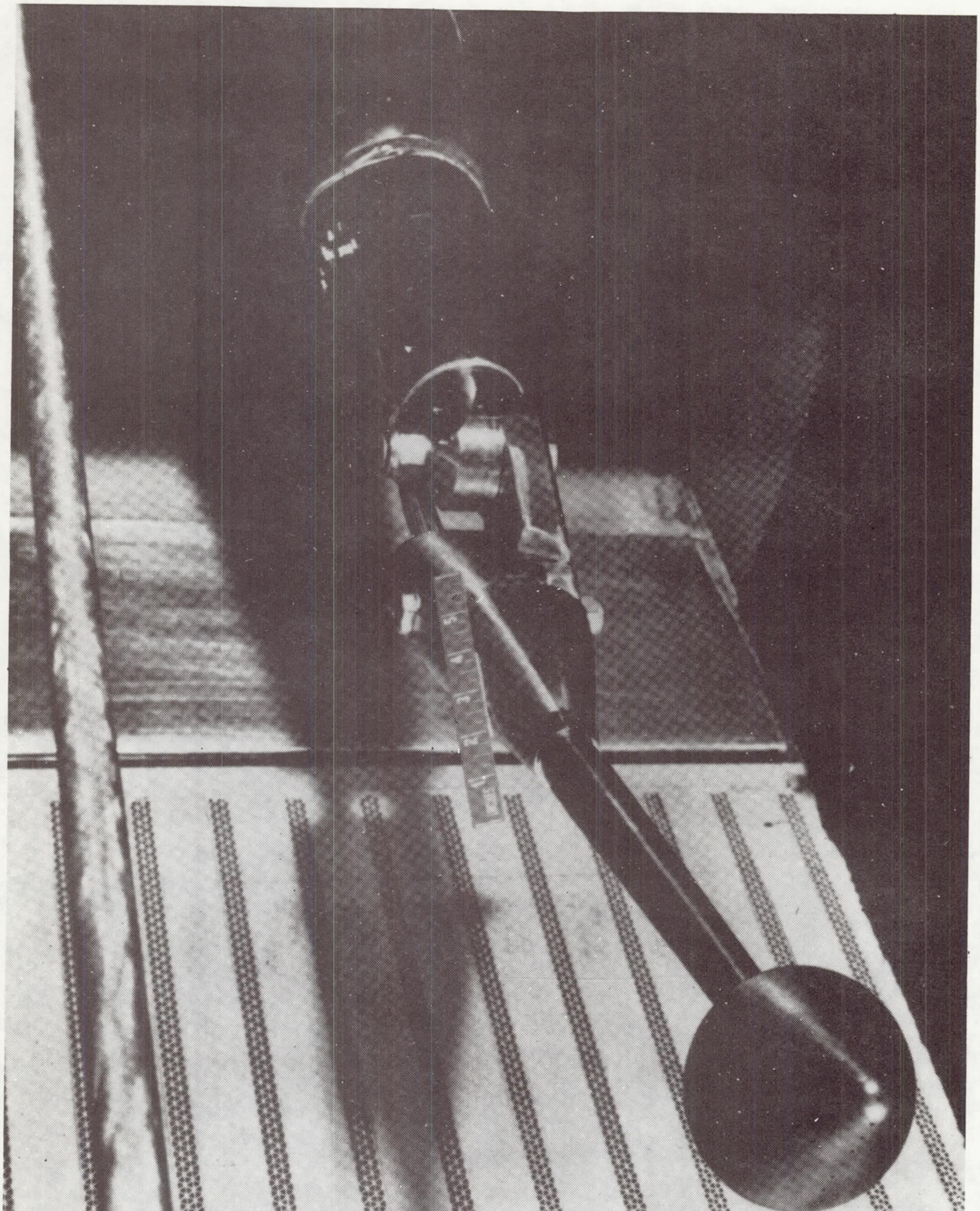

(b) Ames 2×2 TWT, configuration C_1.

Figure 3. - Concluded.

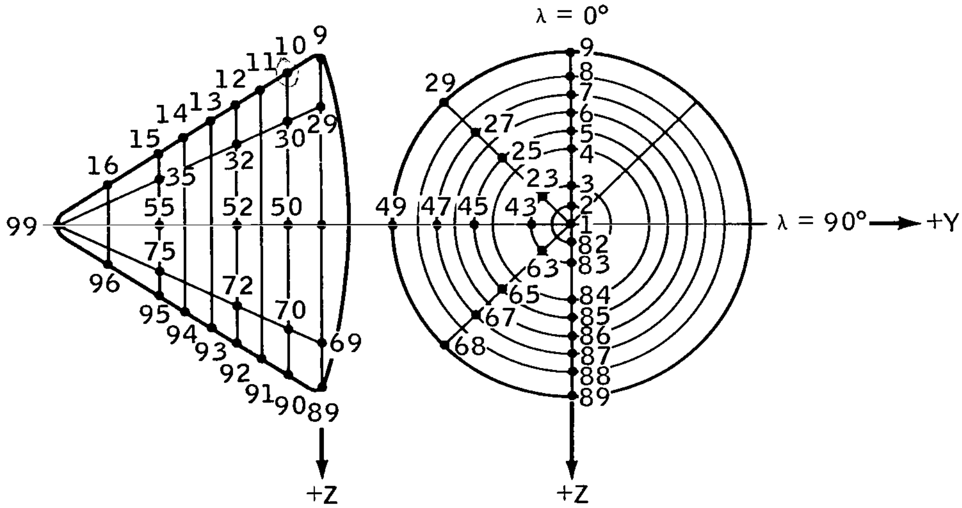

Model orifice no.		s/r Apex forward	s/r Heat shield forward	Model orifice no.		s/r Apex forward	s/r Heat shield forward
99	λ = 0°	0.000	2.846	94	λ = 0°	.686	-2.160
16	λ = 0°	-.253	2.593	95	λ = 0°	.470	-2.376
15	λ = 0°	-.470	2.376	96	λ = 0°	.253	-2.593
14	λ = 0°	-.686	2.160	99	λ = 45°	.000	2.846
13	λ = 0°	-.902	1.944	35	λ = 45°	-.470	2.376
12	λ = 0°	-1.118	1.728	32	λ = 45°	-1.118	1.728
11	λ = 0°	-1.334	1.512	30	λ = 45°	-1.550	1.296
10	λ = 0°	-1.550	1.296	29	λ = 45°	-1.765	1.081
9	λ = 0°	-1.765	1.081	27	λ = 45°	-2.052	.794
8	λ = 0°	-1.914	.932	25	λ = 45°	-2.322	.524
7	λ = 0°	-2.052	.794	23	λ = 45°	-2.586	.260
6	λ = 0°	-2.118	.658	1	λ = 45°	2.846	.000
5	λ = 0°	-2.322	.524	63	λ = 45°	2.586	-.260
4	λ = 0°	-2.455	.391	65	λ = 45°	2.322	-.524
3	λ = 0°	-2.586	.260	67	λ = 45°	2.052	-.794
2	λ = 0°	-2.716	.130	69	λ = 45°	1.765	-1.081
1	λ = 0°	2.846	.000	70	λ = 45°	1.550	-1.296
82	λ = 0°	2.716	-.130	72	λ = 45°	1.118	-1.728
83	λ = 0°	2.586	-.260	75	λ = 45°	.470	-2.376
84	λ = 0°	2.455	-.391	99	λ = 90°	.000	2.846
85	λ = 0°	2.322	-.524	55	λ = 90°	.470	2.376
86	λ = 0°	2.188	-.658	52	λ = 90°	1.118	1.728
87	λ = 0°	2.052	-.794	50	λ = 90°	1.550	1.296
88	λ = 0°	1.914	-.932	49	λ = 90°	1.765	1.081
89	λ = 0°	1.765	-1.081	47	λ = 90°	2.052	.794
90	λ = 0°	1.550	-1.296	45	λ = 90°	2.322	.524
91	λ = 0°	1.334	-1.512	43	λ = 90°	2.586	.260
92	λ = 0°	1.118	-1.728	1	λ = 90°	2.846	.000
93	λ = 0°	.902	-1.944				

(a) 0.02-scale pressure model, configuration C_1. Apex forward: positive s in positive Z-direction. Heat shield forward: positive s in negative Z-direction.

Figure 4. - Pressure-orifice locations.

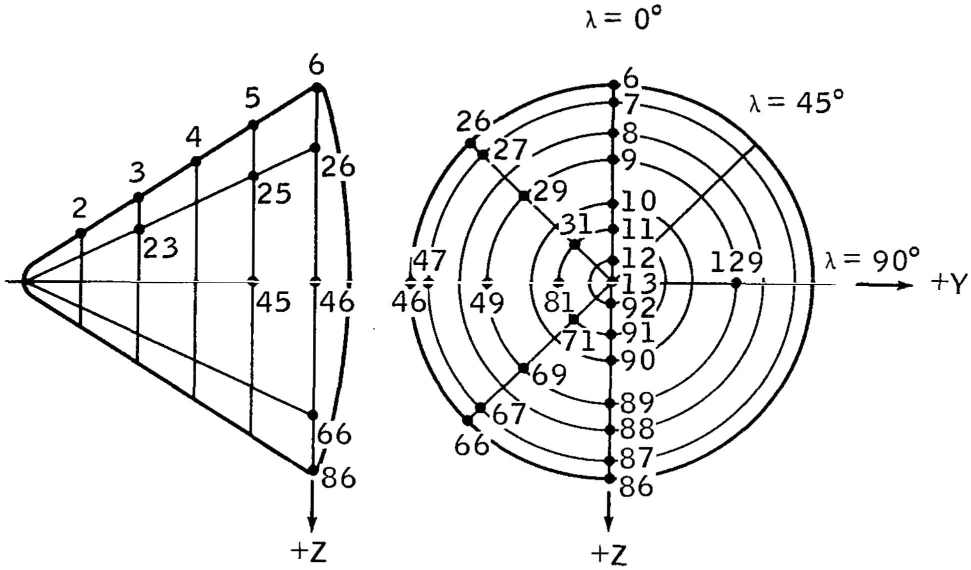

Model orifice no.		s/r Heat shield forward	Model orifice no.		s/r Heat shield forward
2	λ = 0°	2.566	23	λ = 45°	2.175
3	λ = 0°	2.179	25	λ = 45°	1.404
4	λ = 0°	1.791	26	λ = 45°	1.084
5	λ = 0°	1.404	27	λ = 45°	.984
6	λ = 0°	1.084	29	λ = 45°	.712
7	λ = 0°	.984	31	λ = 45°	.352
8	λ = 0°	.897	13	λ = 45°	.000
9	λ = 0°	.712	71	λ = 45°	-.352
10	λ = 0°	.530	69	λ = 45°	-.712
11	λ = 0°	.352	7	λ = 45°	-.984
12	λ = 0°	.175	66	λ = 45°	-1.084
13	λ = 0°	.000	45	λ = 90°	1.404
92	λ = 0°	-.175	46	λ = 90°	1.084
91	λ = 0°	-.352	47	λ = 90°	.984
90	λ = 0°	-.530	49	λ = 90°	.712
80	λ = 0°	-.712	51	λ = 90°	.352
88	λ = 0°	-.897	13	λ = 90°	.000
87	λ = 0°	-.984	129	λ = 90°	-.712
86	λ = 0°	-1.084			

(b) 0.04-scale pressure model, configuration C_2. Positive s in negative Z-direction.

Figure 4. - Continued.

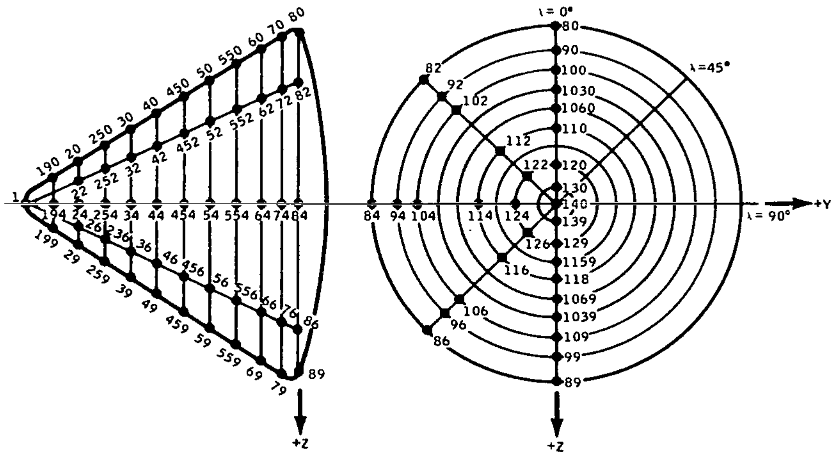

Model orifice no.		s/r Apex forward	s/r Heat shield forward	Model orifice no.		s/r Apex forward	s/r Heat shield forward
1	λ = 0°	0.000	2.886	42	λ = 45°	-.497	2.389
190	λ = 0°	-.064	2.822	452	λ = 45°	-1.046	1.950
20	λ = 0°	-.118	2.768	52	λ = 45°	-1.155	1.731
250	λ = 0°	-.208	2.678	552	λ = 45°	-1.372	1.514
30	λ = 0°	-.289	2.597	62	λ = 45°	-1.589	1.297
40	λ = 0°	-.497	2.389	72	λ = 45°	-1.742	1.144
450	λ = 0°	-.936	1.950	82	λ = 45°	-1.797	1.089
50	λ = 0°	-1.155	1.731	92	λ = 45°	-1.854	1.032
550	λ = 0°	-1.372	1.514	102	λ = 45°	-1.918	.968
60	λ = 0°	-1.589	1.297	112	λ = 45°	-2.085	.801
70	λ = 0°	-1.742	1.144	122	λ = 45°	-2.354	.532
80	λ = 0°	-1.797	1.089	140	λ = 45°	2.886	.000
90	λ = 0°	-1.854	1.032	126	λ = 45°	2.354	-.532
100	λ = 0°	-1.918	.968	116	λ = 45°	2.085	-.801
1030	λ = 0°	-1.979	.907	106	λ = 45°	1.918	-.968
1060	λ = 0°	-2.034	.852	96	λ = 45°	1.854	-1.032
110	λ = 0°	-2.085	.801	86	λ = 45°	1.797	-1.089
120	λ = 0°	-2.354	.532	76	λ = 45°	1.742	-1.144
130	λ = 0°	-2.626	.260	66	λ = 45°	1.589	-1.297
140	λ = 0°	2.886	.000	556	λ = 45°	1.372	-1.514
139	λ = 0°	2.626	-.260	56	λ = 45°	1.155	-1.731
129	λ = 0°	2.354	-.532	456	λ = 45°	.936	-1.950
1159	λ = 0°	2.143	-.743	46	λ = 45°	.497	-2.389
119	λ = 0°	2.085	-.801	36	λ = 45°	.289	-2.597
1069	λ = 0°	2.034	-.852	256	λ = 45°	.208	-2.672
1039	λ = 0°	1.979	-.907	26	λ = 45°	.118	-2.762
109	λ = 0°	1.918	-.968	1	λ = 90°	.000	2.886
99	λ = 0°	1.854	-1.032	194	λ = 90°	.064	2.822
89	λ = 0°	1.797	-1.089	24	λ = 90°	.118	2.762
79	λ = 0°	1.742	-1.144	254	λ = 90°	.208	2.672
69	λ = 0°	1.589	-1.297	34	λ = 90°	.289	2.597
559	λ = 0°	1.372	-1.514	44	λ = 90°	.497	2.389
59	λ = 0°	1.155	-1.731	454	λ = 90°	.936	1.950
459	λ = 0°	.936	-1.950	54	λ = 90°	1.155	1.731
49	λ = 0°	.497	-2.389	554	λ = 90°	1.372	1.514
39	λ = 0°	.289	-2.597	64	λ = 90°	1.589	1.297
259	λ = 0°	.208	-2.678	74	λ = 90°	1.742	1.144
29	λ = 0°	.118	-2.768	84	λ = 90°	1.797	1.089
199	λ = 0°	.064	-2.822	94	λ = 90°	1.854	1.032
1	λ = 45°	-.000	2.886	104	λ = 90°	1.918	.968
22	λ = 45°	-.118	2.762	114	λ = 90°	2.085	.801
252	λ = 45°	-.208	2.672	124	λ = 90°	2.354	.532
32	λ = 45°	-.289	2.597	140	λ = 90°	2.886	.000

(c) 0.045-scale pressure model, configuration C_2. Apex forward: positive s in positive Z-direction. Heat shield forward: positive s in negative Z-direction.

Figure 4. - Continued.

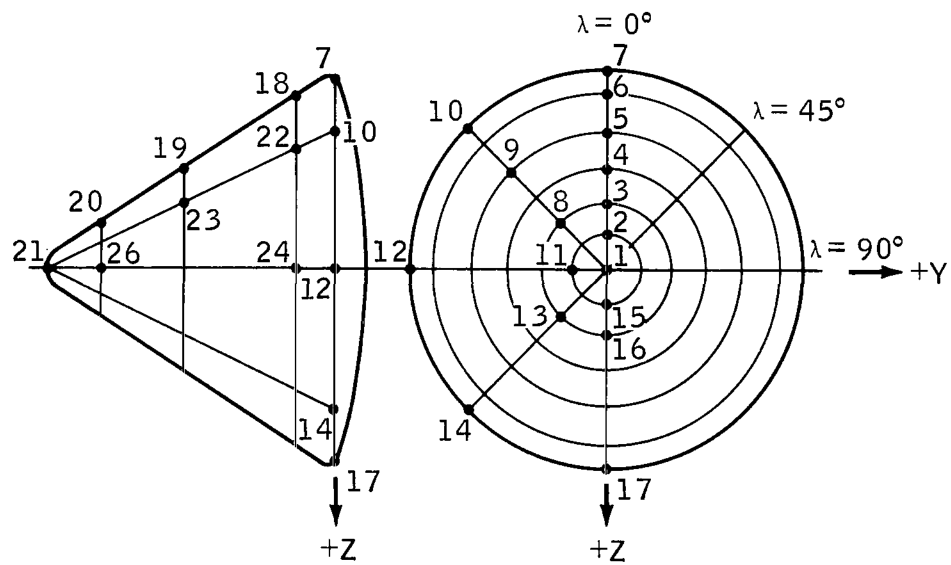

Model orifice no.		s/r Heat shield forward
21	λ = 0°	-2.885
20	λ = 0°	2.349
19	λ = 0°	1.757
18	λ = 0°	1.162
7	λ = 0°	1.086
6	λ = 0°	1.023
5	λ = 0°	.975
4	λ = 0°	.921
3	λ = 0°	.808
2	λ = 0°	.405
1	λ = 0°	.000
15	λ = 0°	-.401
16	λ = 0°	-.805
17	λ = 0°	-1.083
21	λ = 45°	2.885
23	λ = 45°	1.756
22	λ = 45°	1.163
10	λ = 45°	1.085
9	λ = 45°	.974
8	λ = 45°	.809
1	λ = 45°	.000
13	λ = 45°	-.802
14	λ = 45°	-1.088
21	λ = 90°	2.885
26	λ = 90°	2.347
24	λ = 90°	1.157
12	λ = 90°	1.087
11	λ = 90°	.404
1	λ = 90°	.000

(d) 0.05-scale pressure model, configuration C_2. Positive s in negative Z-direction.

Figure 4. - Concluded.

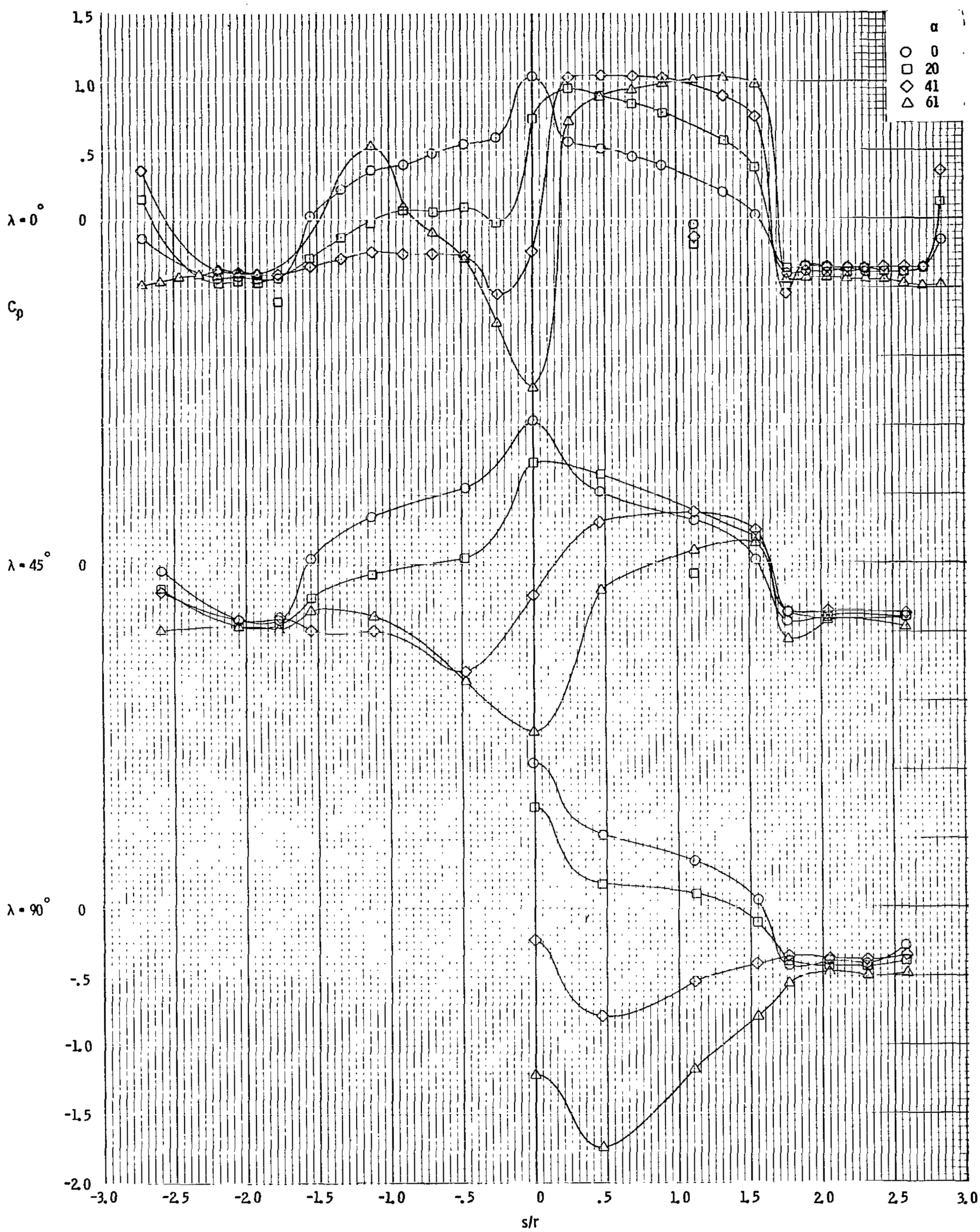

(a) $\alpha = 0°$ to $\alpha = 61°$.

Figure 5. - Variation of C_p with increasing α at $\lambda = 0°$, $\lambda = 45°$, and $\lambda = 90°$ at $M = 0.4$, 0.02-scale model, configuration C_1, apex forward, in the Ames 2×2 TWT test facility.

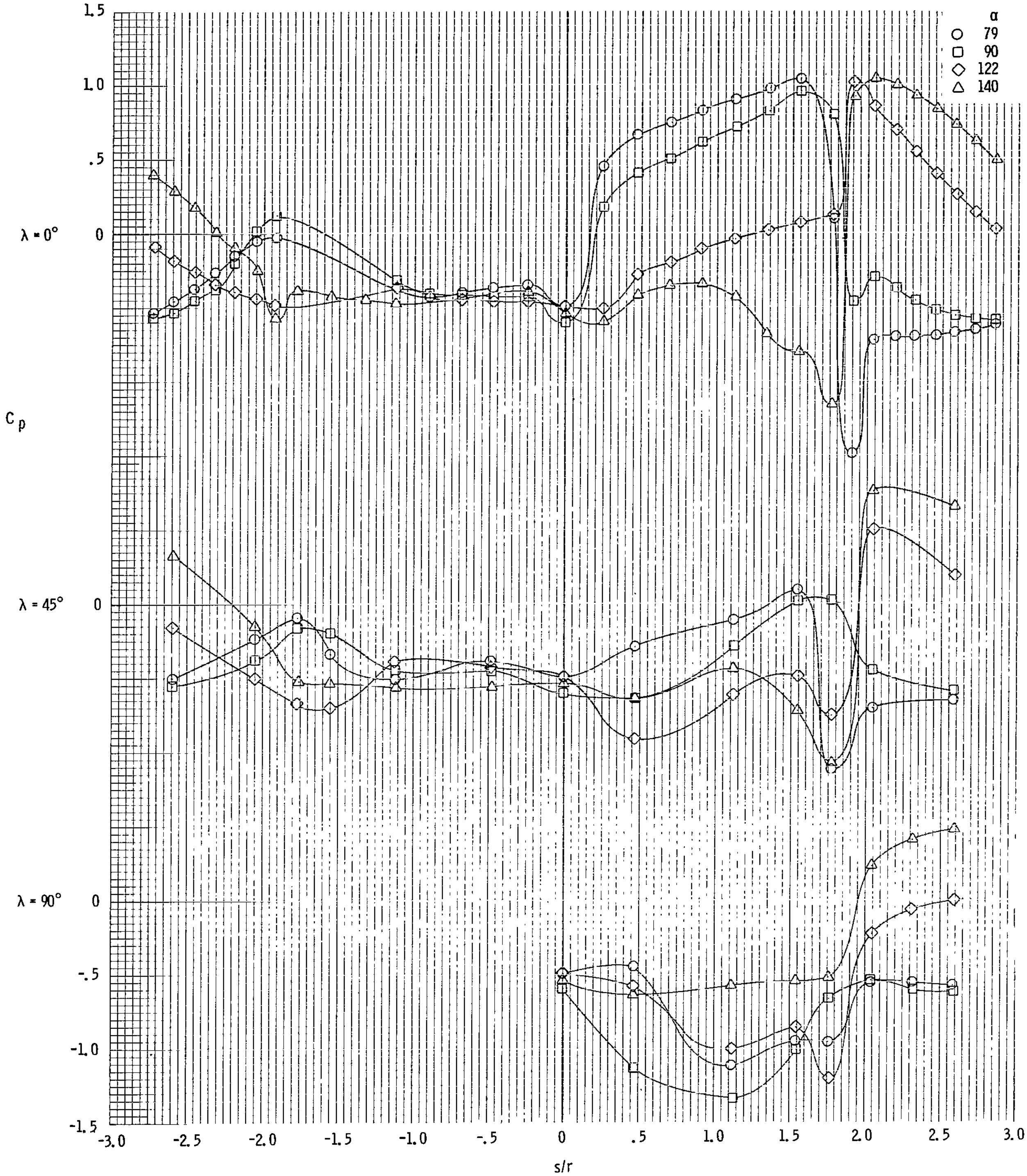

(b) α = 79° to α = 140°.

Figure 5. - Concluded.

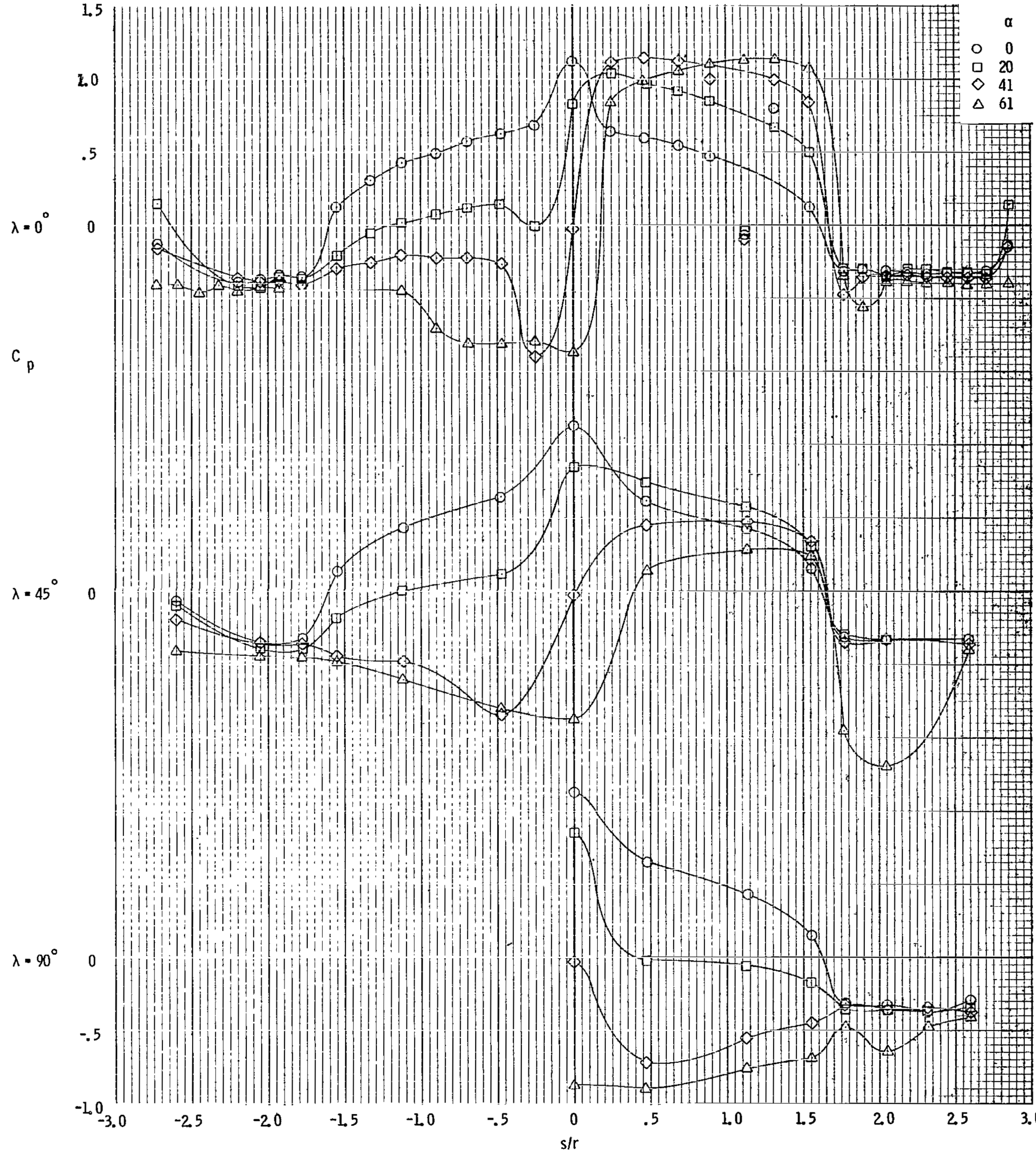

(a) $\alpha = 0°$ to $\alpha = 61°$.

Figure 6. - Variation of C_p with increasing α at $\lambda = 0°$, $\lambda = 45°$, and $\lambda = 90°$ at $M = 0.7$, 0.02-scale model, configuration C_1, apex forward, in the Ames 2×2 TWT test facility.

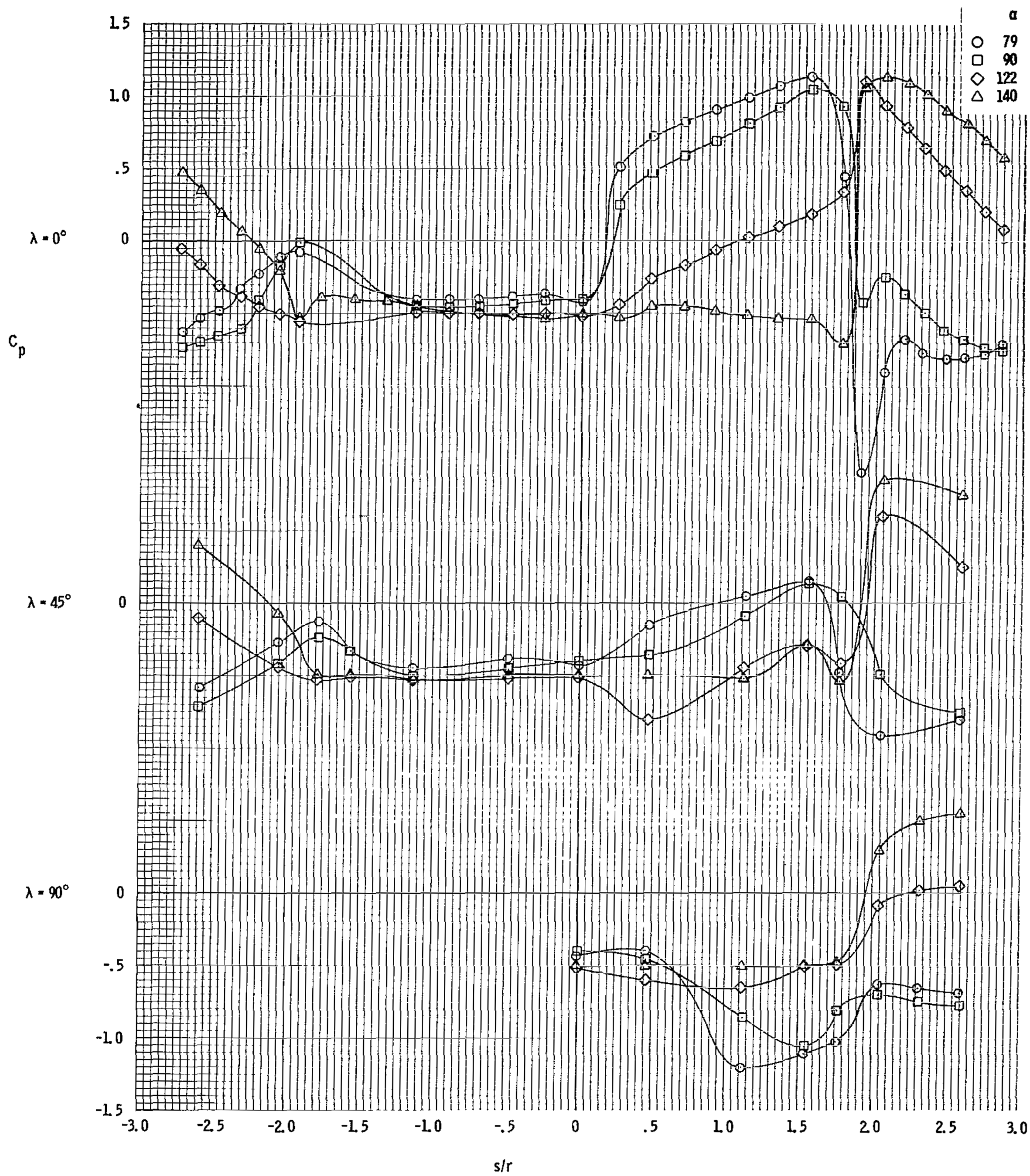

(b) $\alpha = 79°$ to $\alpha = 140°$.

Figure 6. - Concluded.

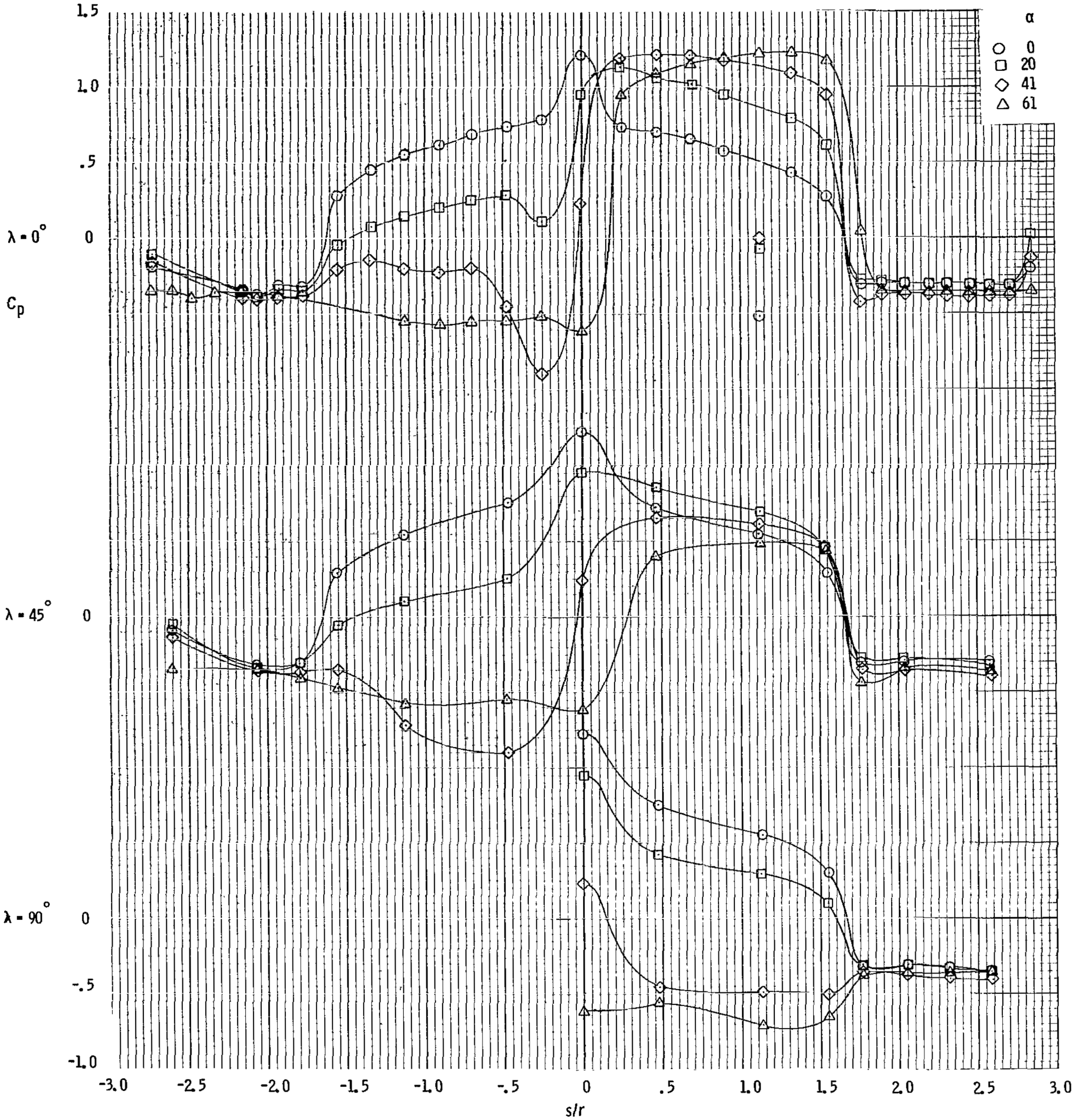

(a) $\alpha = 0°$ to $\alpha = 61°$.

Figure 7. - Variation of C_p with increasing α at $\lambda = 0°$, $\lambda = 45°$, and $\lambda = 90°$ at M = 0.9, 0.02-scale model, configuration C_1, apex forward, in the Ames 2×2 TWT test facility.

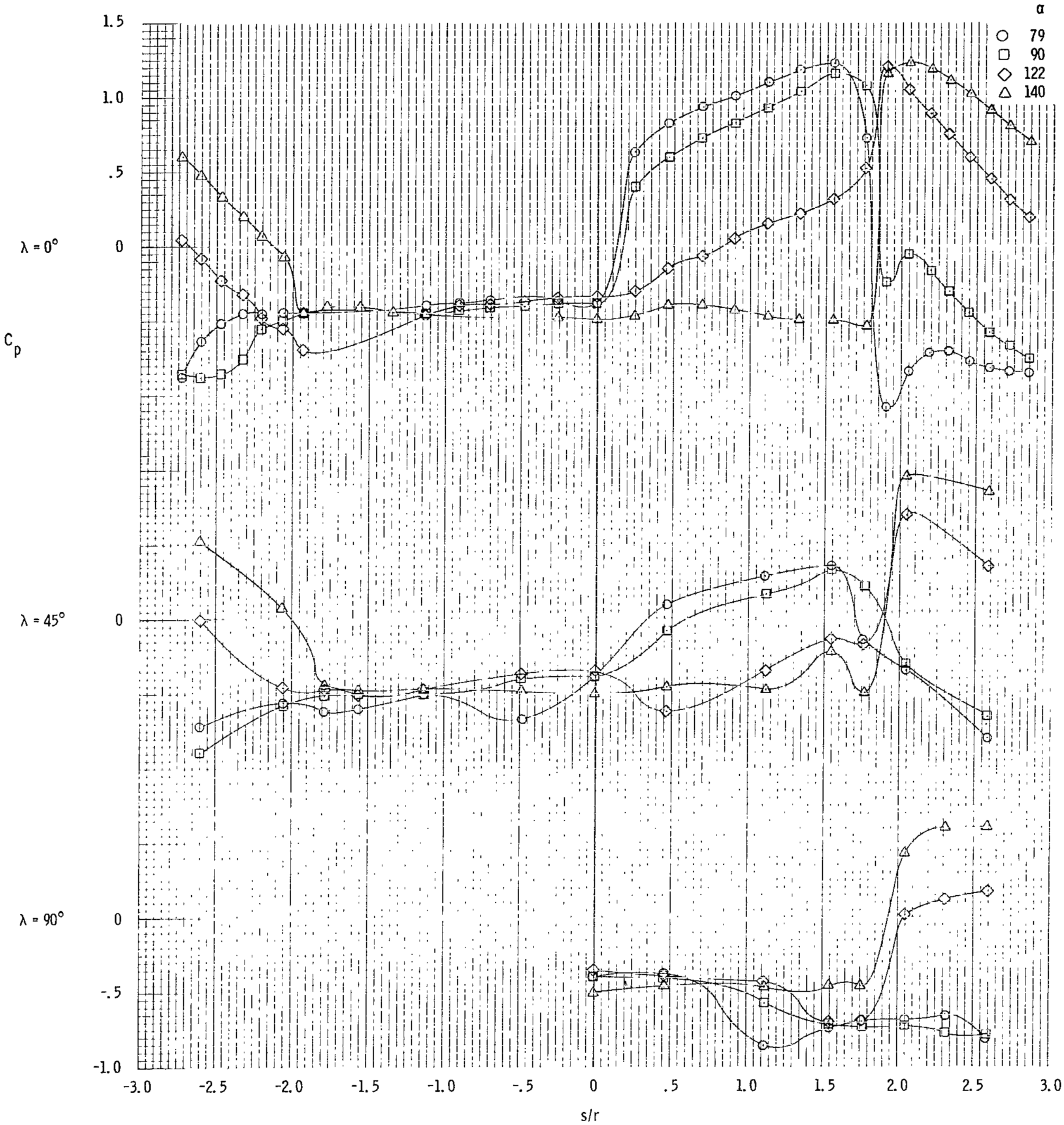

(b) $\alpha = 79^\circ$ to $\alpha = 140^\circ$.

Figure 7. - Concluded.

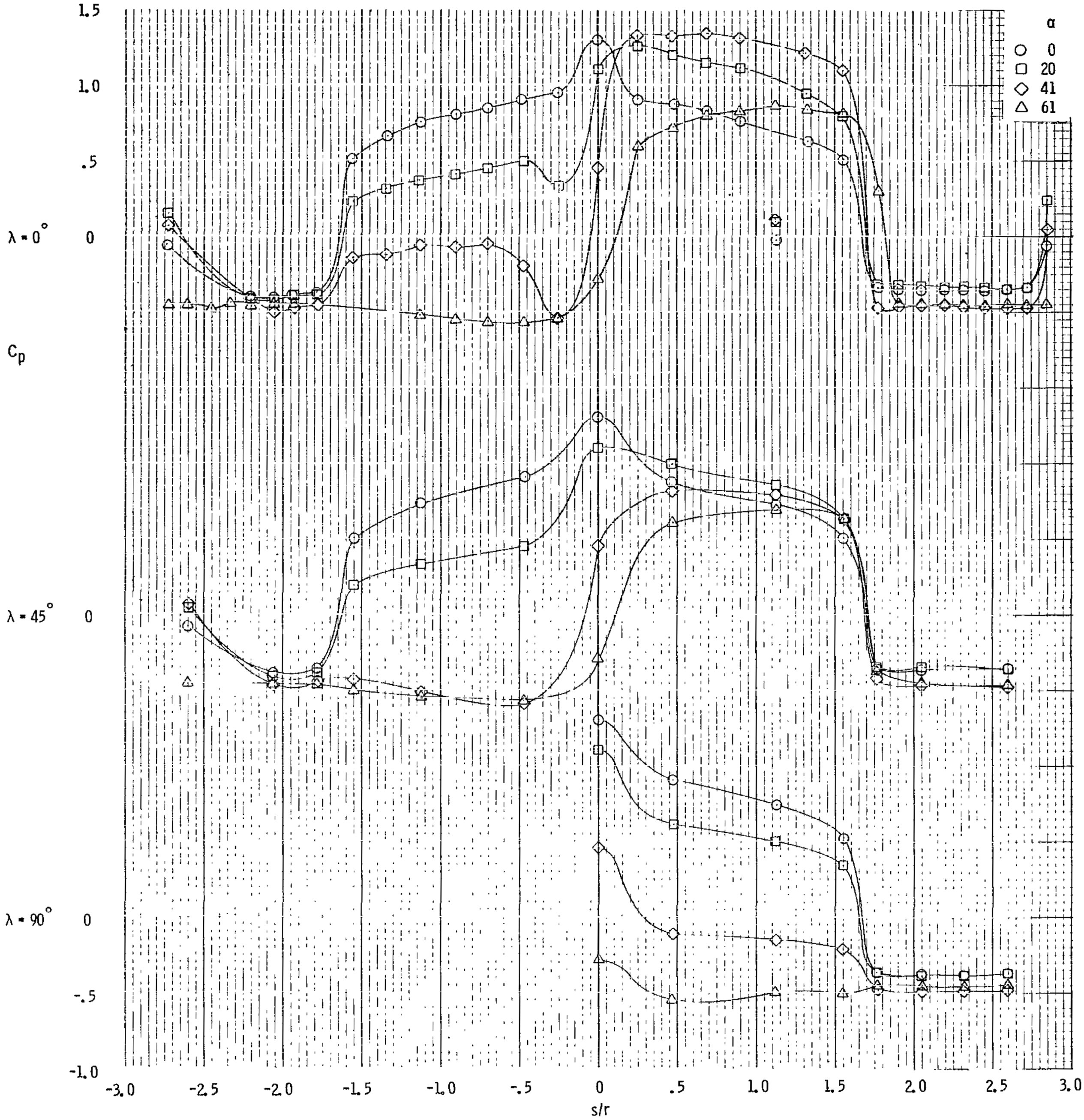

(a) $\alpha = 0°$ to $\alpha = 61°$.

Figure 8.- Variation or C_p with increasing α at $\lambda = 0°$, $\lambda = 45°$, and $\lambda = 90°$ at $M = 1.1$, 0.02-scale model, configuration C_1, apex forward, in the Ames 2×2 TWT test facility.

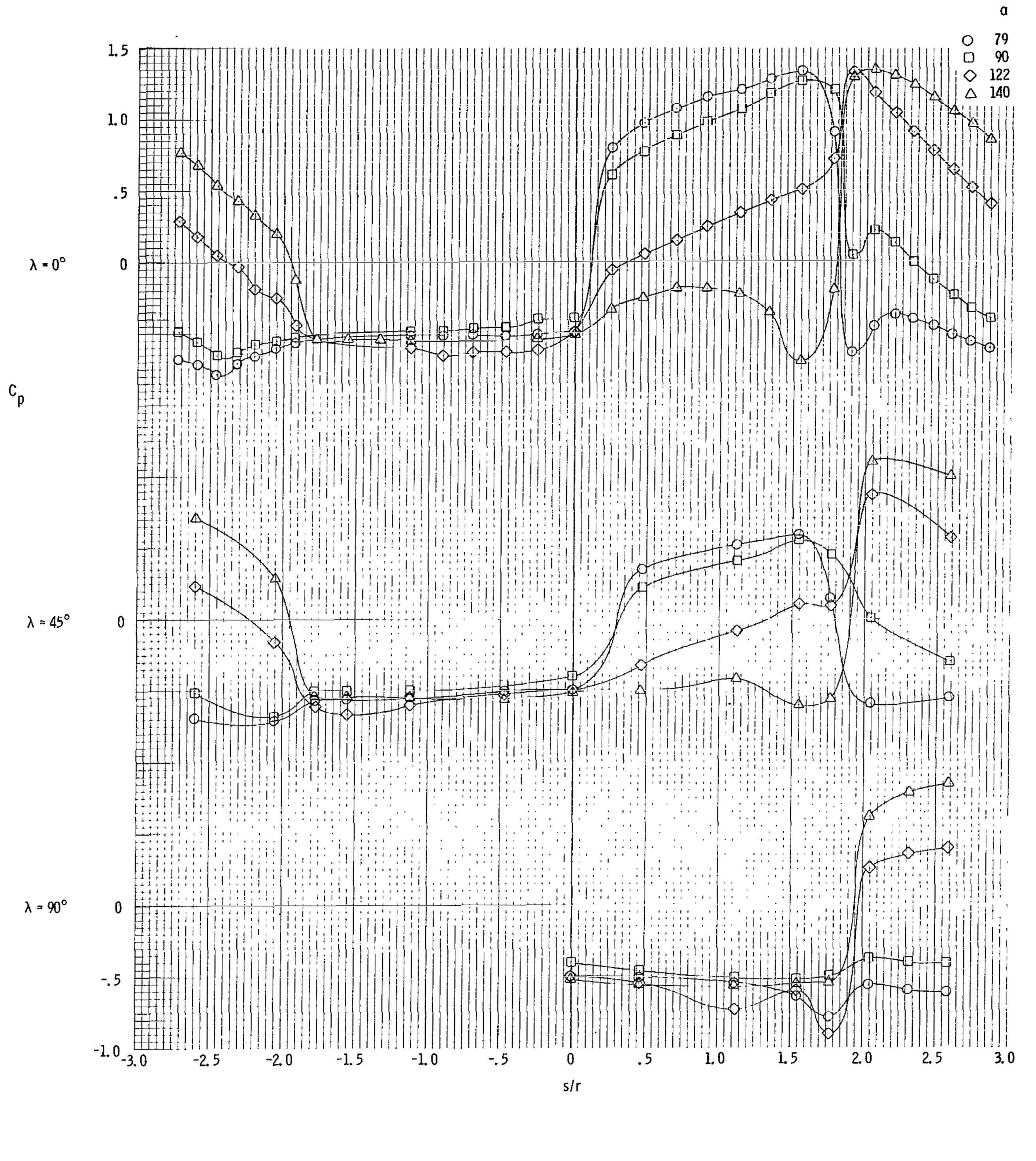

(b) $\alpha = 79°$ to $\alpha = 140°$.

Figure 8. - Concluded.

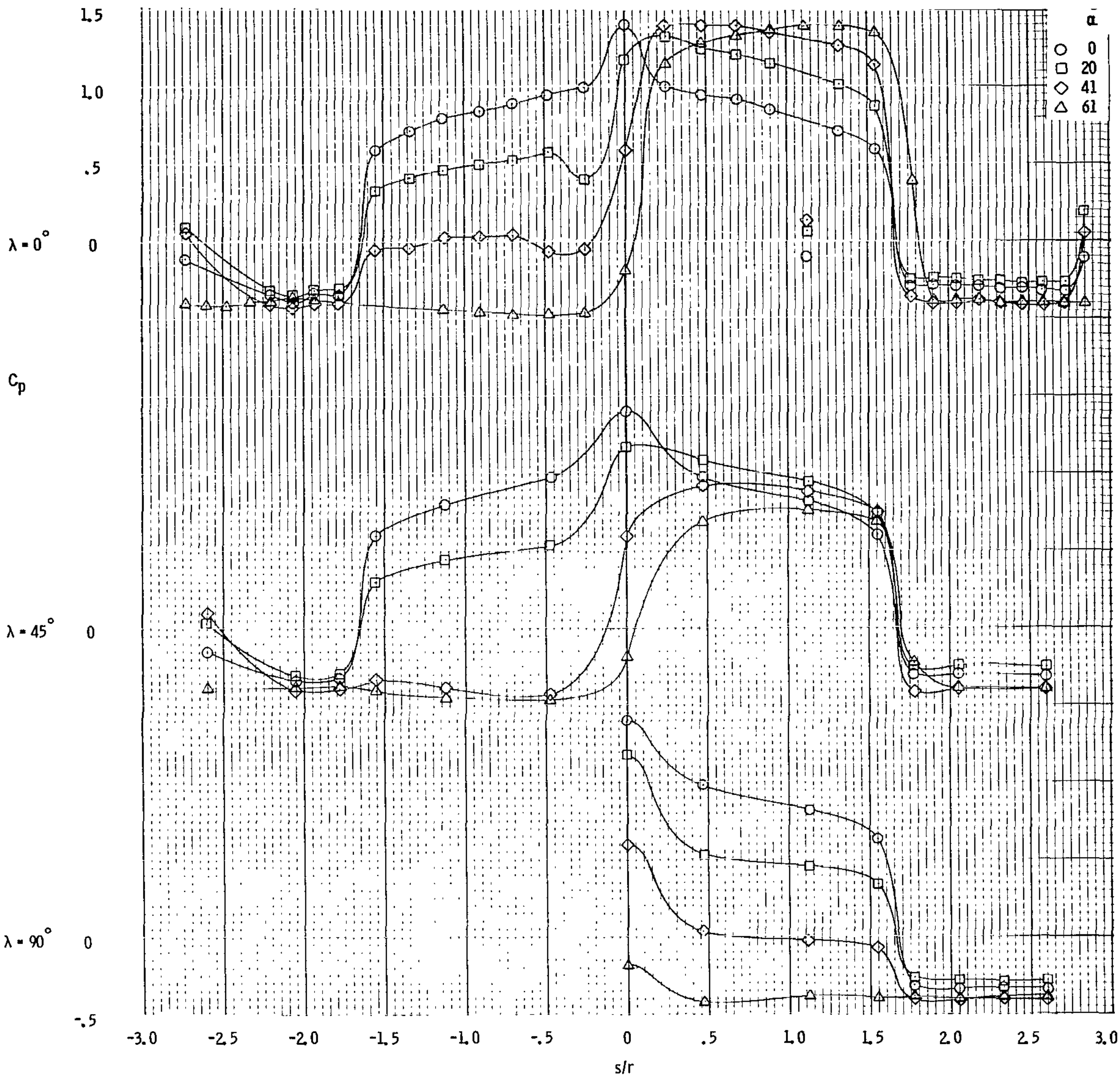

(a) $\alpha = 0°$ to $\alpha = 61°$.

Figure 9. - Variation of C_p with increasing α at $\lambda = 0°$, $\lambda = 45°$, and $\lambda = 90°$ at M = 1.2, 0.02-scale model, configuration C_1, apex forward, in the Ames 2×2 TWT test facility.

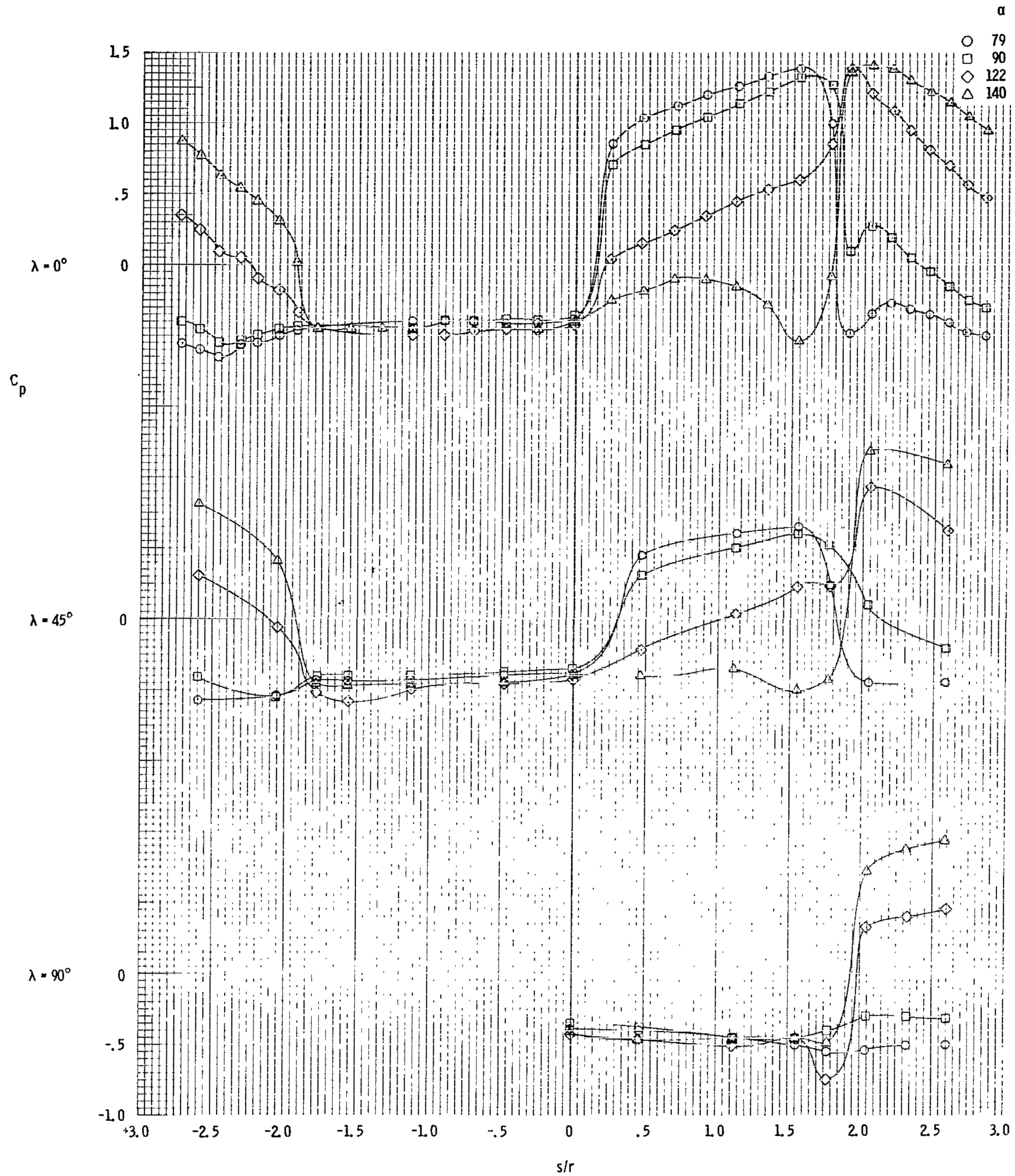

(b) $\alpha = 79°$ to $\alpha = 140°$.

Figure 9. - Concluded.

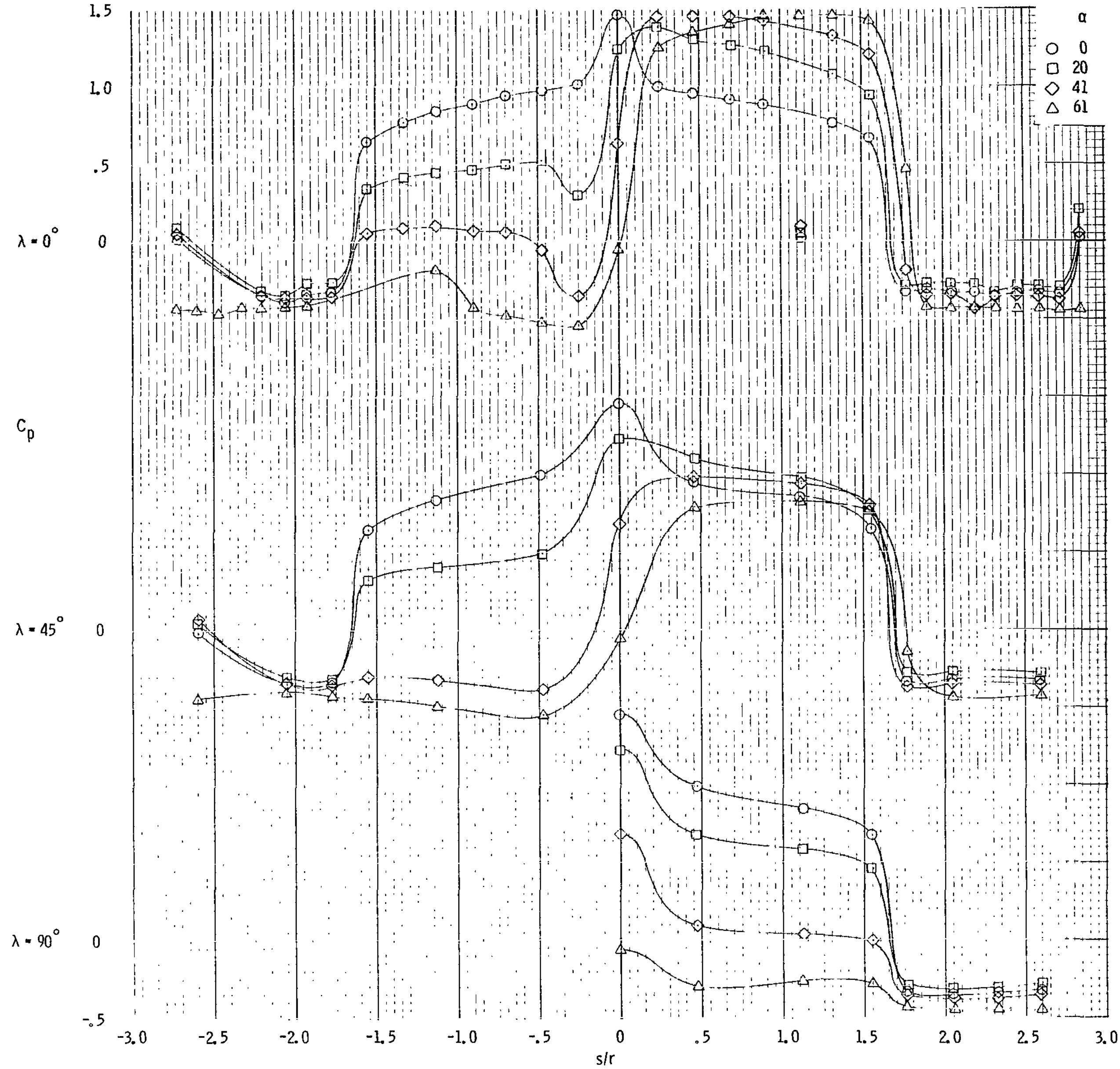

(a) $\alpha = 0°$ to $\alpha = 61°$.

Figure 10. - Variation of C_p with increasing α at $\lambda = 0°$, $\lambda = 45°$, and $\lambda = 90°$ at $M = 1.34$, 0.02-scale model, configuration C_1, apex forward, in the Ames 2×2 TWT test facility.

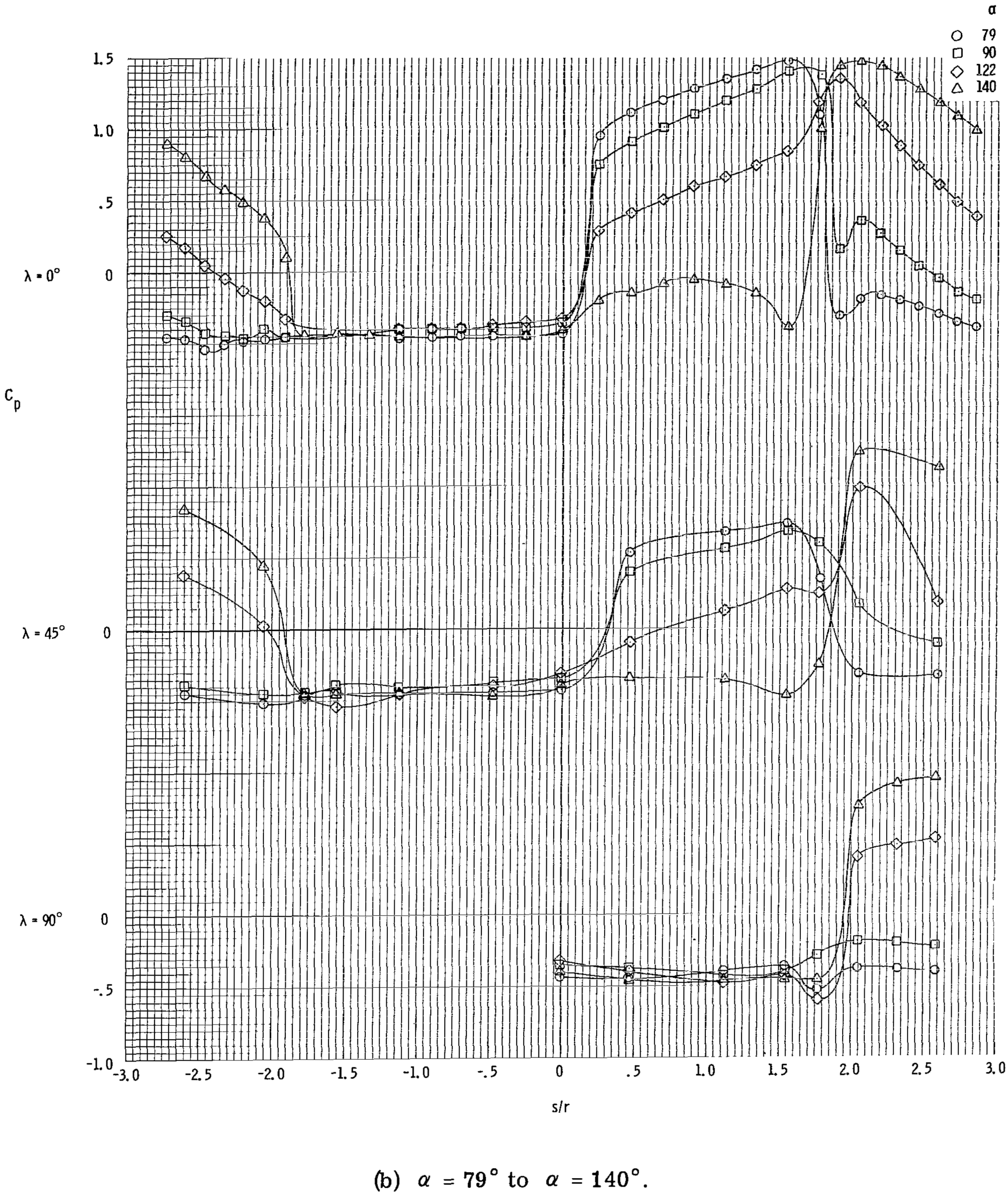

(b) $\alpha = 79°$ to $\alpha = 140°$.

Figure 10. - Concluded.

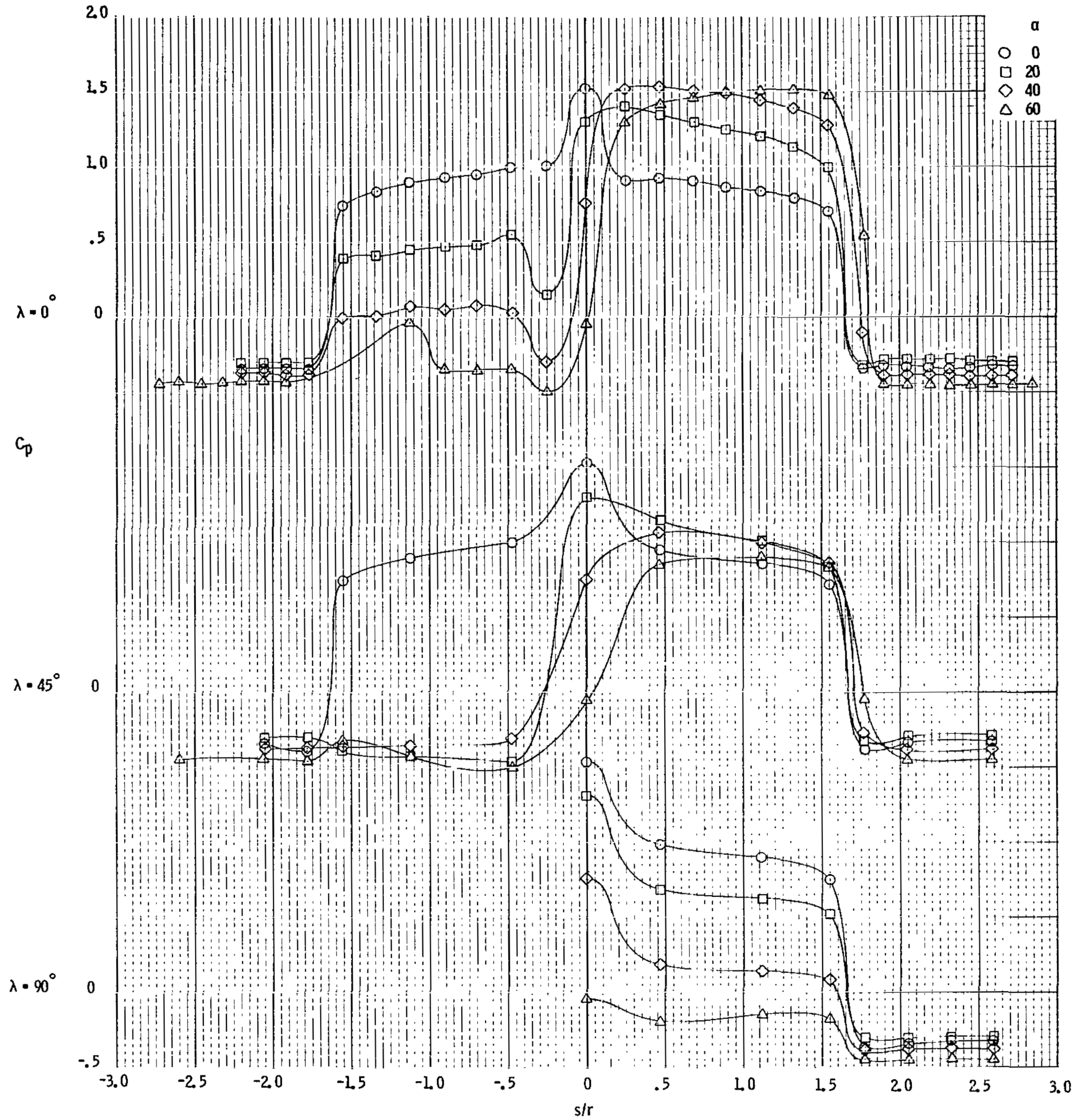

(a) $\alpha = 0°$ to $\alpha = 60°$.

Figure 11. - Variation of C_p with increasing α at $\lambda = 0°$, $\lambda = 45°$, and $\lambda = 90°$ at $M = 1.48$, 0.02-scale model, configuration C_1, apex forward, in the JPL-20SWT test facility.

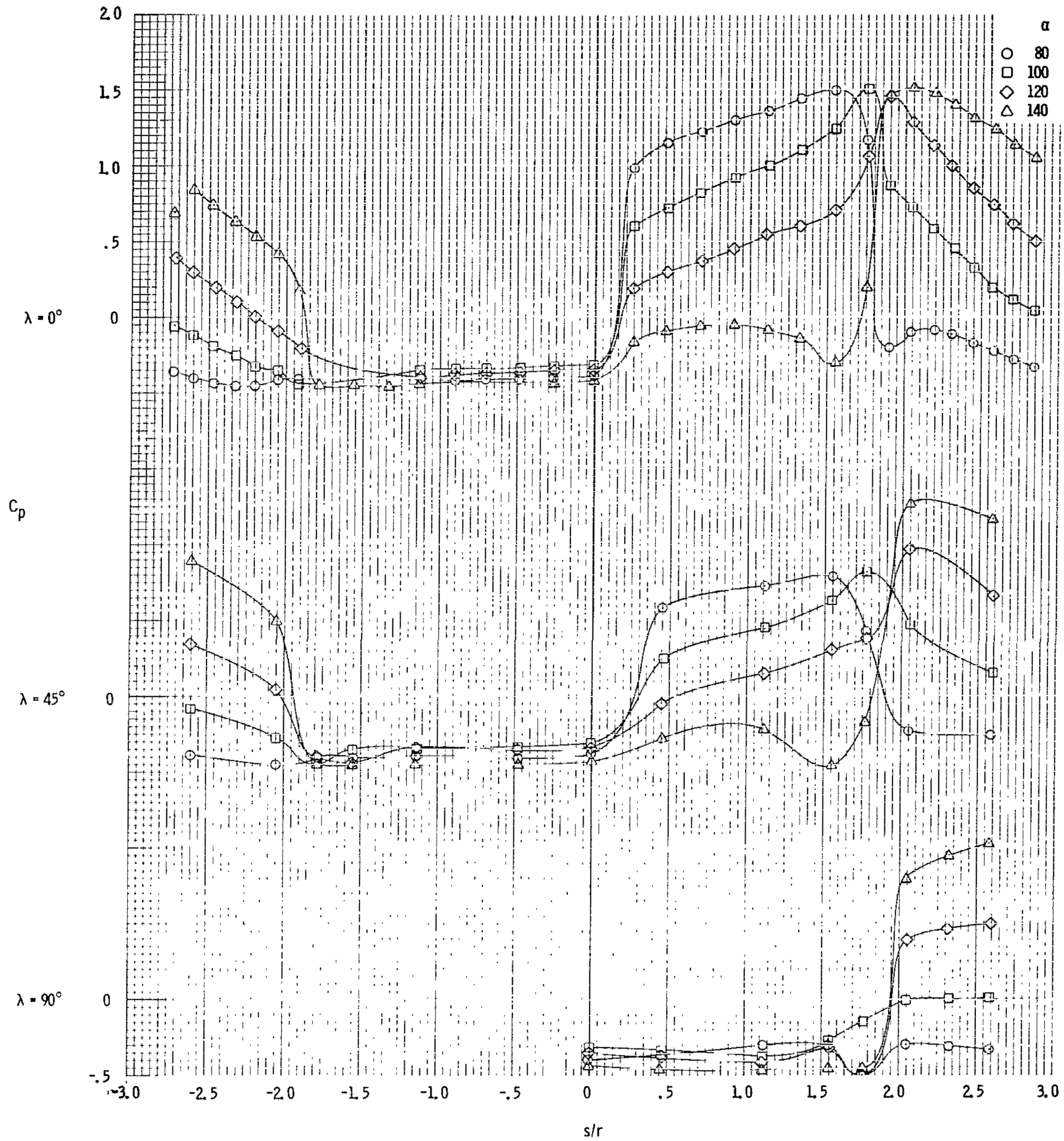

(b) $\alpha = 80°$ to $\alpha = 140°$.

Figure 11. - Concluded.

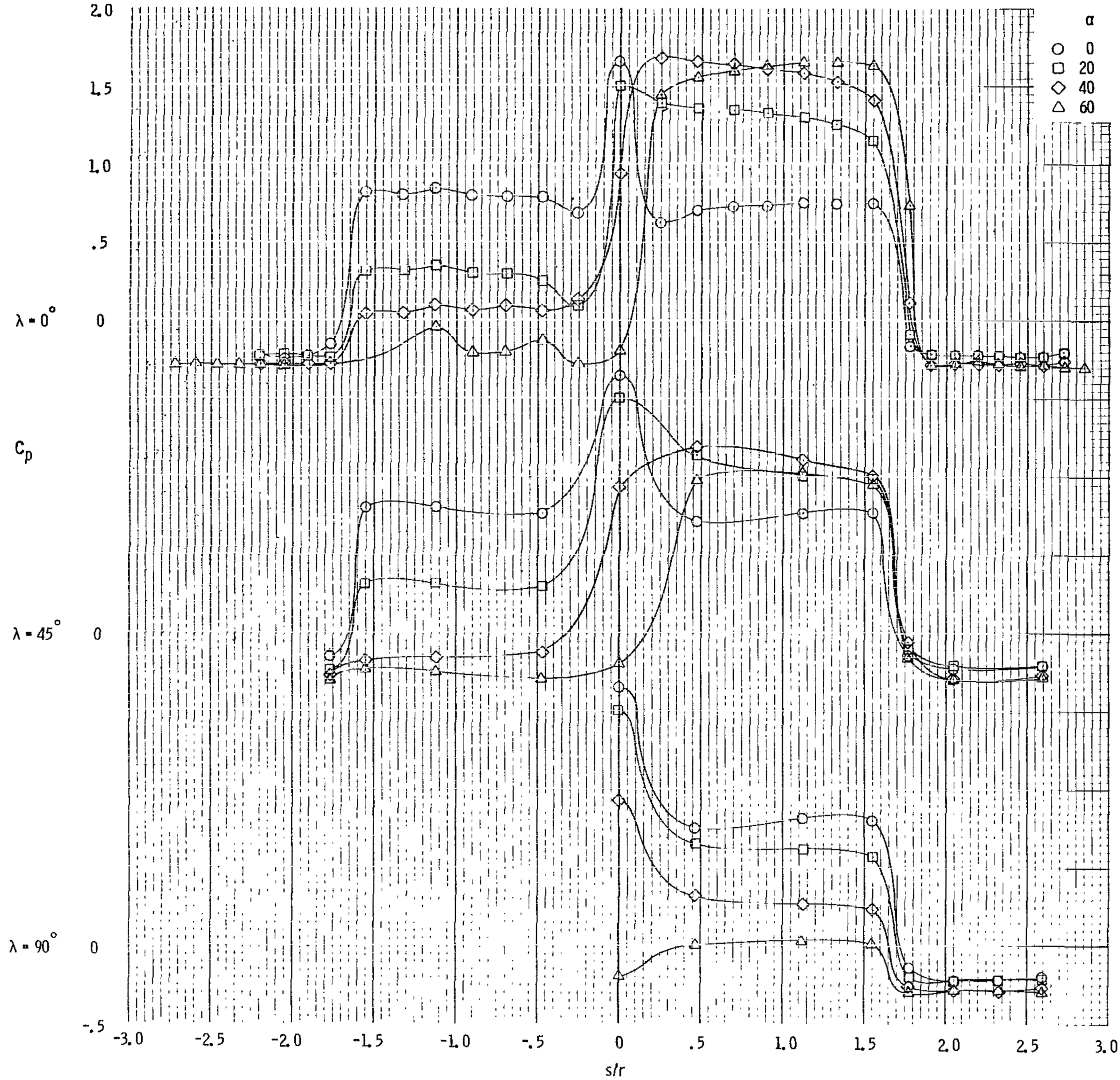

(a) $\alpha = 0°$ to $\alpha = 60°$.

Figure 12. - Variation of C_p with increasing α at $\lambda = 0°$, $\lambda = 45°$, and $\lambda = 90°$ at $M = 2.01$, 0.02-scale model, configuration C_1, apex forward, in the JPL-20SWT test facility.

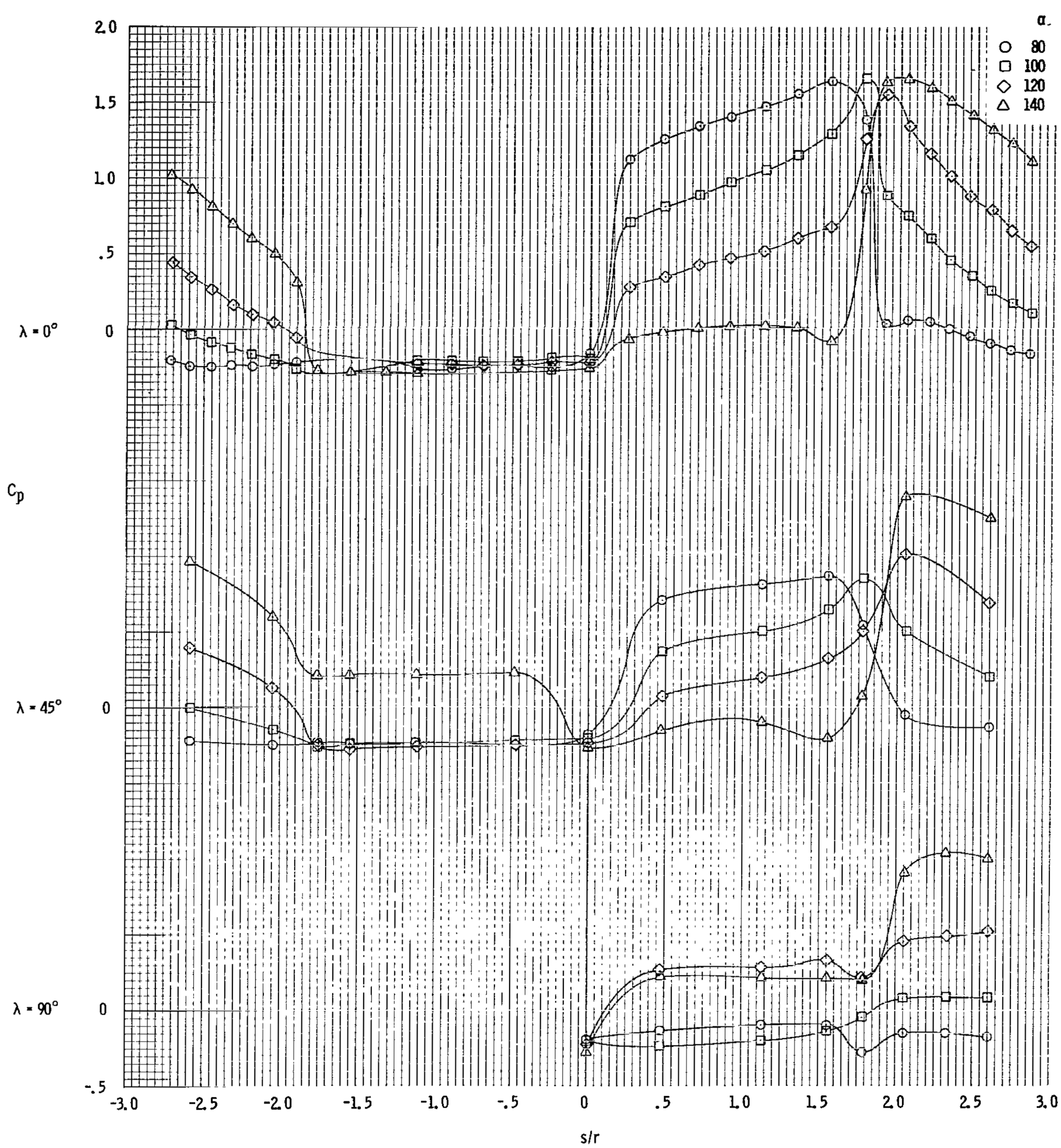

(b) $\alpha = 80°$ to $\alpha = 140°$.

Figure 12. - Concluded.

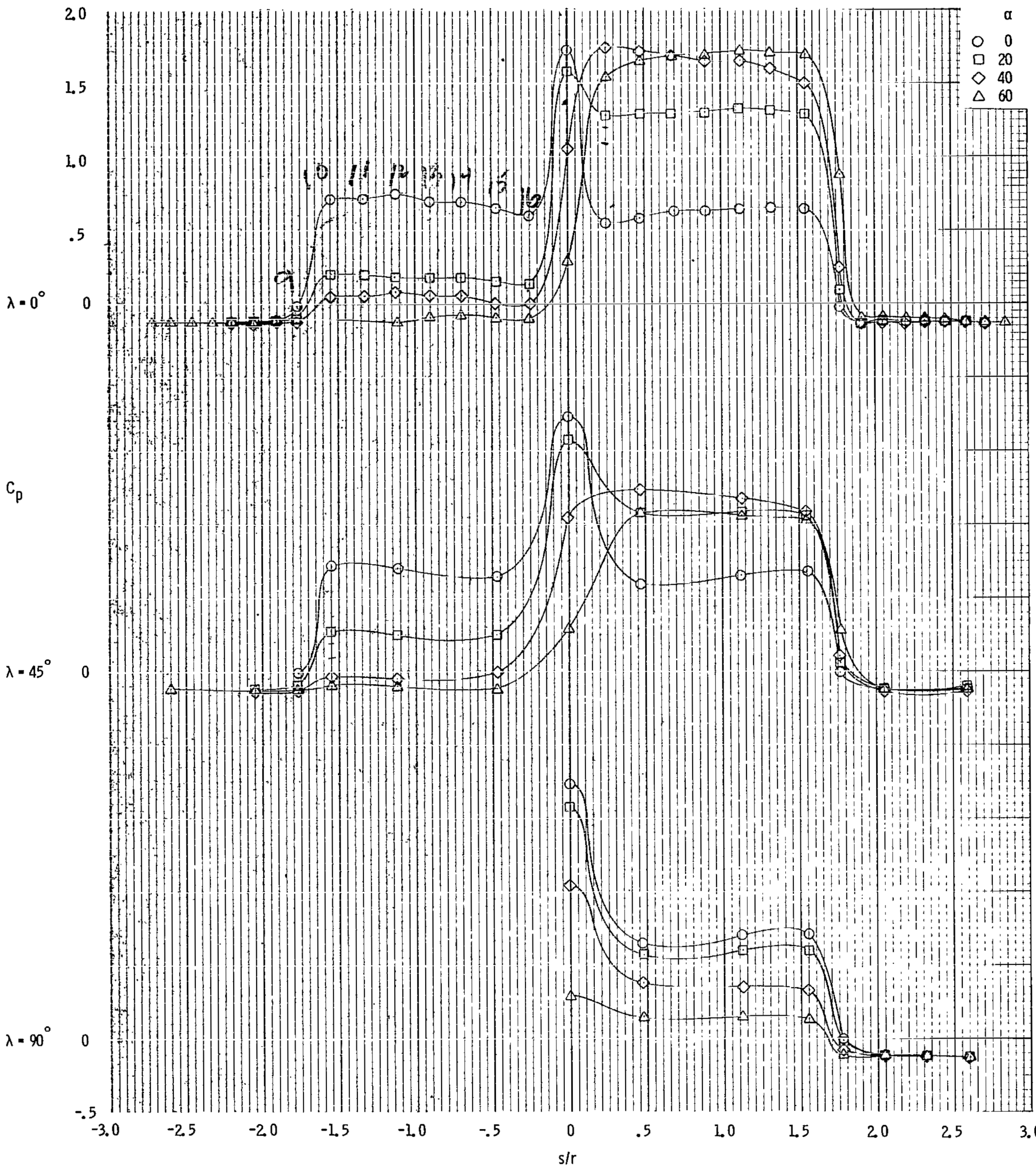

(a) $\alpha = 0°$ to $\alpha = 60°$.

Figure 13. - Variation of C_p with increasing α at $\lambda = 0°$, $\lambda = 45°$, and $\lambda = 90°$ at $M = 3.01$, 0.02-scale model, configuration C_1, apex forward, in the JPL-20SWT test facility.

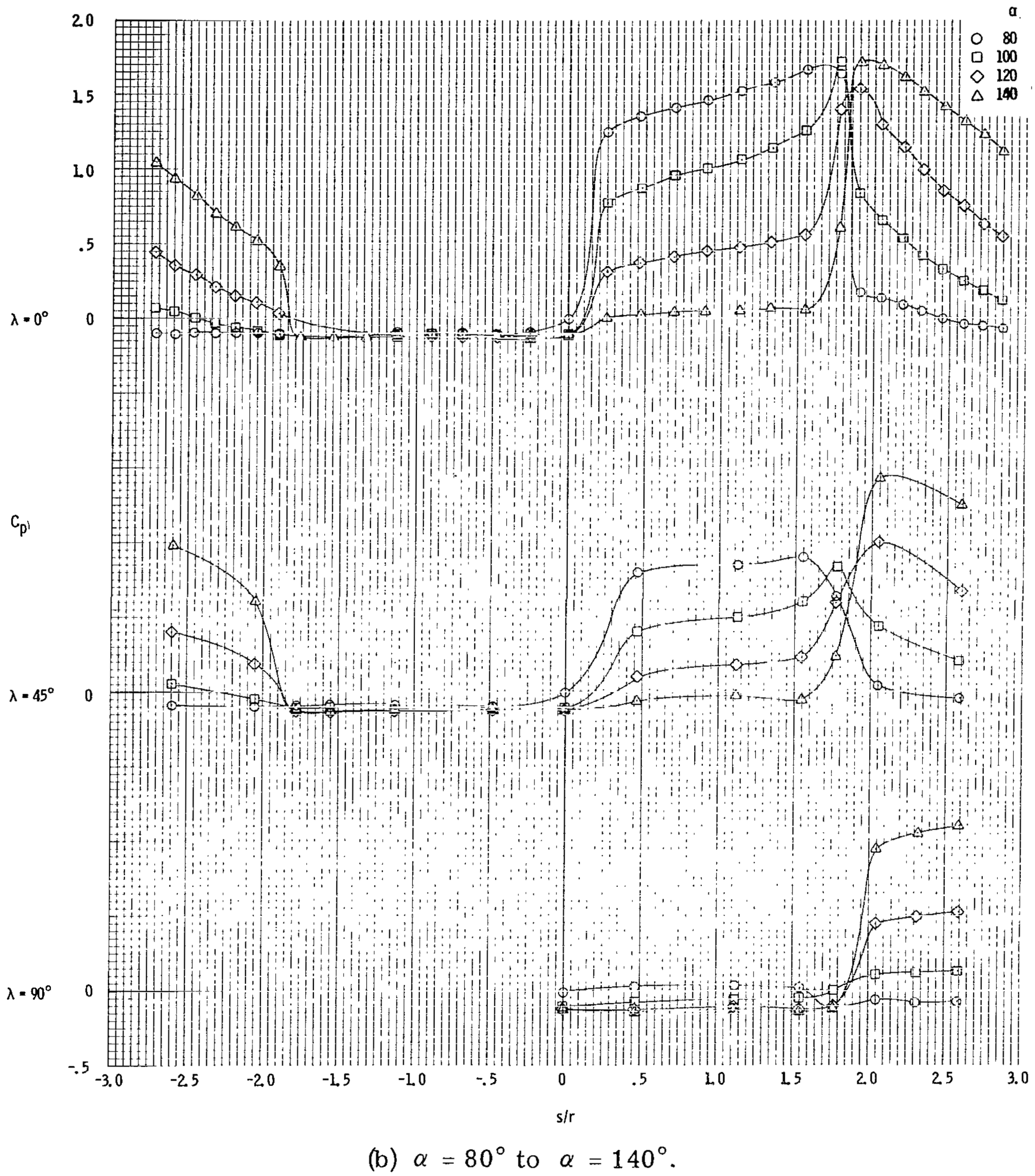

(b) $\alpha = 80°$ to $\alpha = 140°$.

Figure 13. - Concluded.

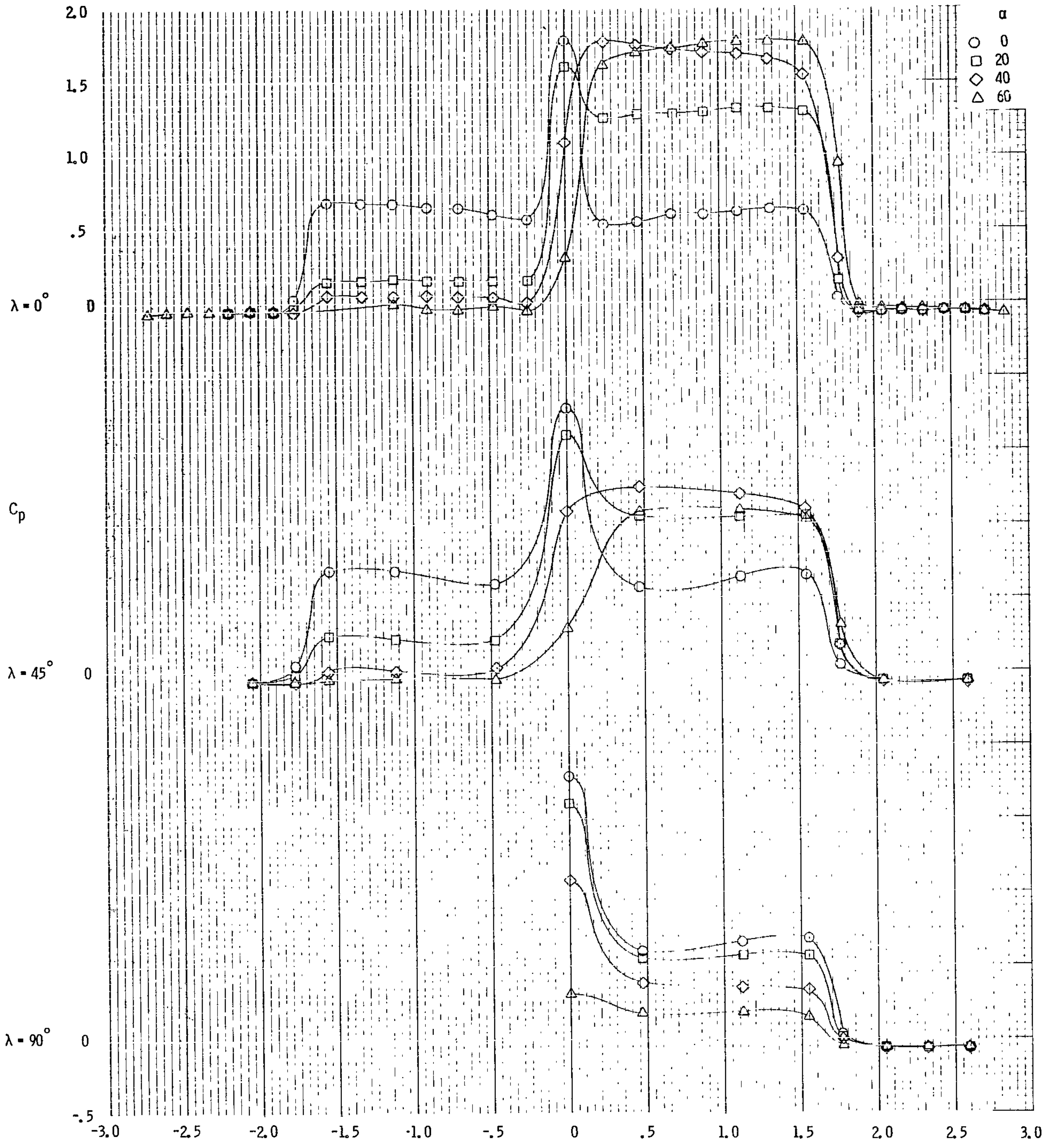

(a) $\alpha = 0°$ to $\alpha = 60°$.

Figure 14. - Variation of C_p with increasing α at $\lambda = 0°$, $\lambda = 45°$, and $\lambda = 90°$ at $M = 3.99$, 0.02-scale model, configuration C_1, apex forward, in the JPL-20SWT test facility.

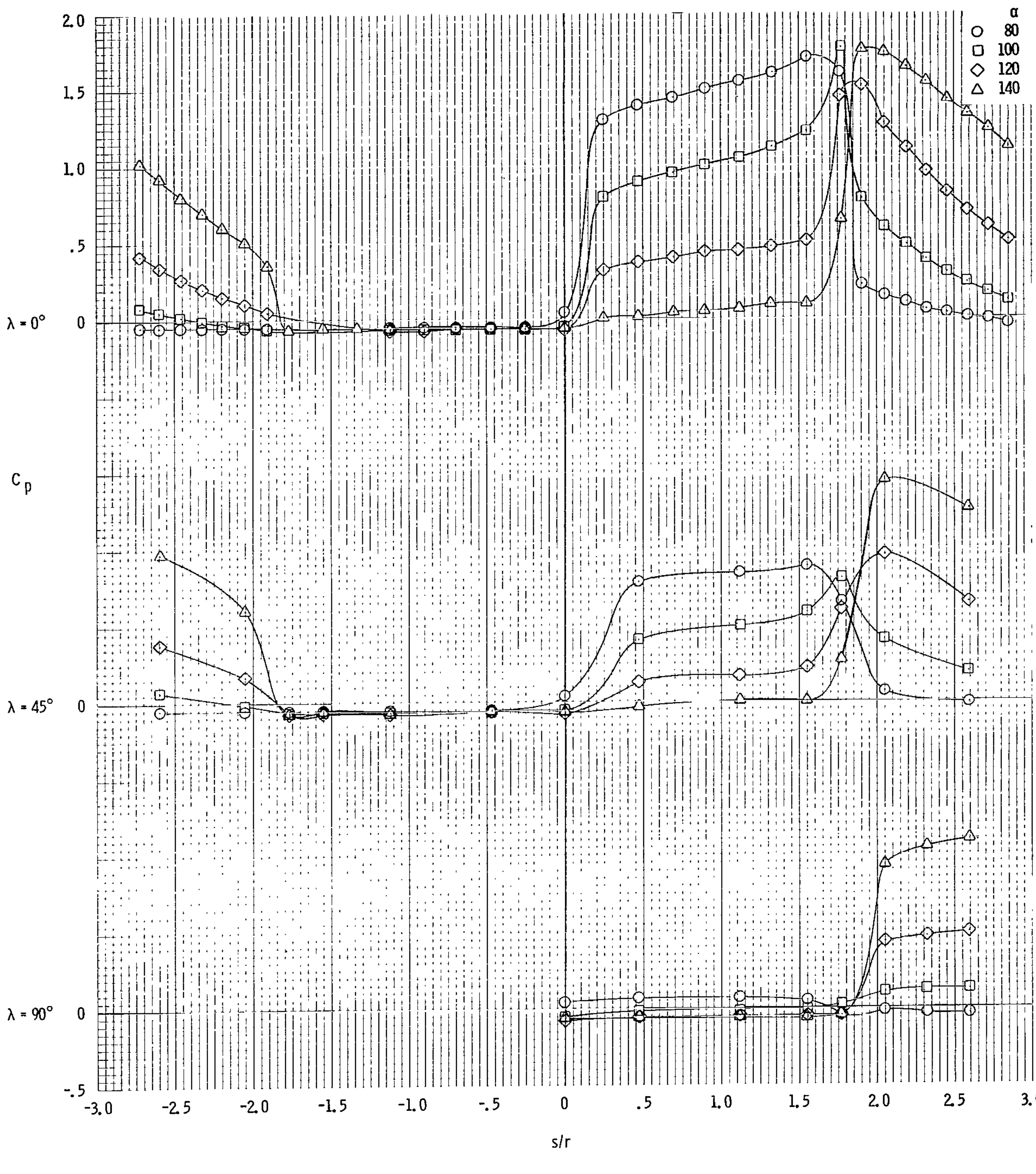

(b) $\alpha = 80^\circ$ to $\alpha = 140^\circ$.

Figure 14. - Concluded.

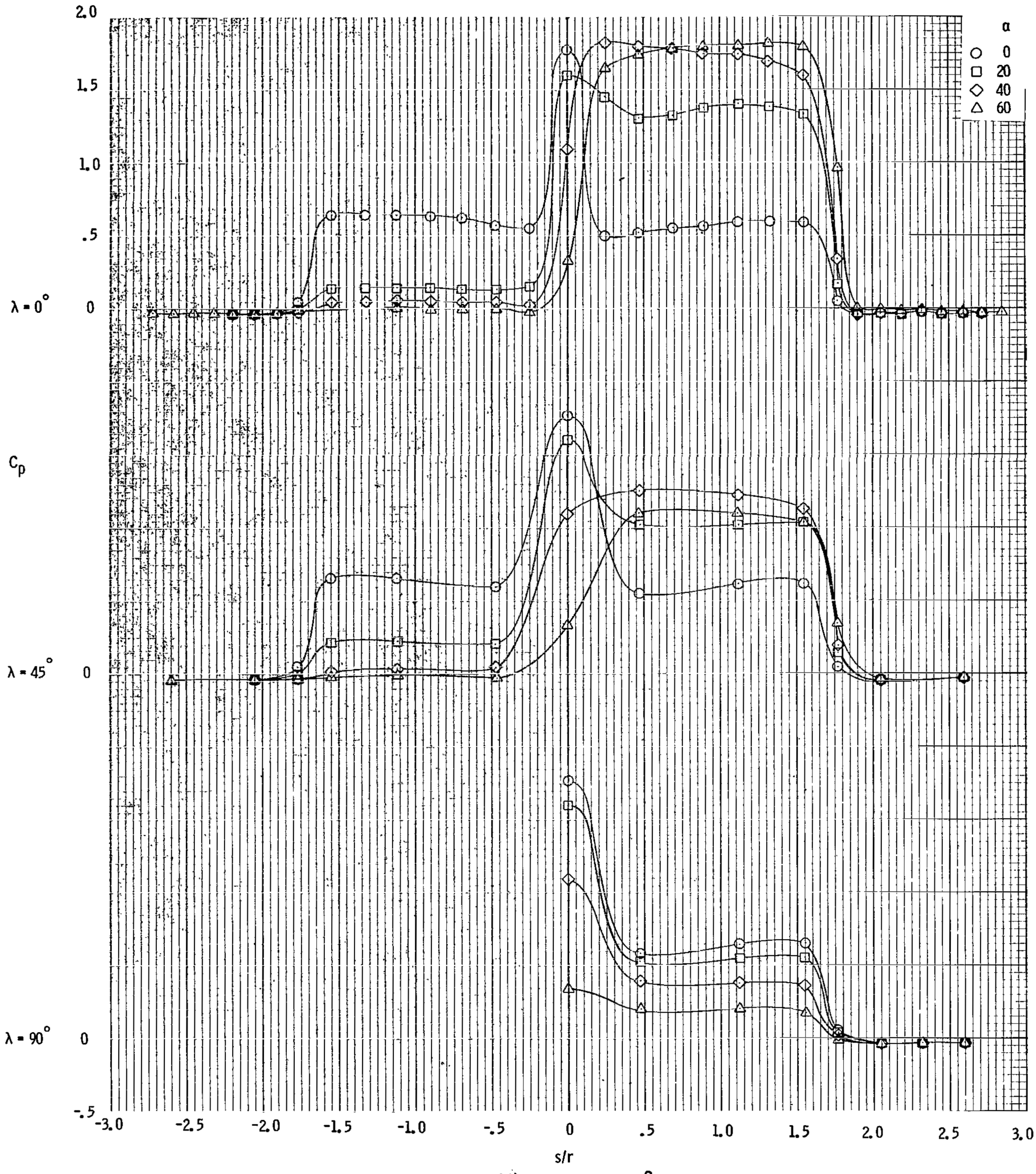

(a) $\alpha = 0°$ to $\alpha = 60°$.

Figure 15. - Variation of C_p with increasing α at $\lambda = 0°$, $\lambda = 45°$, and $\lambda = 90°$ at $M = 5.01$, 0.02-scale model, configuration C_1, apex forward, in the JPL-20SWT test facility.

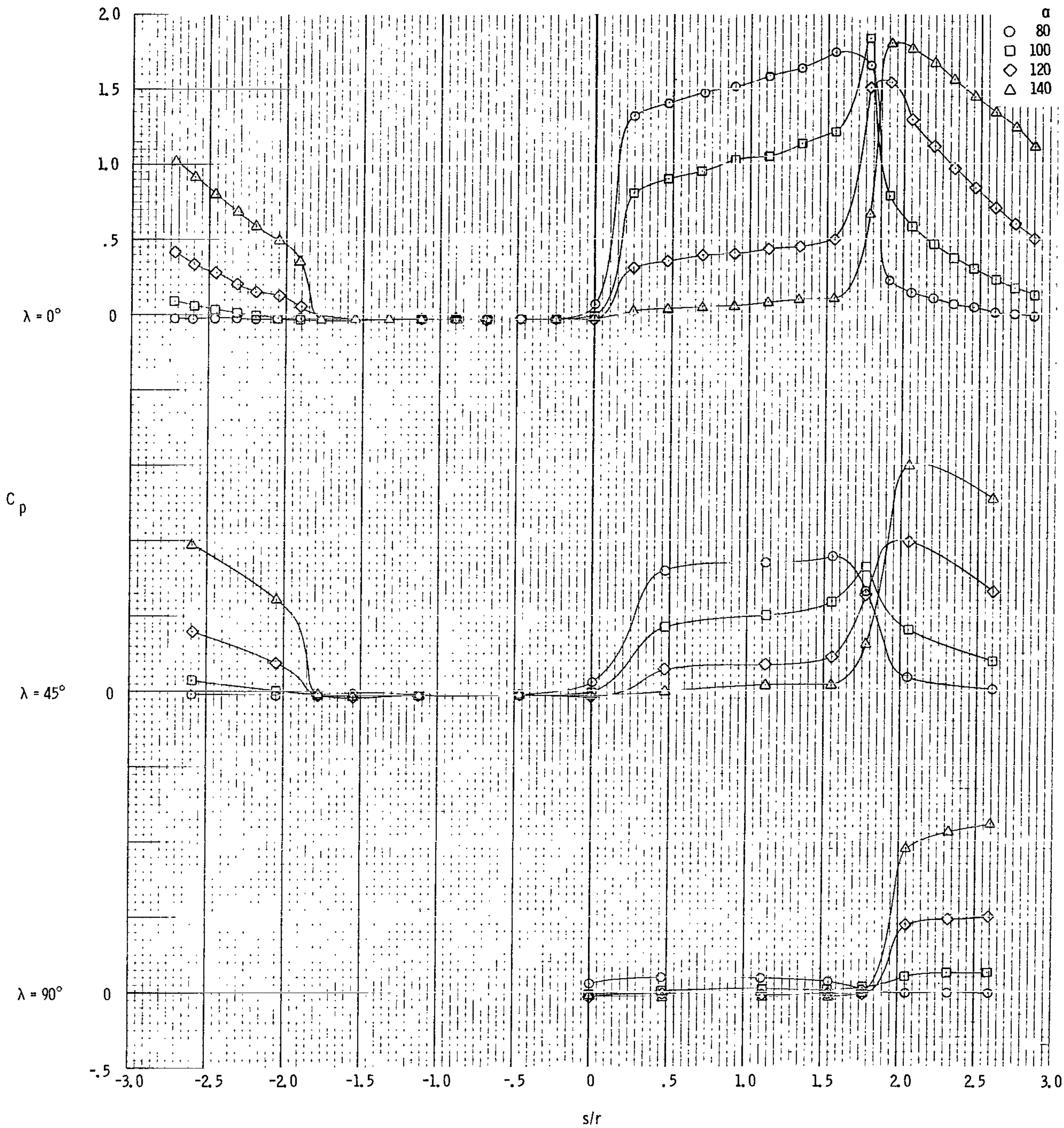

(b) $\alpha = 80^\circ$ to $\alpha = 140^\circ$.

Figure 15. - Concluded.

(a) $\alpha = 0°$ to $\alpha = 60°$.

Figure 16. - Variation of C_p with increasing α at $\lambda = 0°$, $\lambda = 45°$, and $\lambda = 90°$ at M = 7.35, 0.02-scale model, configuration C_1, apex forward, in the JPL-21HWT test facility.

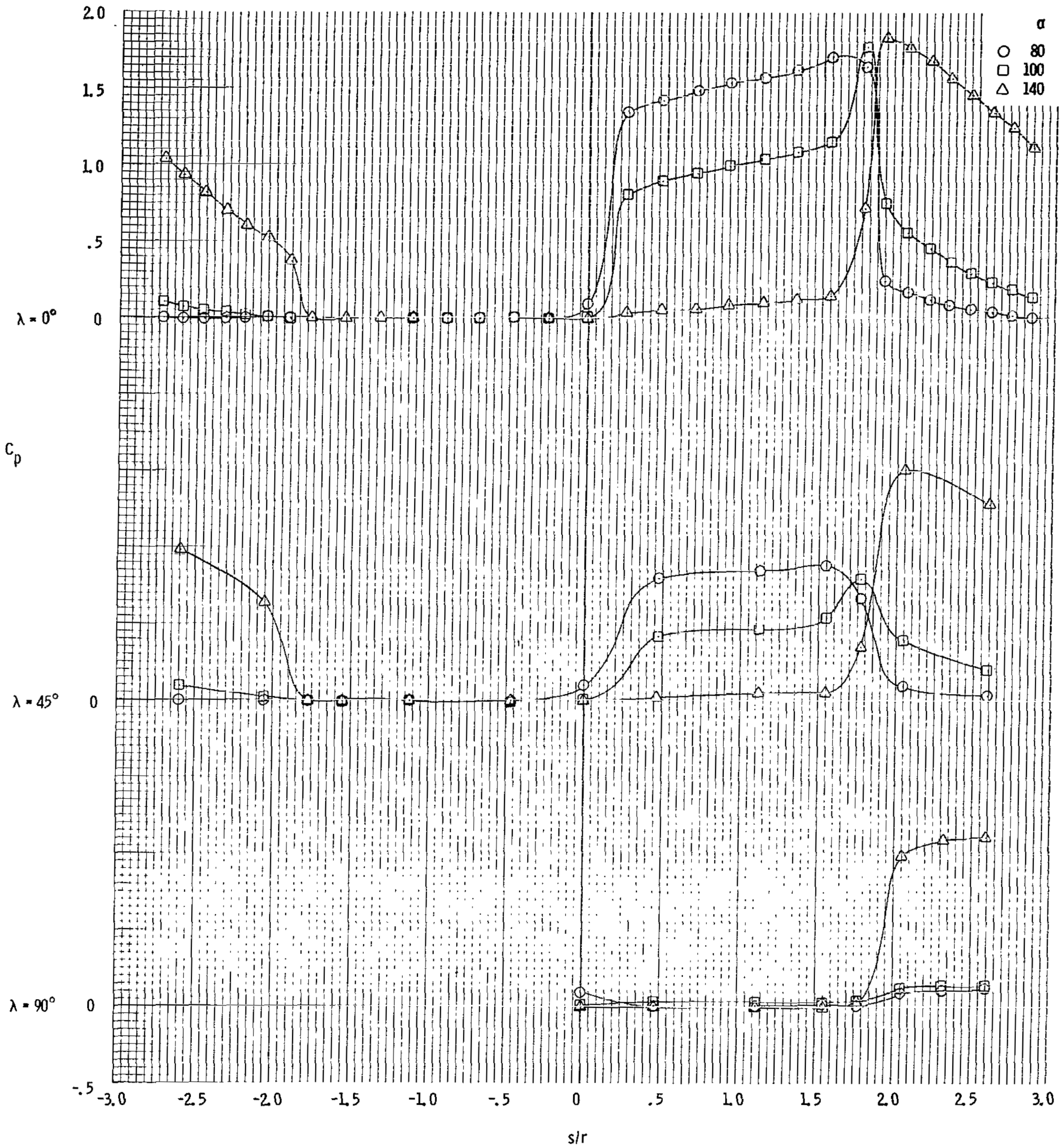

(b) $\alpha = 80^\circ$ to $\alpha = 140^\circ$.

Figure 16. - Concluded.

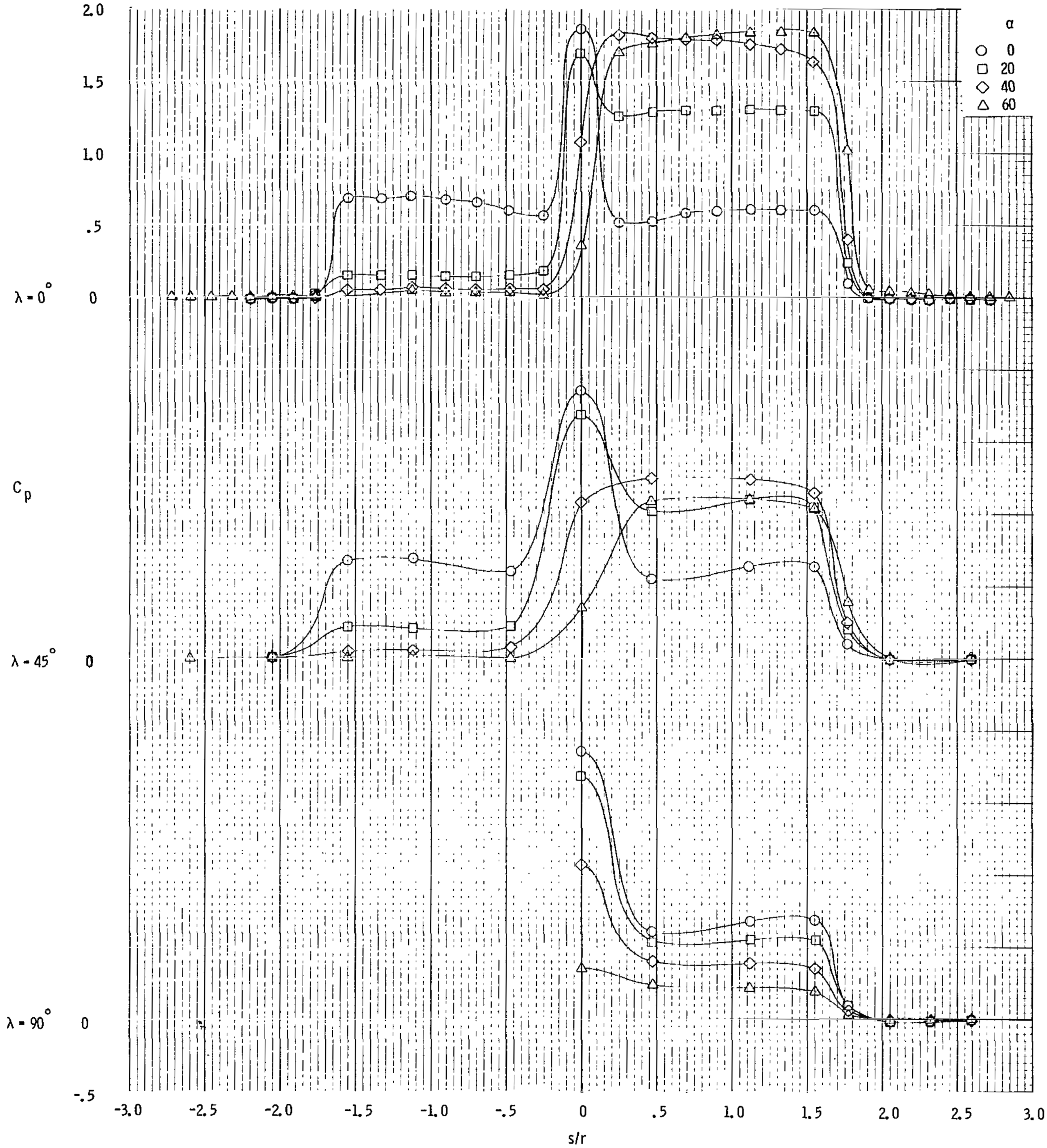

(a) $\alpha = 0°$ to $\alpha = 60°$.

Figure 17. - Variation of C_p with increasing α at $\lambda = 0°$, $\lambda = 45°$, and $\lambda = 90°$ at M = 9.08, 0.02-scale model, configuration C_1, apex forward, in the JPL-21HWT test facility.

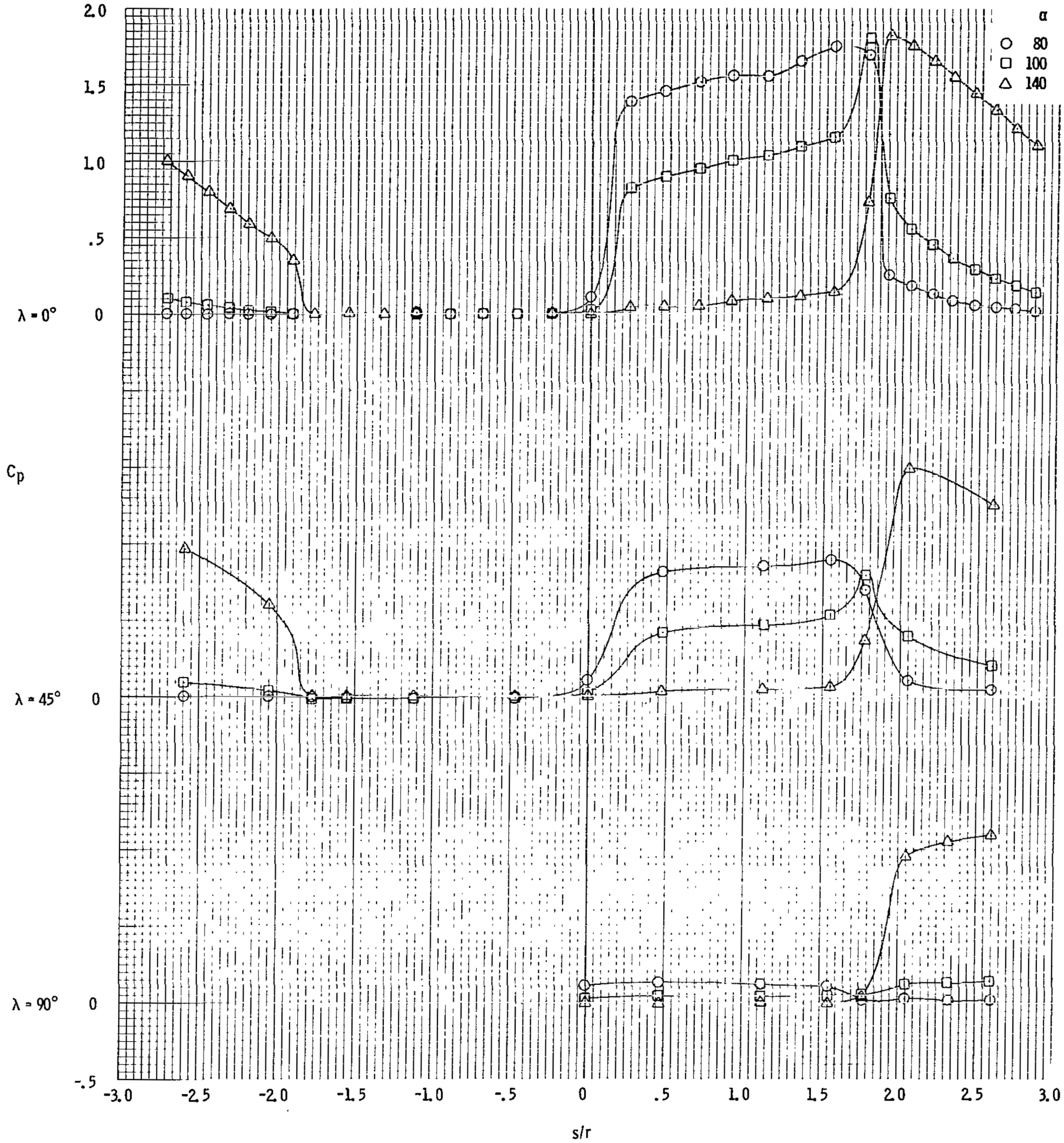

(b) $\alpha = 80°$ to $\alpha = 140°$.

Figure 17. - Concluded.

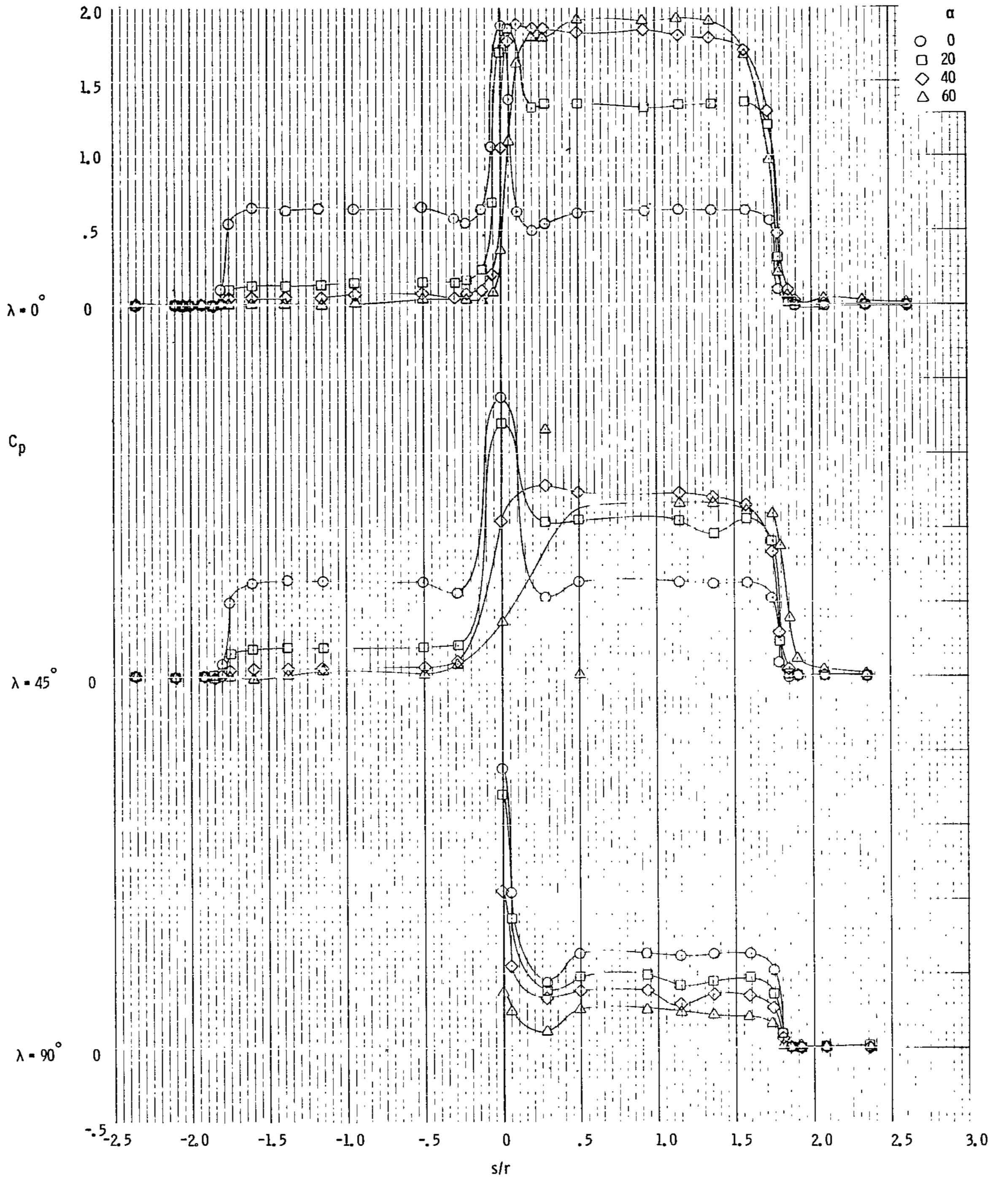

(a) $\alpha = 0°$ to $\alpha = 60°$ at $M = 10.1$, C_2.

Figure 18. - Variation of C_p with increasing α at $\lambda = 0°$, $\lambda = 45°$, and $\lambda = 90°$, 0.045-scale model, apex forward, in the AEDC-C test facility.

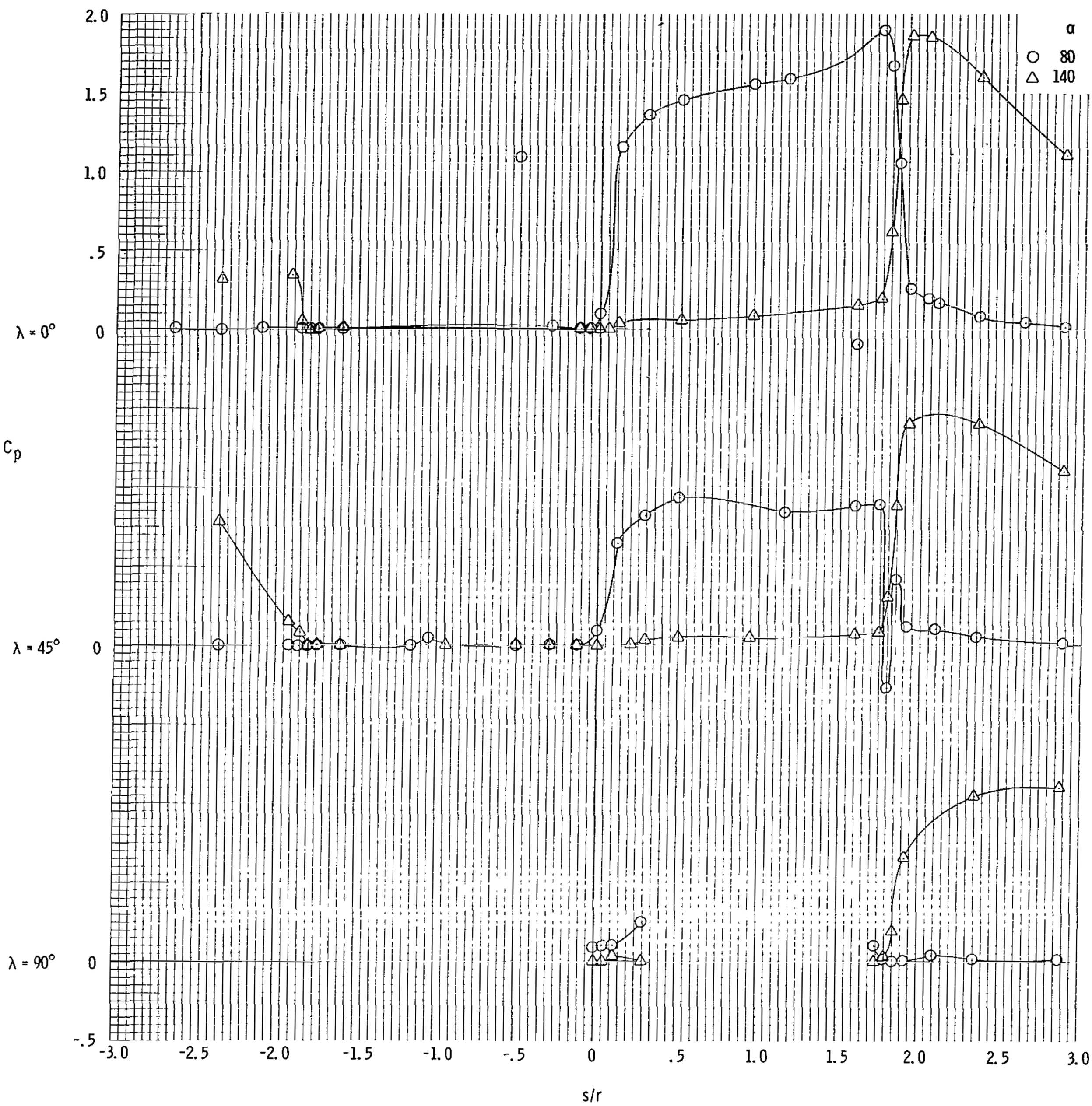

(b) $\alpha = 80°$ to $\alpha = 140°$ at M = 10.0, $C_{38}L_{28}$.

Figure 18. - Concluded.

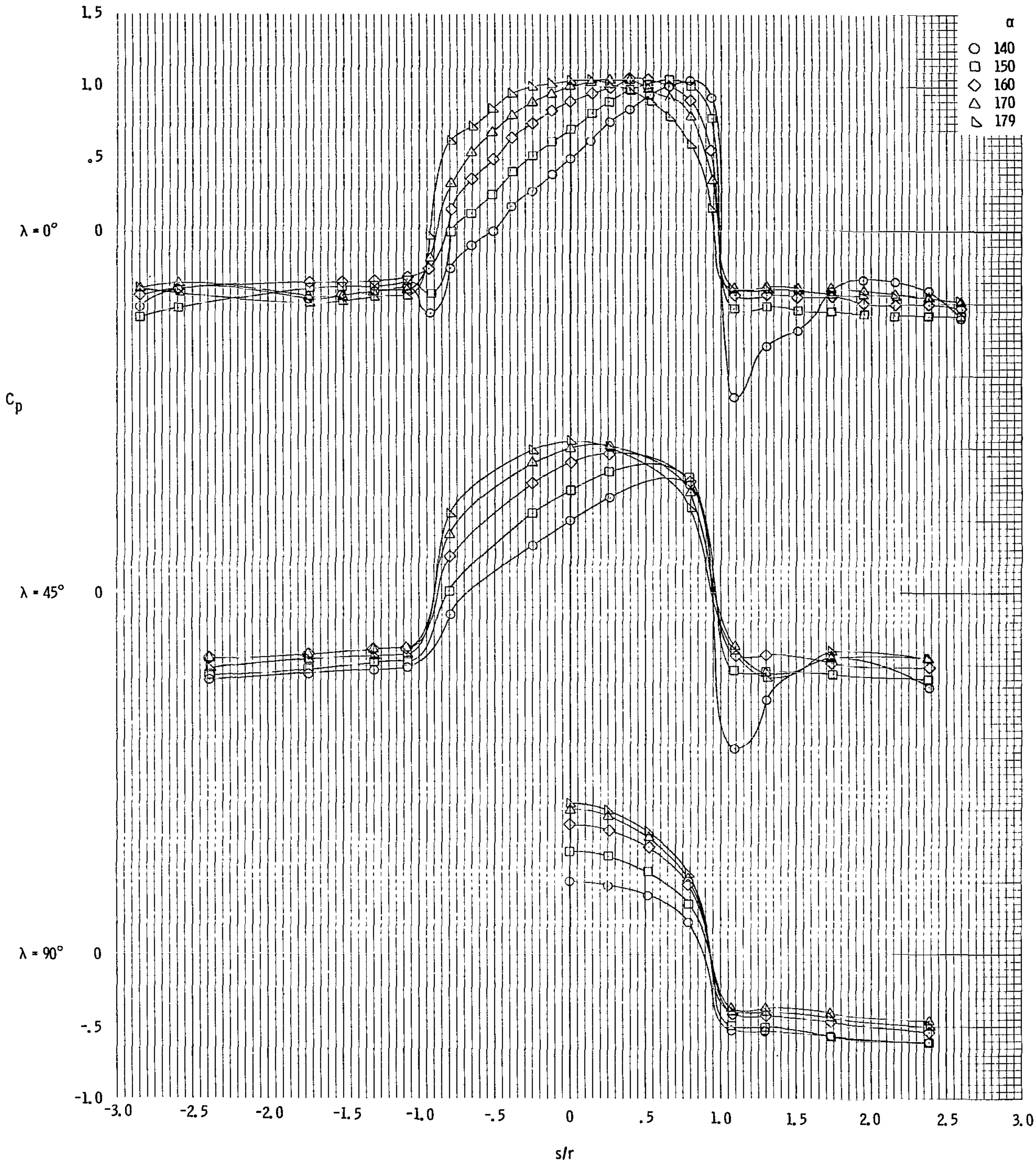

Figure 19. - Variation of C_p with increasing α at $\lambda = 0°$, $\lambda = 45°$, and $\lambda = 90°$ at M = 0.4, 0.02-scale model, configuration C_1, heat shield forward, in the Ames 2×2 TWT test facility.

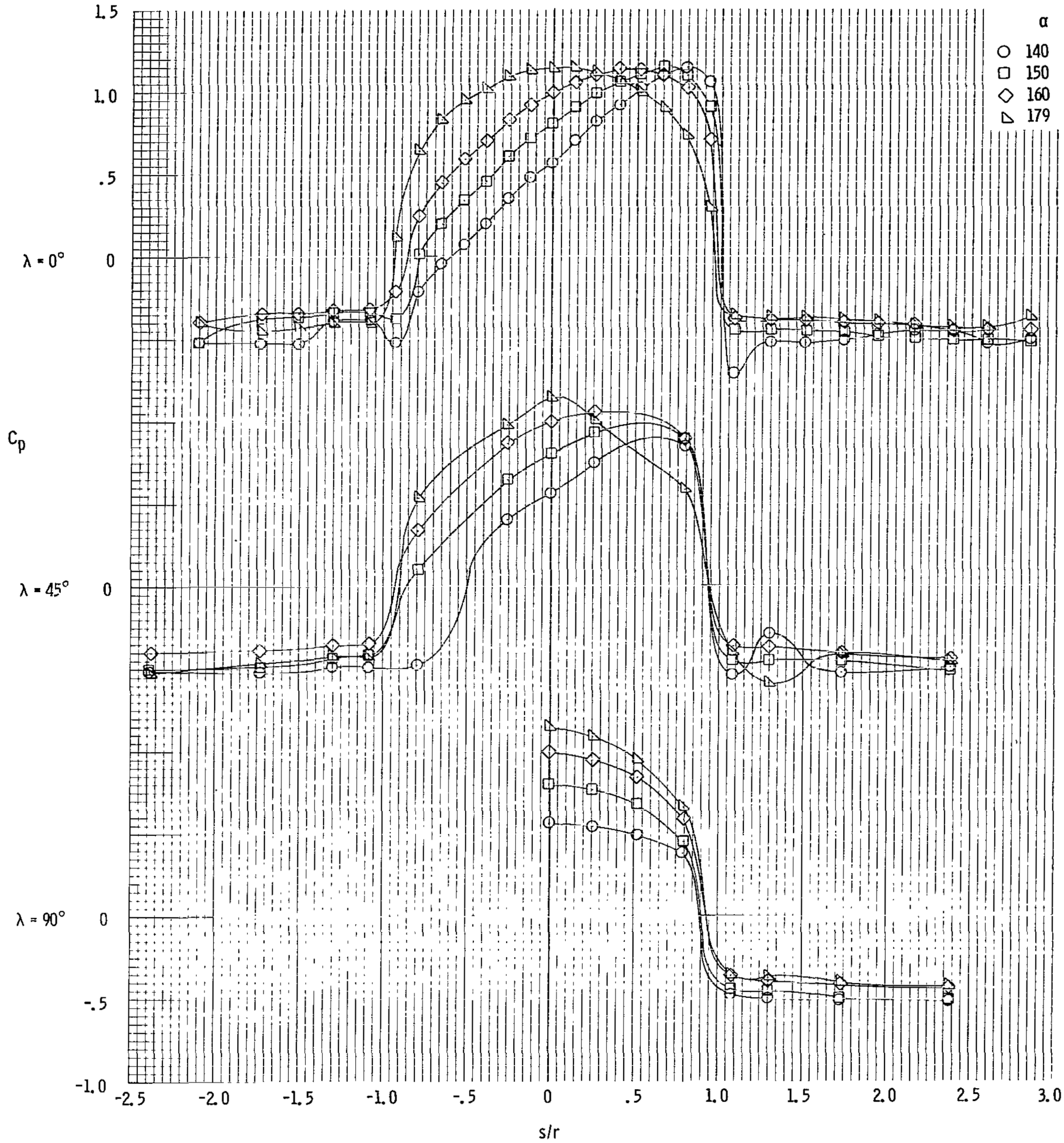

Figure 20. - Variation of C_p with increasing α at $\lambda = 0°$, $\lambda = 45°$, and $\lambda = 90°$ at M = 0.7, 0.02-scale model, configuration C_1, heat shield forward, in the Ames 2×2 TWT test facility.

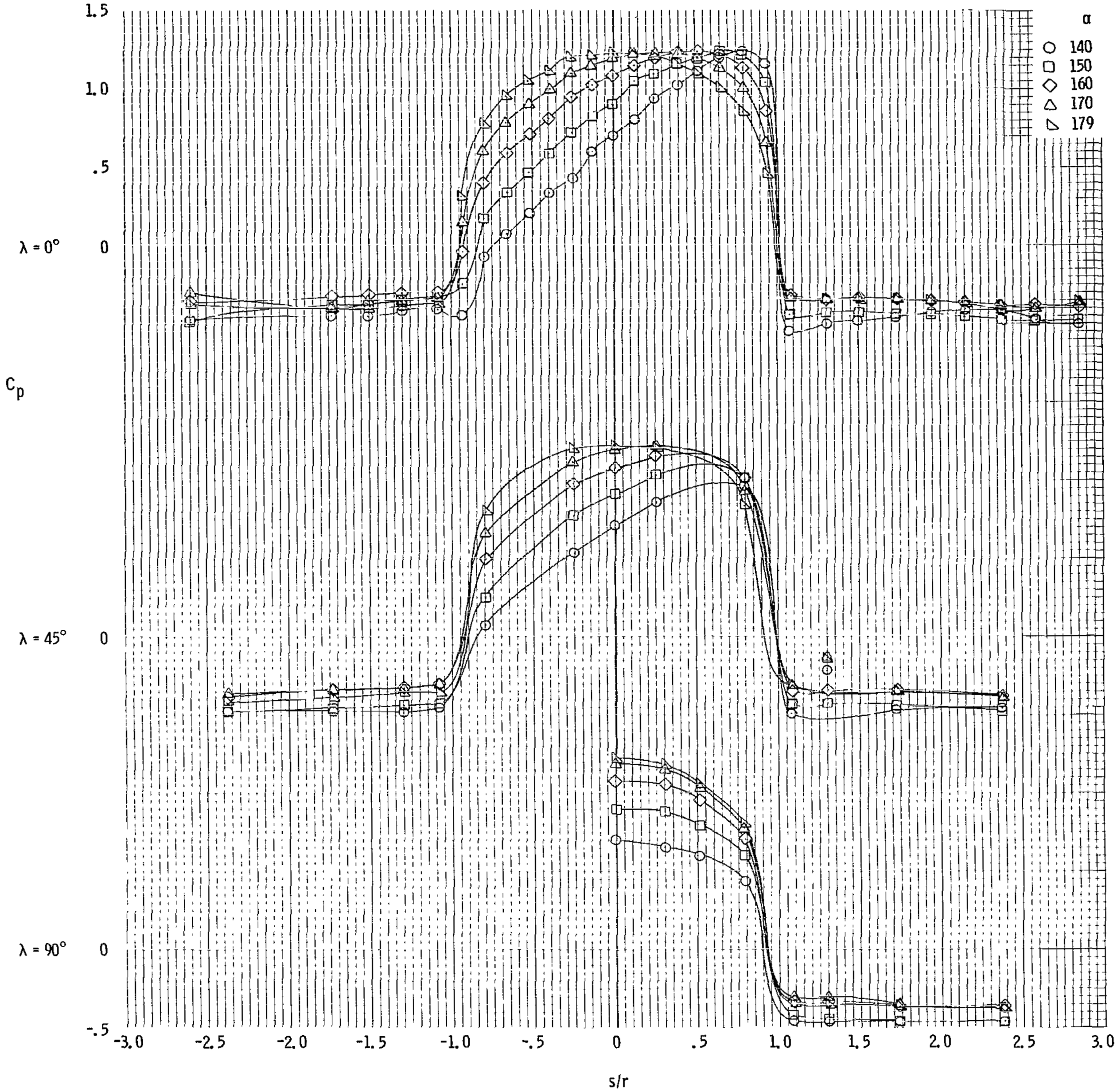

Figure 21. - Variation of C_p with increasing α at $\lambda = 0°$, $\lambda = 45°$, and $\lambda = 90°$ at M = 0.9, 0.02-scale model, configuration C_1, heat shield forward, in the Ames 2×2 TWT test facility.

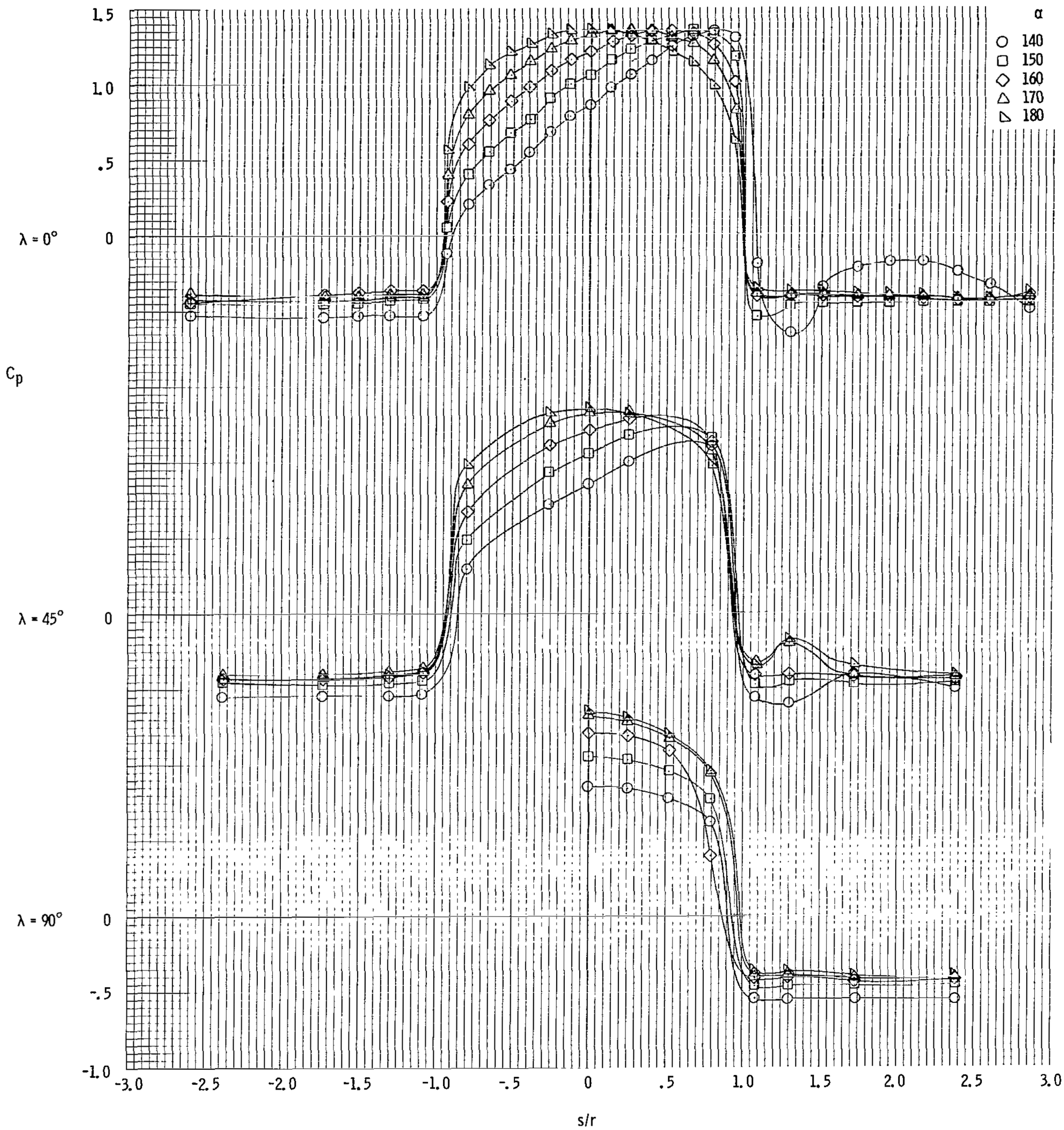

Figure 22. - Variation of C_p with increasing α at $\lambda = 0°$, $\lambda = 45°$, and $\lambda = 90°$ at $M = 1.1$, 0.02-scale model, configuration C_1, heat shield forward, in the Ames 2×2 TWT test facility.

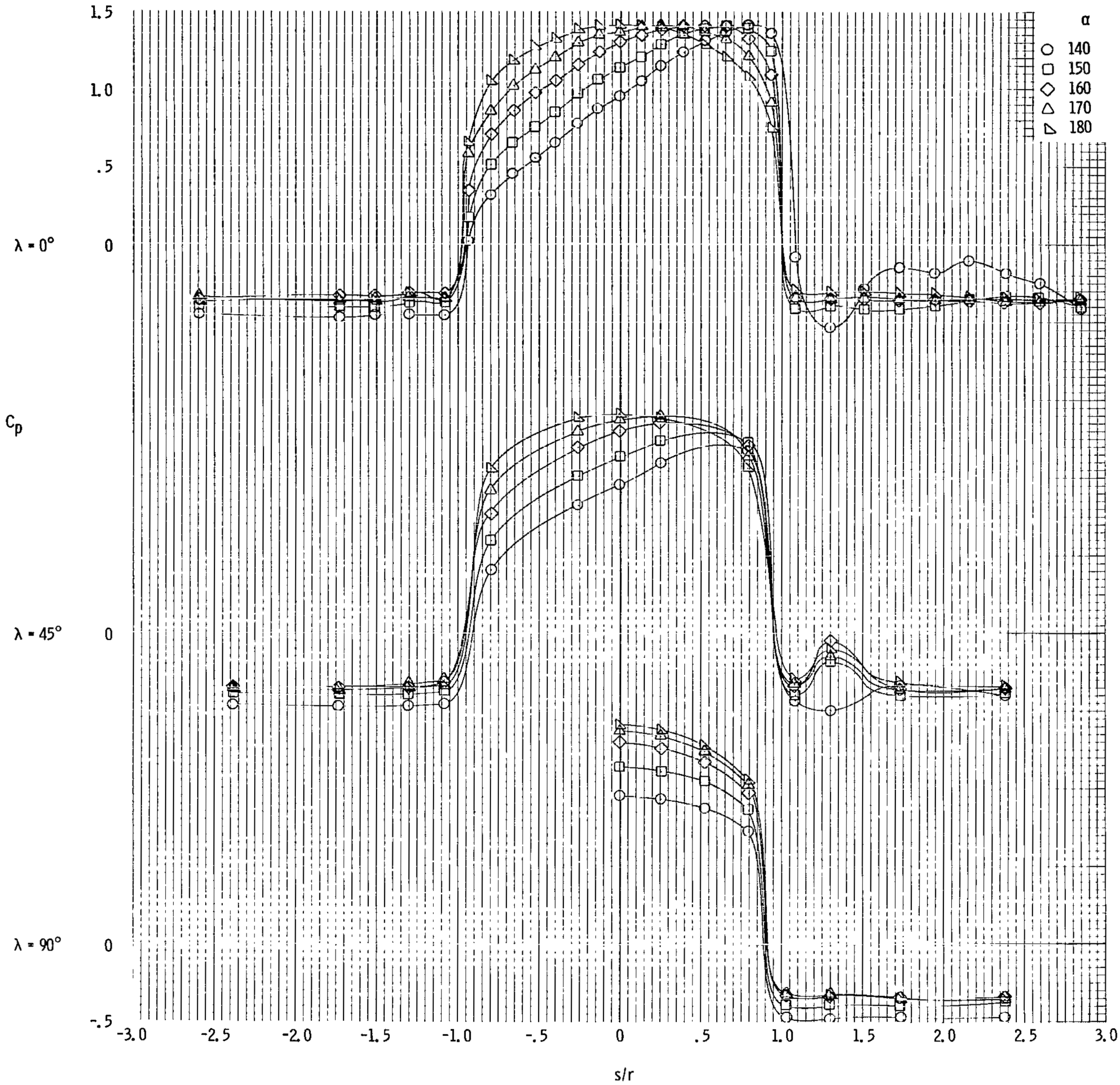

Figure 23. - Variation of C_p with increasing α at $\lambda = 0°$, $\lambda = 45°$, and $\lambda = 90°$ at $M = 1.2$, 0.02-scale model, configuration C_1, heat shield forward, in the Ames 2 × 2 TWT test facility.

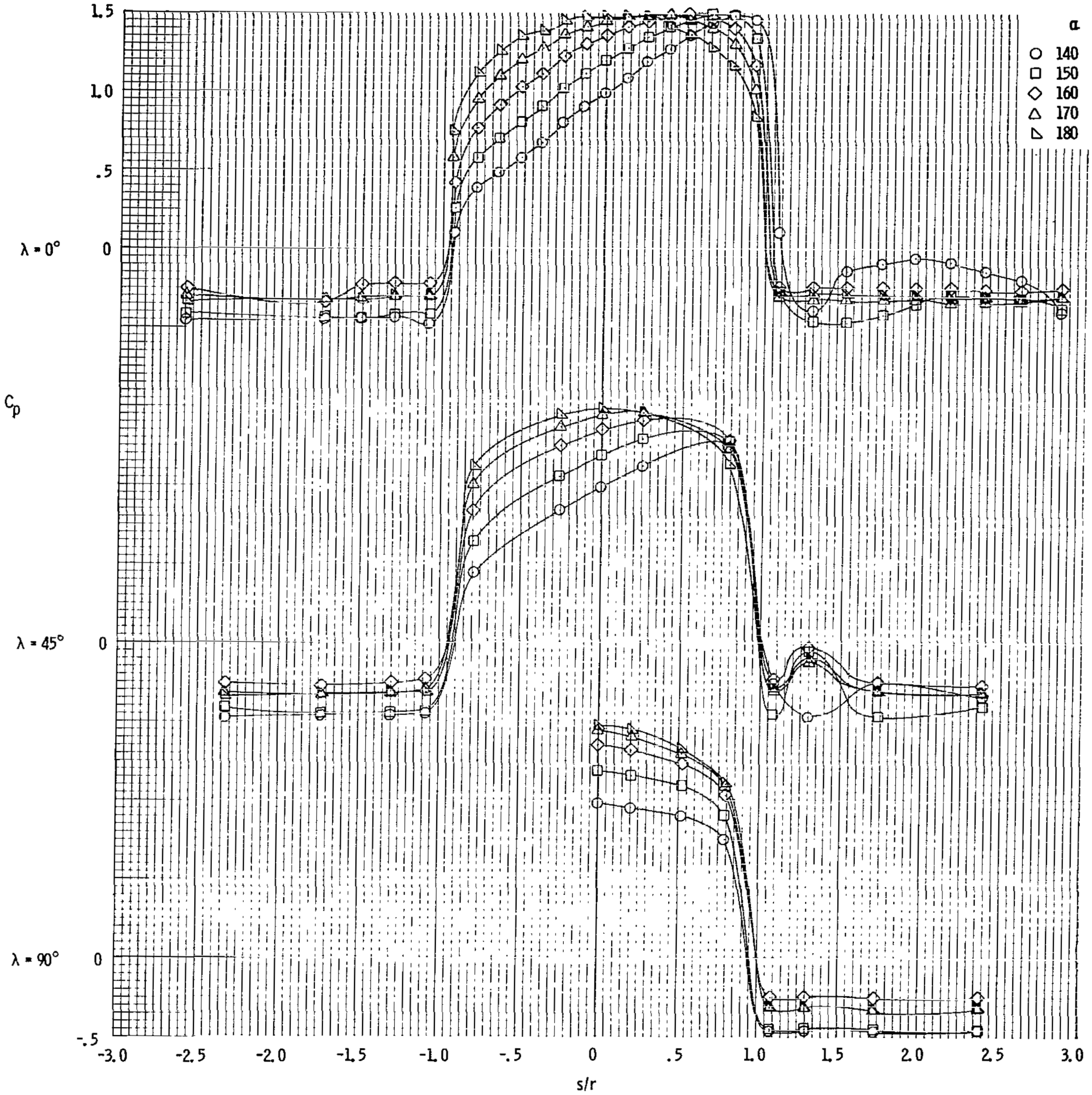

Figure 24. - Variation of C_p with increasing α at $\lambda = 0°$, $\lambda = 45°$, and $\lambda = 90°$ at M = 1.34, 0.02-scale model, configuration C_1, heat shield forward, in the Ames 2 × 2 TWT test facility.

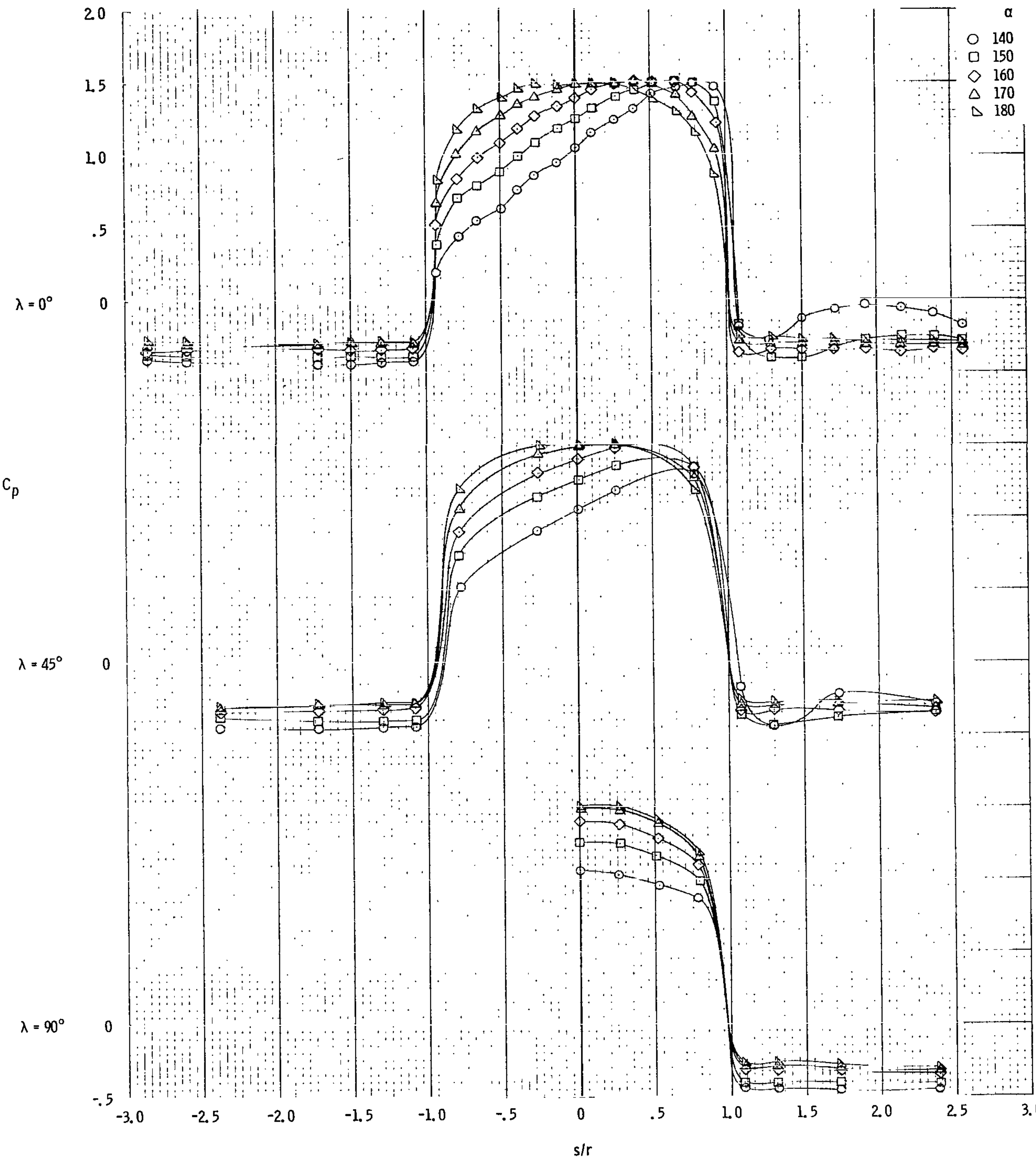

Figure 25. - Variation of C_p with increasing α at $\lambda = 0°$, $\lambda = 45°$, and $\lambda = 90°$ at M = 1.48, 0.02-scale model, configuration C_1, heat shield forward, in the JPL-20SWT test facility.

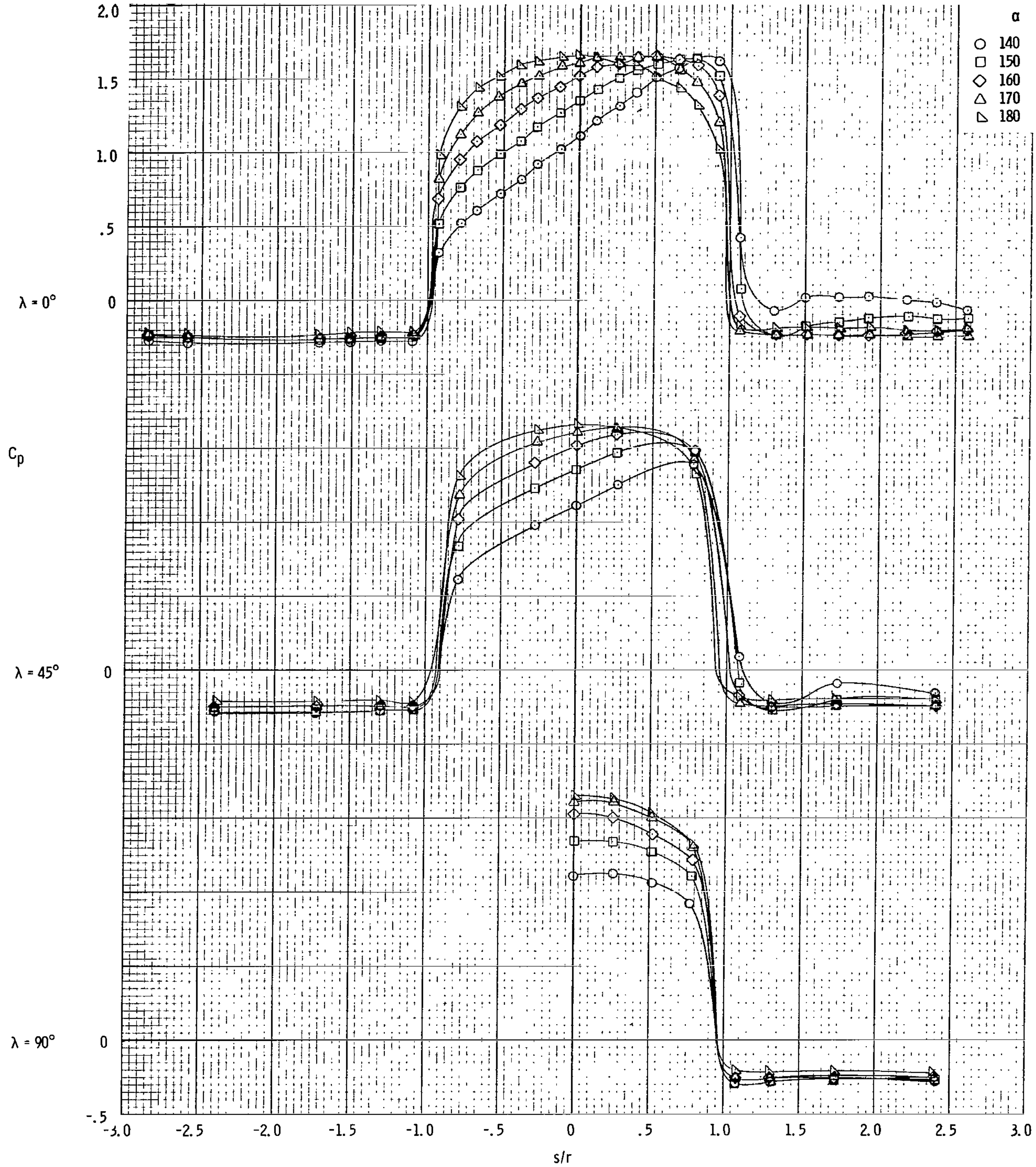

Figure 26. - Variation of C_p with increasing α at $\lambda = 0°$, $\lambda = 45°$, and $\lambda = 90°$ at M = 2.01, 0.02-scale model, configuration C_1, heat shield forward, in the JPL-20SWT test facility.

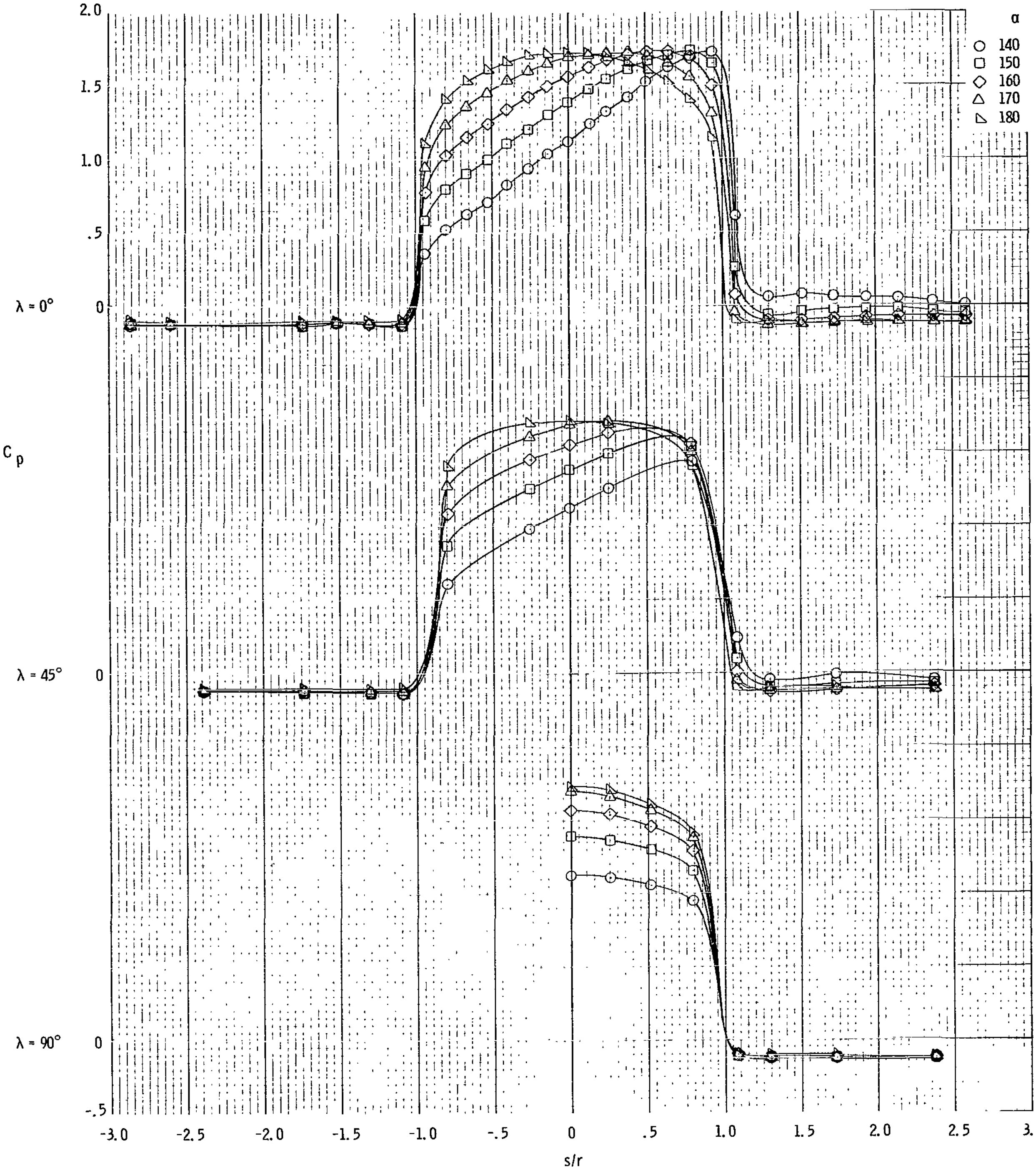

Figure 27. - Variation of C_p with increasing α at $\lambda = 0°$, $\lambda = 45°$, and $\lambda = 90°$ at $M = 3.01$, 0.02-scale model, configuration C_1, heat shield forward, in the JPL-20SWT test facility.

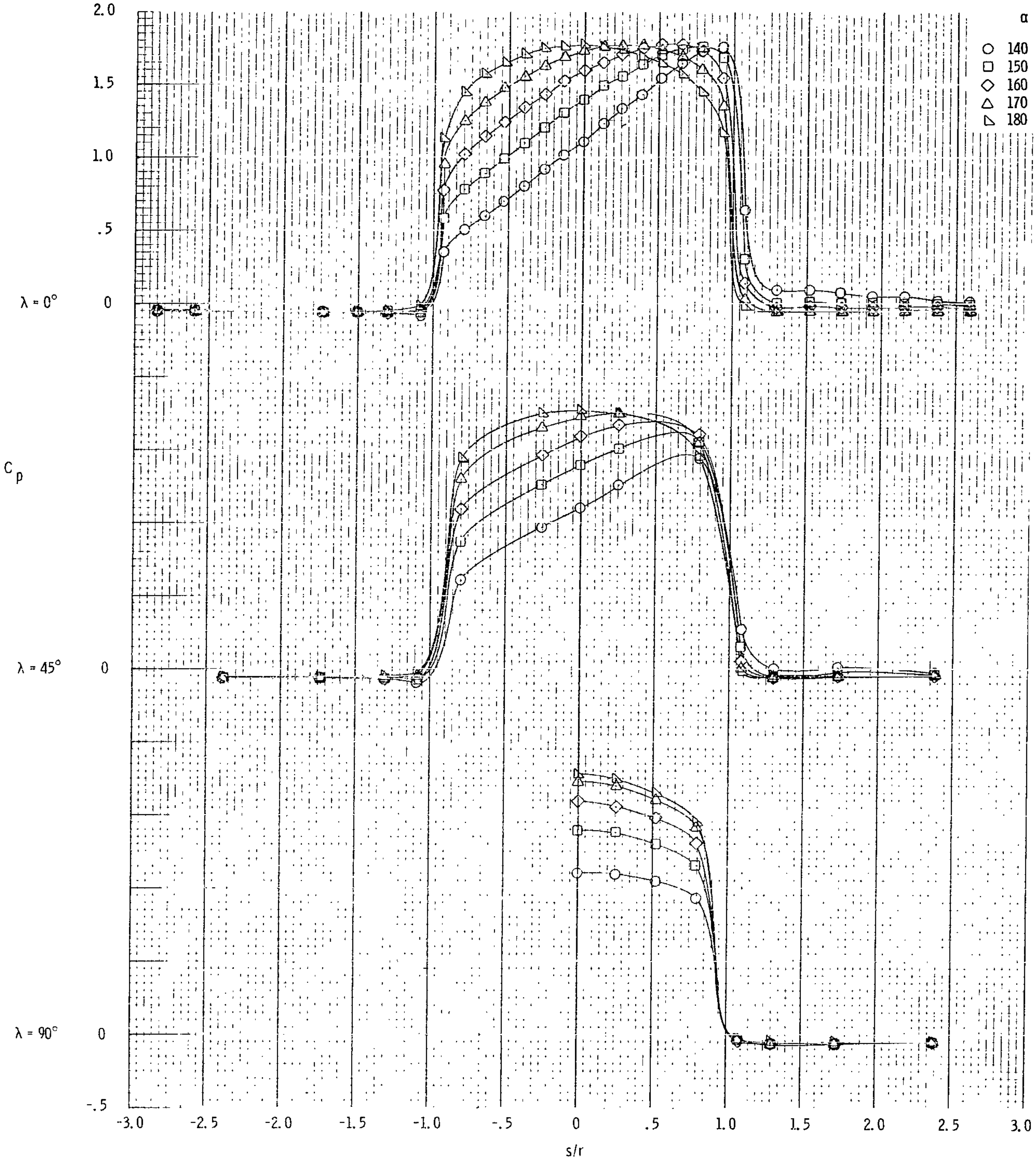

Figure 28. - Variation of C_p with increasing α at $\lambda = 0°$, $\lambda = 45°$, and $\lambda = 90°$ at $M = 3.99$, 0.02-scale model, configuration C_1, heat shield forward, in the JPL-20SWT test facility.

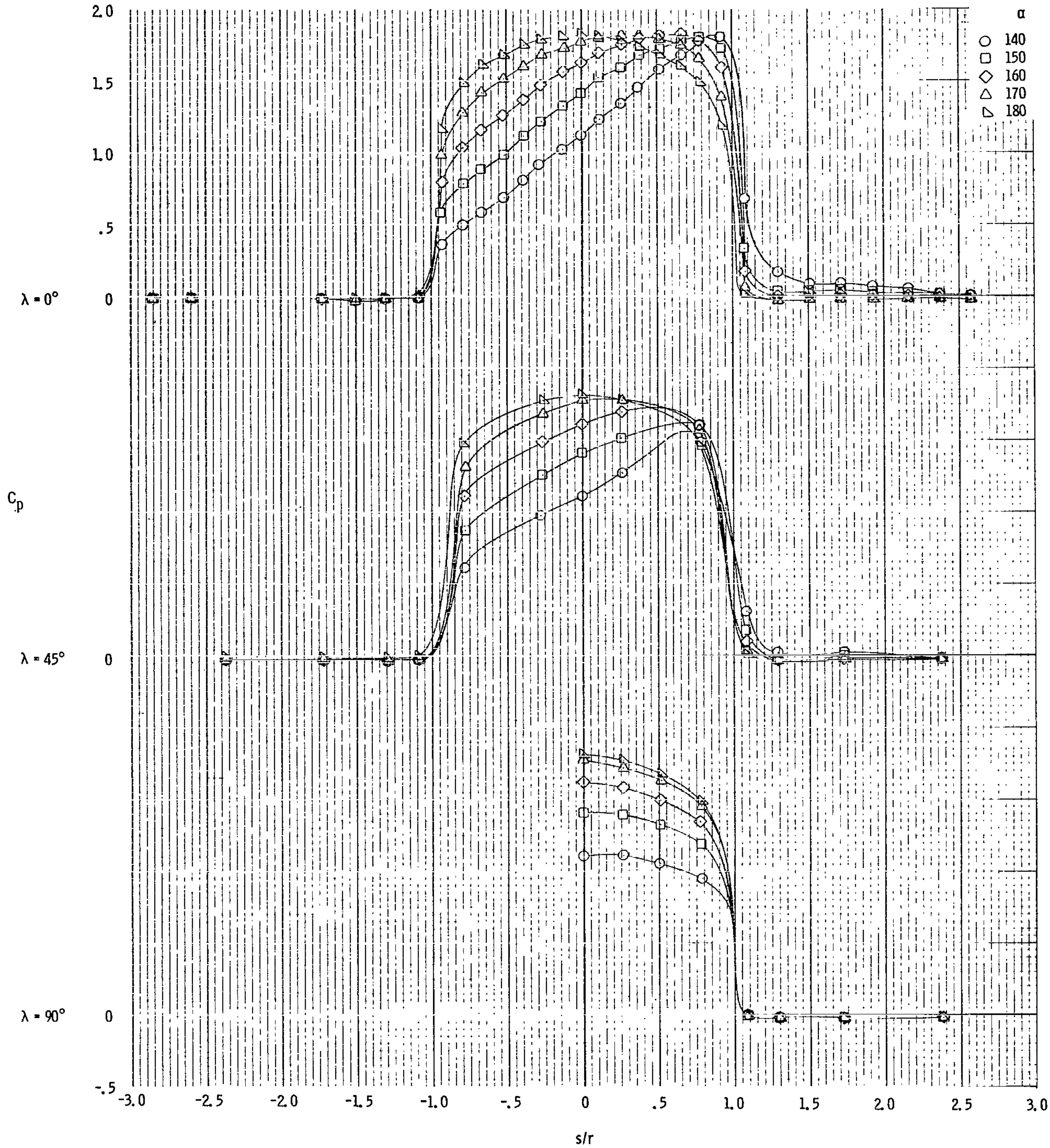

Figure 29. - Variation of C_p with increasing α at $\lambda = 0°$, $\lambda = 45°$, and $\lambda = 90°$ at M = 5.01, 0.02-scale model, configuration C_1, heat shield forward, in the JPL-20SWT test facility.

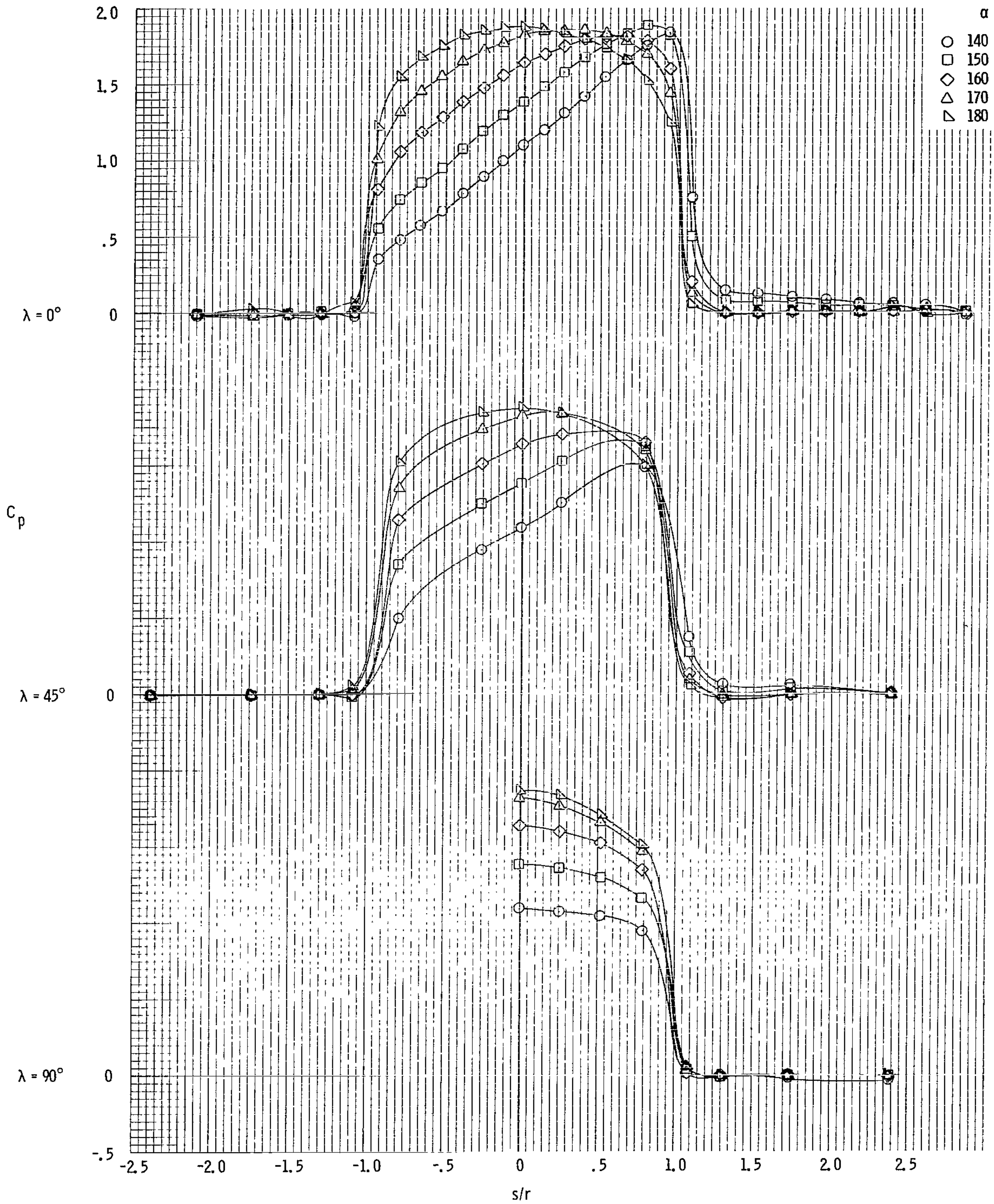

Figure 30. - Variation of C_p with increasing α at $\lambda = 0°$, $\lambda = 45°$, and $\lambda = 90°$ at M = 6.07, 0.02-scale model, configuration C_1, heat shield forward, in the JPL-21HWT test facility.

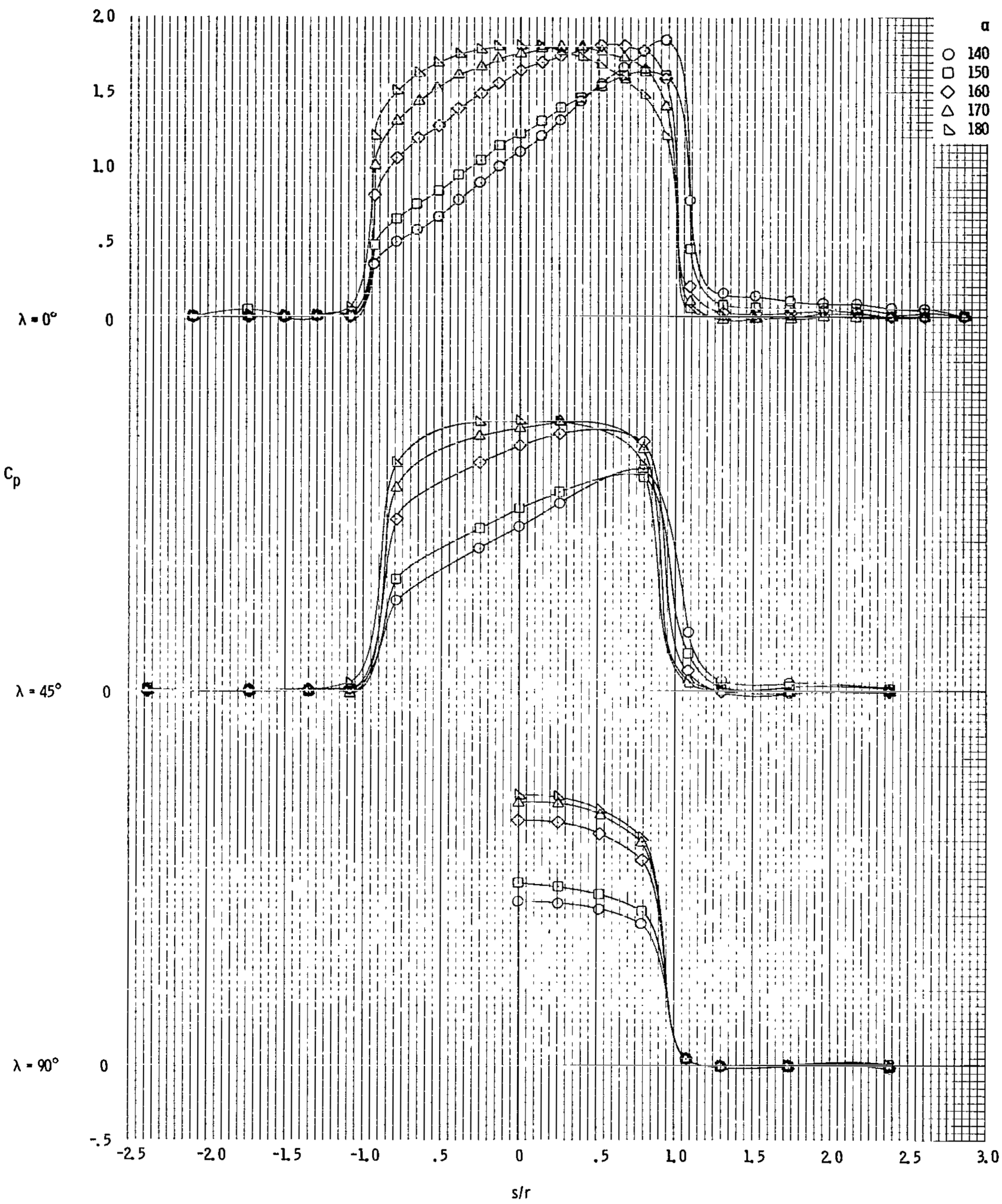

Figure 31. - Variation of C_p with increasing α at $\lambda = 0°$, $\lambda = 45°$, and $\lambda = 90°$ at $M = 7.35$, 0.02-scale model, configuration C_1, heat shield forward, in the JPL-21HWT test facility.

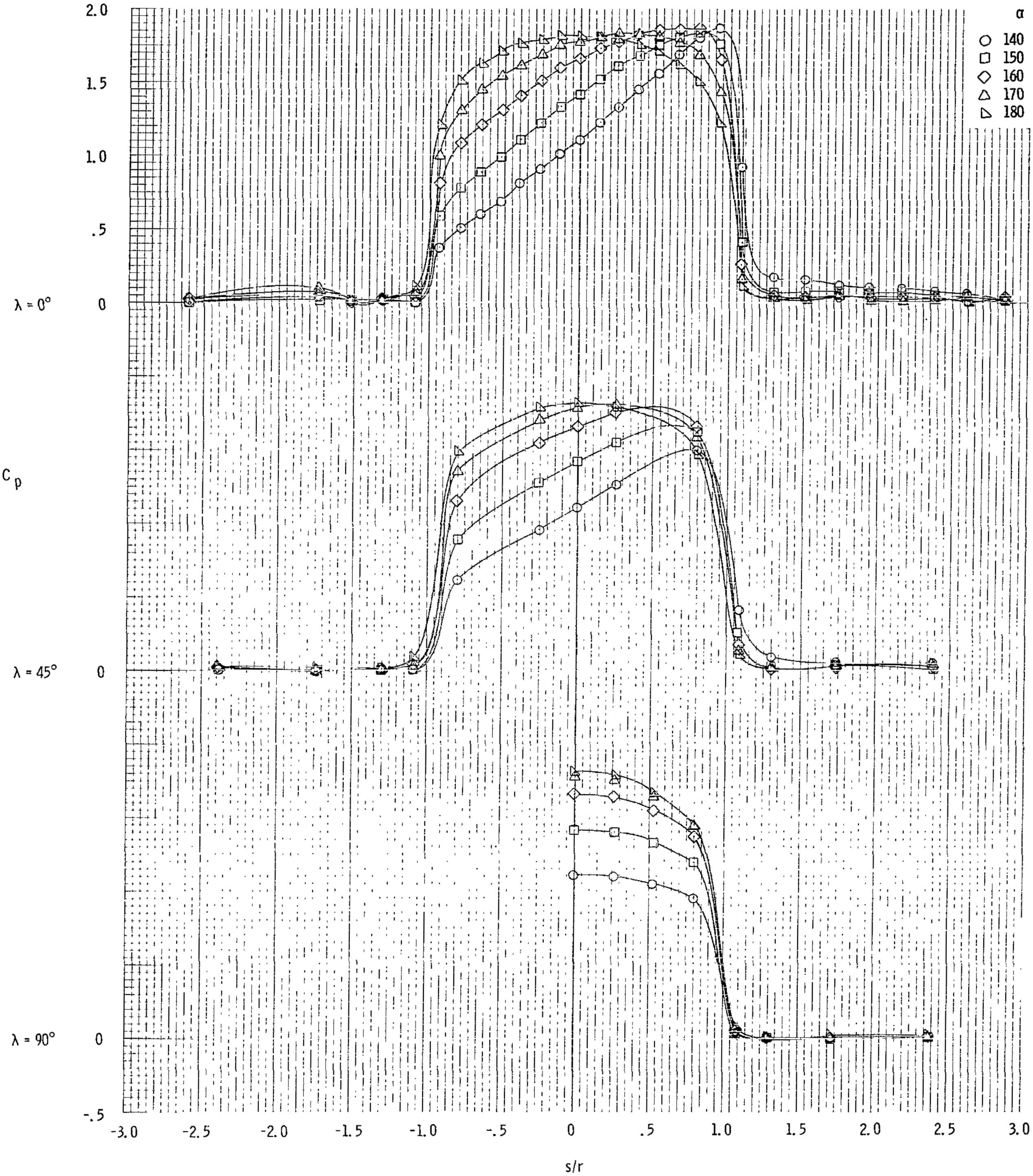

Figure 32. - Variation of C_p with increasing α at $\lambda = 0°$, $\lambda = 45°$, and $\lambda = 90°$ at M = 9.08, 0.02-scale model, configuration C_1, heat shield forward, in the JPL-21HWT test facility.

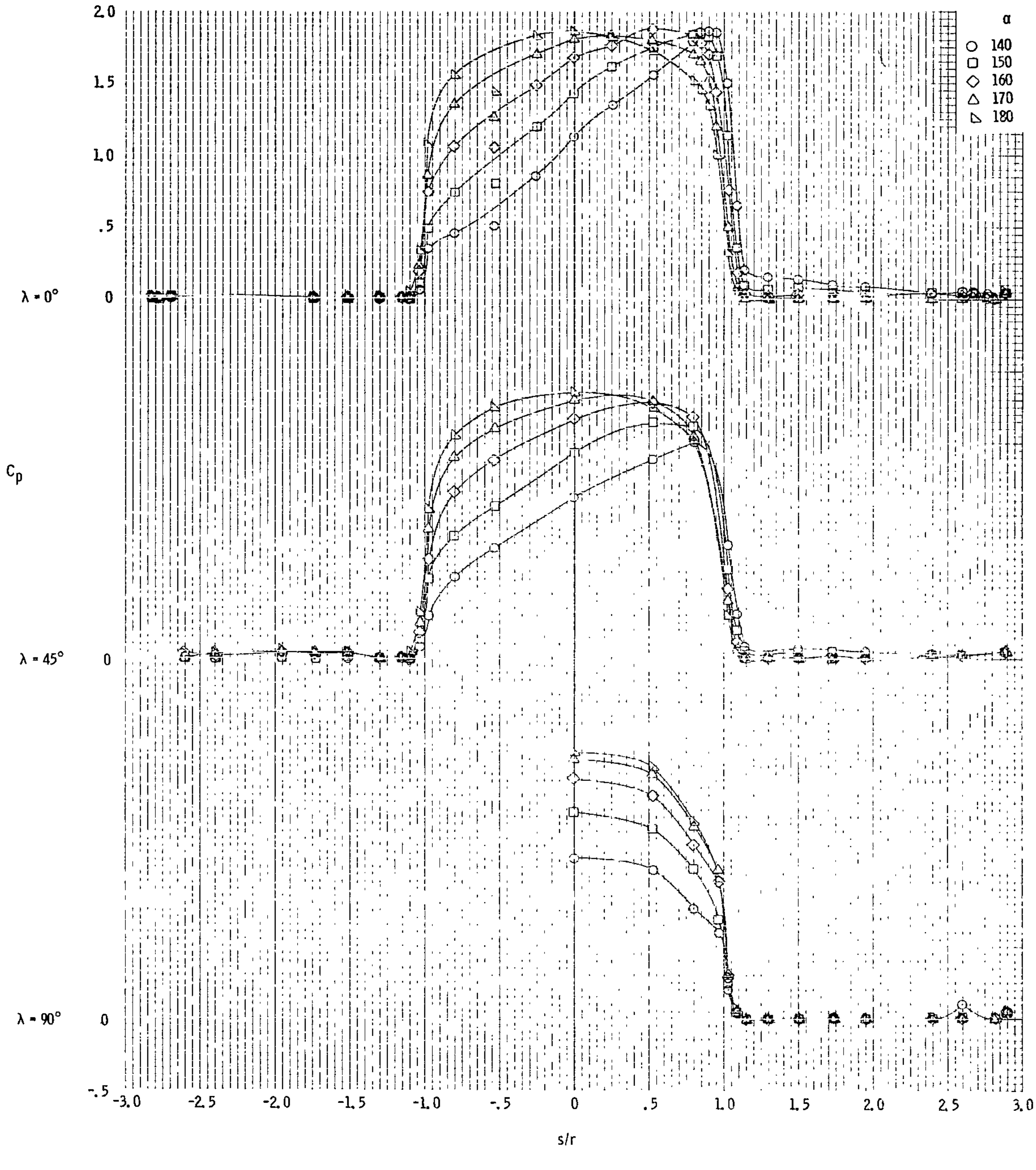

Figure 33. - Variation of C_p with increasing α at $\lambda = 0°$, $\lambda = 45°$, and $\lambda = 90°$ at $M = 10.1$, 0.045-scale model, configuration C_2, heat shield forward, in the AEDC-C test facility.

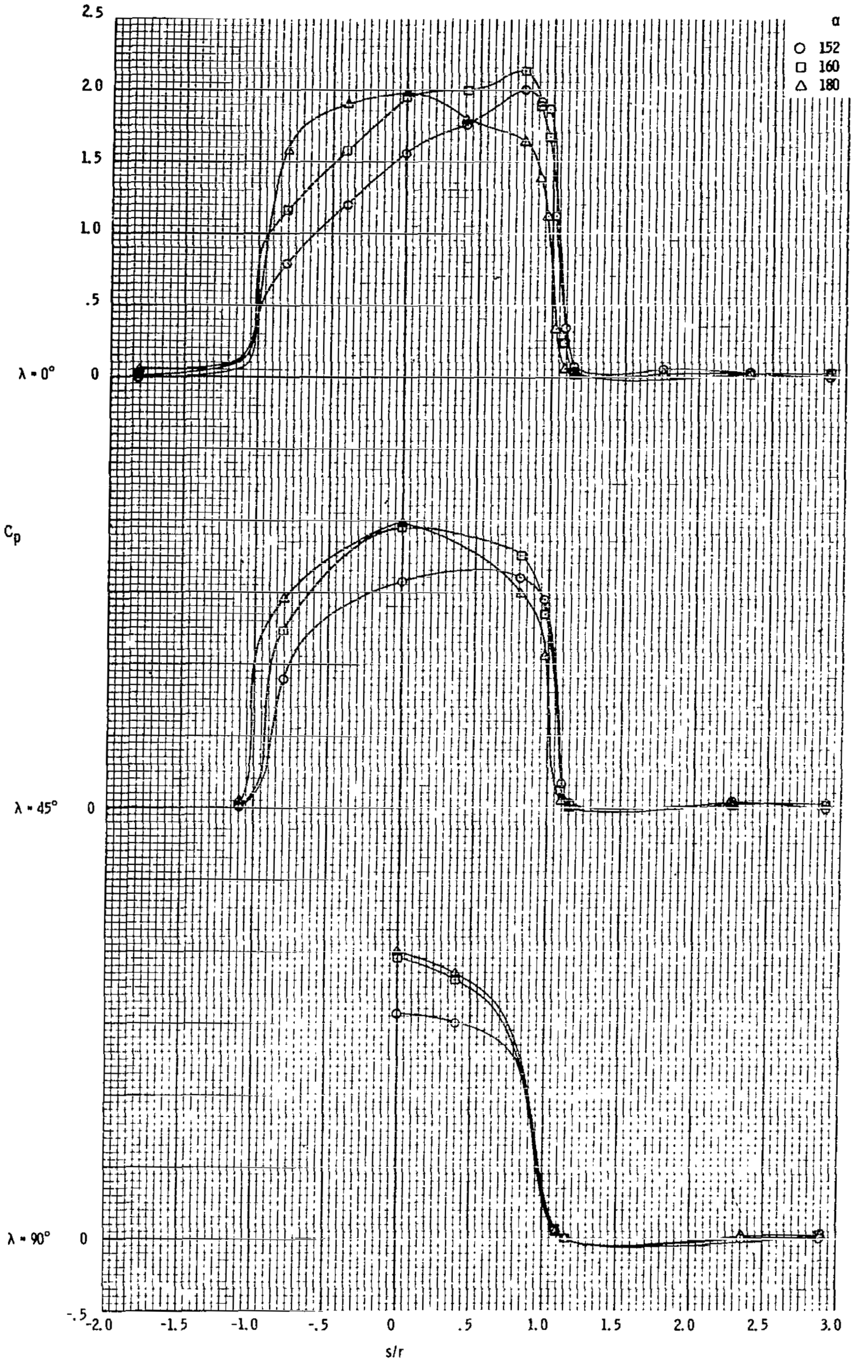

Figure 34. - Variation of C_p with increasing α at $\lambda = 0°$, $\lambda = 45°$, and $\lambda = 90°$ at $M = 12.0$, 0.05-scale model, configuration C_2, heat shield forward, in the CAL-48HST test facility.

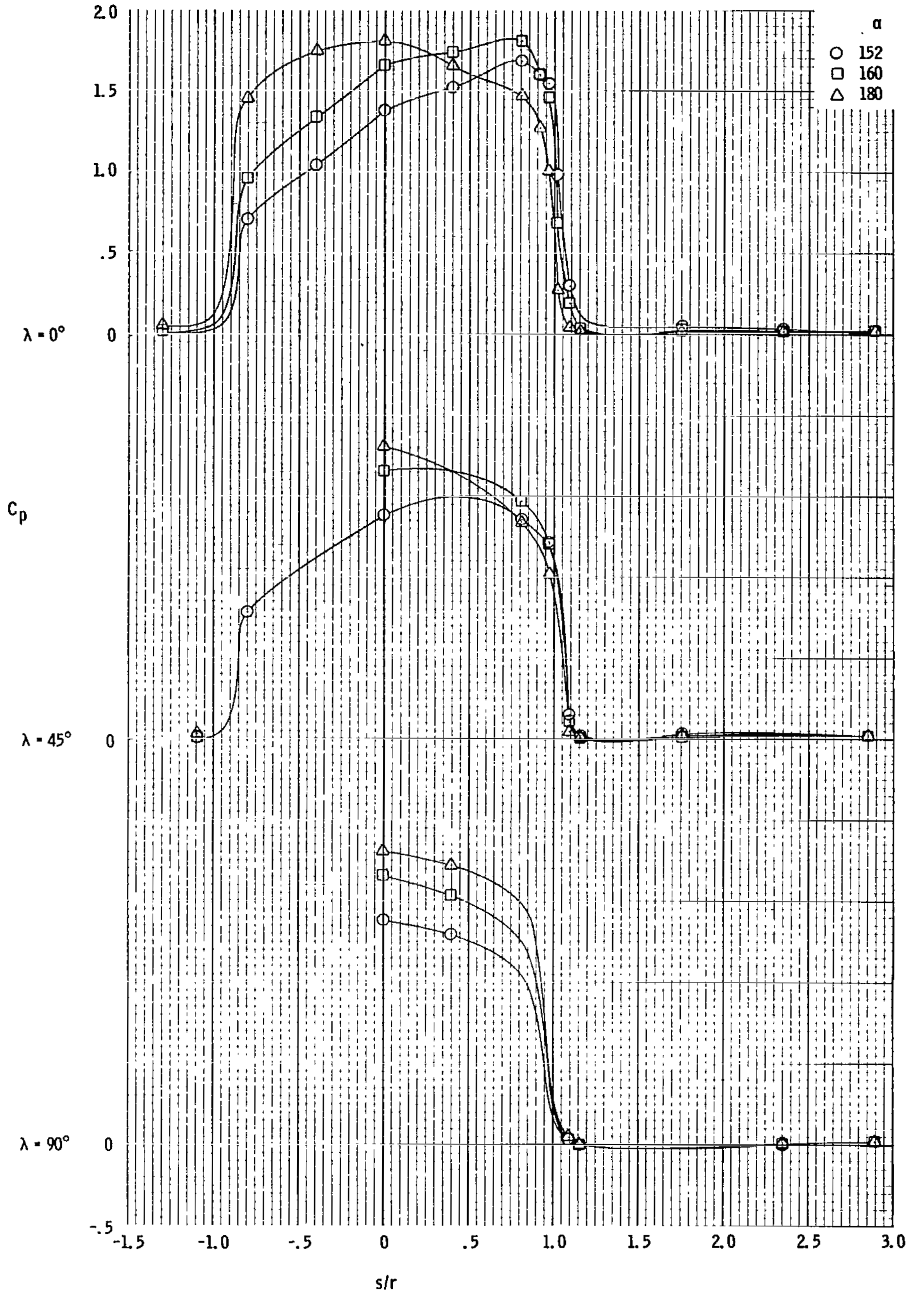

Figure 35. - Variation of C_p with increasing α at $\lambda = 0°$, $\lambda = 45°$, and $\lambda = 90°$ at M = 12.7, 0.05-scale model, configuration C_2, heat shield forward, in the CAL-48HST test facility.

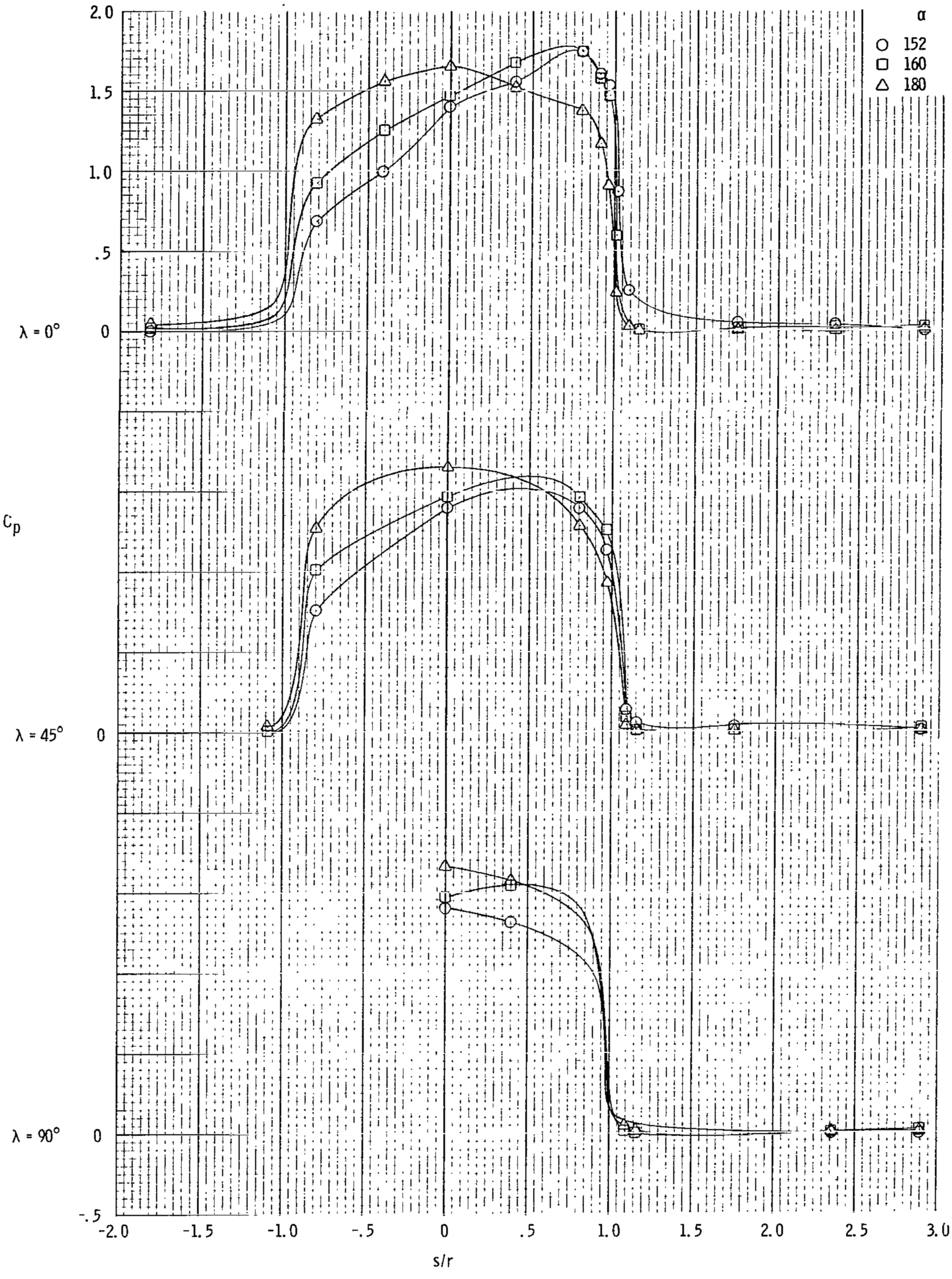

Figure 36. - Variation of C_p with increasing α at $\lambda = 0°$, $\lambda = 45°$, and $\lambda = 90°$ at M = 13.1, 0.05-scale model, configuration C_2, heat shield forward, in the CAL-48HST test facility.

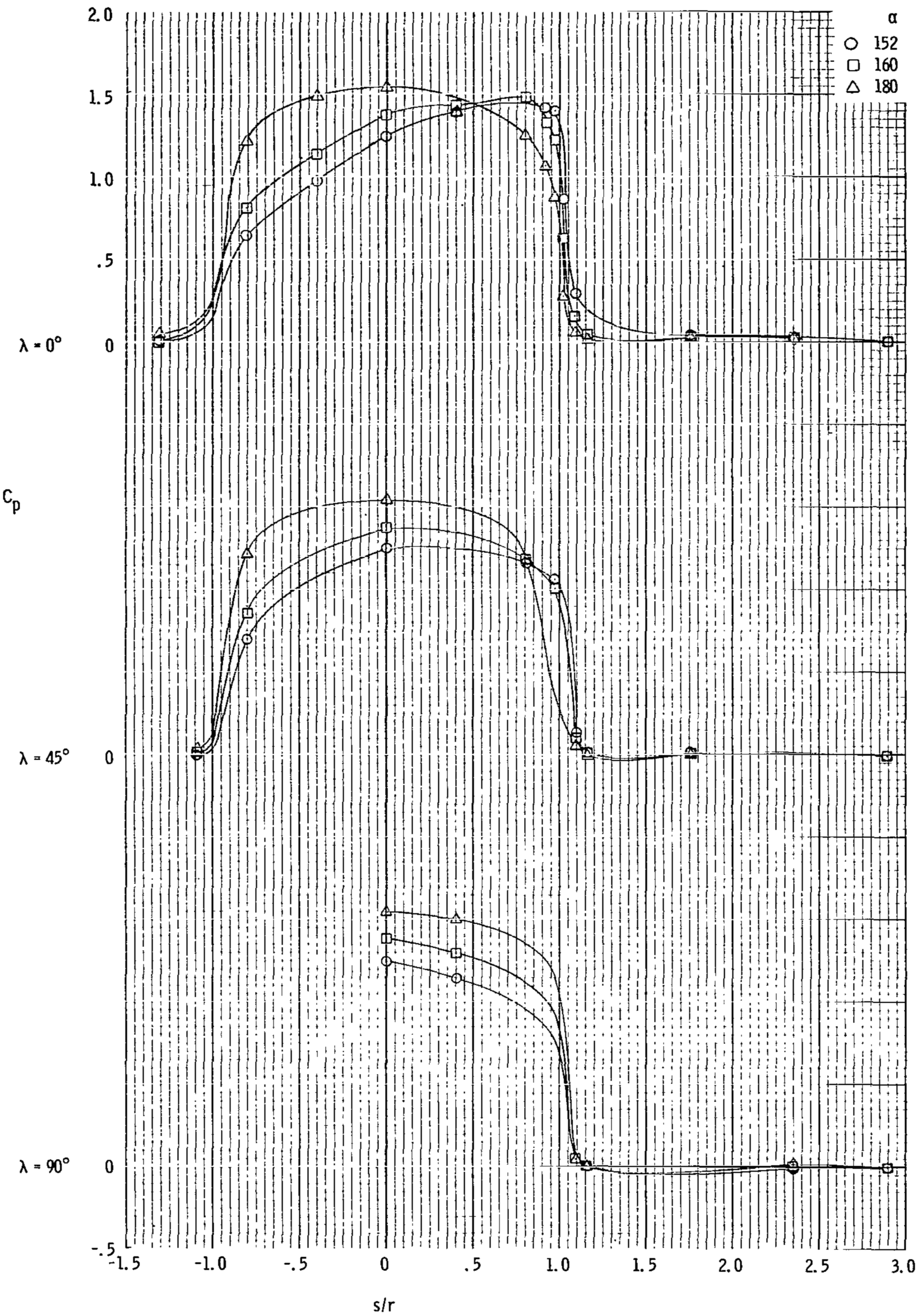

Figure 37. - Variation of C_p with increasing α at $\lambda = 0°$, $\lambda = 45°$, and $\lambda = 90°$ at M = 16.2, 0.05-scale model, configuration C_2, heat shield forward, in the CAL-48HST test facility.

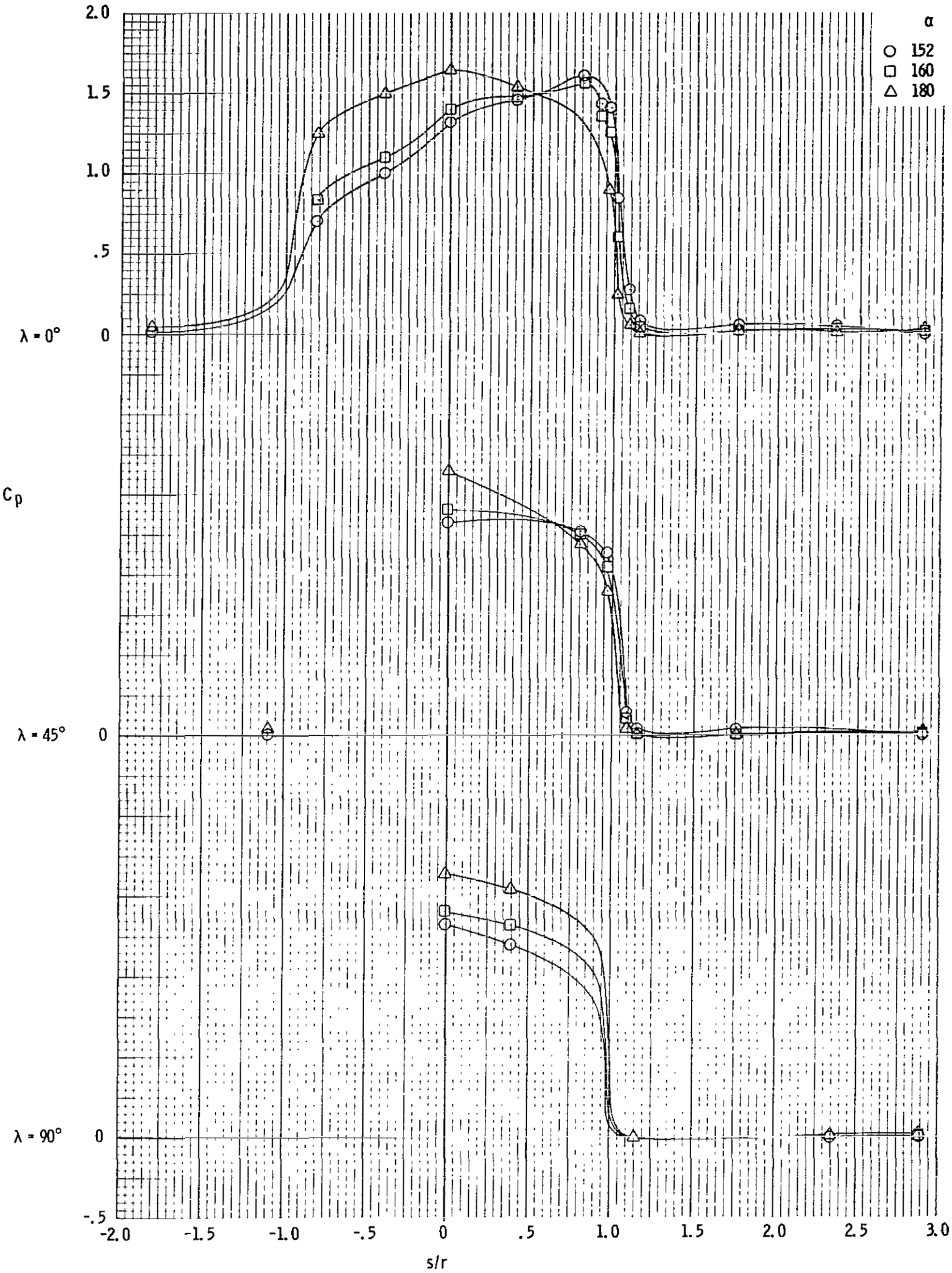

Figure 38. - Variation of C_p with increasing α at $\lambda = 0°$, $\lambda = 45°$, and $\lambda = 90°$ at $M = 17.3$, 0.05-scale model, configuration C_2, heat shield forward, in the CAL-48HST test facility.

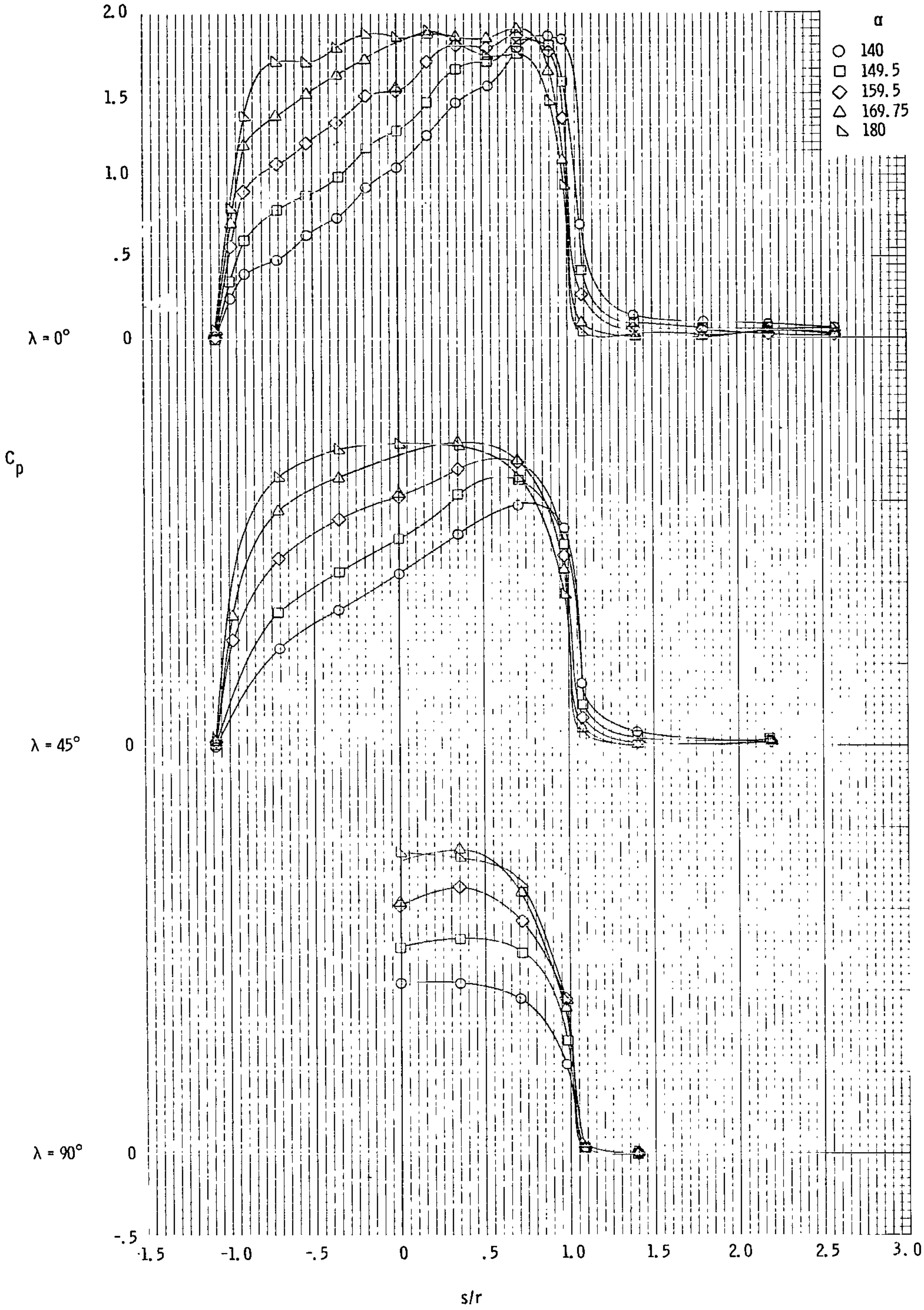

Figure 39. - Variation of C_p with increasing α at $\lambda = 0°$, $\lambda = 45°$, and $\lambda = 90°$ at M = 19.0, 0.04-scale model, configuration C_2, heat shield forward, in the AEDC-HS II test facility.

NATIONAL AERONAUTICS AND SPACE ADMINISTRATION
WASHINGTON, D. C. 20546

OFFICIAL BUSINESS

FIRST CLASS MAIL

POSTAGE AND FEES PAID
NATIONAL AERONAUTICS AND
SPACE ADMINISTRATION

020 001 25 51 30S 69286 00903
AIR FORCE WEAPONS LABORATORY/WLIL/
KIRTLAND AIR FORCE BASE, NEW MEXICO 8711
ATT E. LOU BOWMAN, CHIEF, TECH. LIBRARY

POSTMASTER: If Undeliverable (Section 158 Postal Manual) Do Not Return

"The aeronautical and space activities of the United States shall be conducted so as to contribute . . . to the expansion of human knowledge of phenomena in the atmosphere and space. The Administration shall provide for the widest practicable and appropriate dissemination of information concerning its activities and the results thereof."

—NATIONAL AERONAUTICS AND SPACE ACT OF 1958

NASA SCIENTIFIC AND TECHNICAL PUBLICATIONS

TECHNICAL REPORTS: Scientific and technical information considered important, complete, and a lasting contribution to existing knowledge.

TECHNICAL NOTES: Information less broad in scope but nevertheless of importance as a contribution to existing knowledge.

TECHNICAL MEMORANDUMS: Information receiving limited distribution because of preliminary data, security classification, or other reasons.

CONTRACTOR REPORTS: Scientific and technical information generated under a NASA contract or grant and considered an important contribution to existing knowledge.

TECHNICAL TRANSLATIONS: Information published in a foreign language considered to merit NASA distribution in English.

SPECIAL PUBLICATIONS: Information derived from or of value to NASA activities. Publications include conference proceedings, monographs, data compilations, handbooks, sourcebooks, and special bibliographies.

TECHNOLOGY UTILIZATION PUBLICATIONS: Information on technology used by NASA that may be of particular interest in commercial and other non-aerospace applications. Publications include Tech Briefs, Technology Utilization Reports and Notes, and Technology Surveys.

Details on the availability of these publications may be obtained from:

SCIENTIFIC AND TECHNICAL INFORMATION DIVISION

NATIONAL AERONAUTICS AND SPACE ADMINISTRATION

Washington, D.C. 20546